Optimal Sizing of

Battery/Ultracapacitor-Based Energy Storage Systems

in Electric Vehicles

by

Amir Ostadi

A Thesis

presented to the University of Waterloo

in fulfillment of

the requirement for the degree of

Doctor of Philosophy

in

Electrical and Computer Engineering

Watreloo, Ontario, Canada

Author's Declaration

I hereby declare that I am the sole author of this thesis. This is a true copy of the thesis, including any required final revisions, as accepted by my examiners.

I understand that my thesis may be made electronically available to the public.

Abstract

In recent years, electrification of powertrain has gradually become the core of research and development efforts in automotive industry. This is mainly due to the fact that electrified powertrains can effectively alleviate concerns of environmental pollution caused by internal combustion engines (ICEs) and reduce the rate of depletion of the earth's natural resources, while offering a higher efficiency and a better fuel economy.

One of the key components of every electric vehicle (EV)/hybrid electric vehicle (HEV) is the Energy Storage System (ESS). An ESS provides propulsion power to the electric drivetrain and captures regenerative braking power. Batteries and ultracapacitors are the most well-known ESS devices for automotive applications.

In battery/ultracapacitor-based powertrains, the storage units are configured as series-parallel arrangements of individual cells. In this thesis, the battery and ultracapacitor units are assumed to be composed of parallel branches of series-connected cells. Optimal sizing of the storage unit (determining the optimum numbers of the parallel branches and series-connected cells) and the interfacing infrastructure (if any DC-DC converter exists between the storage unit(s) and the traction motor controller) can have a significant impact on the manufacturing cost of the electric vehicle and its fuel economy.

This thesis formulates the problem of optimal sizing of battery/ultracapacitor-based energy storage systems in electric vehicles. Through the course of this research, a flexible optimization platform has been developed. When solving the optimization problem, different constraints such as limits on state of charge, current, and power of the battery cells, current and power of the ultracapacitor cells, voltage conversion of the DC-DC converter, DC bus voltage, and operation characteristics of the inverter and the traction motor are taken into account. This optimization tool is used to solve the problem of optimal sizing

of the storage systems for two different classes of vehicles: (i) a small-size, long-range car and (ii) a city bus. Aside from optimal sizing of the storage systems as the main objective, the developed platform provides a proper simulation tool for analyzing the performance of existing electric vehicles on the road.

Acknowledgements

Table of Contents

List of Tables

List of Figures

List of Abbreviations

ACO: Ant Colony Optimization

BU: Battery Unit

CD: Charge Depletion

CS: Charge Sustenance

EM: Electric Motor

ESS: Energy Storage System

EV: Electric Vehicle

FTP: Federal Test Procedure

GA: Genetic Algorithm

HESS: Hybrid Energy Storage System

HEV: Hybrid Electric Vehicle

HWFET: Highway Fuel Economy Driving Schedule

ICE: Internal Combustion Engine

INLP: Integer Nonlinear Programming

MINLP: Mixed-Integer Nonlinear Programming

NEDC: New European Driving Cycle

PHEV: Plug-in Hybrid Electric Vehicle

PSO: Particle Swarm Optimization

pu: per-unit

SA: Simulated Annealing

SoC: State of Charge

SPWM: Sinusoidal Pulse Width Modulation

SQP: Sequential Quadratic Programming

SVM: Space Vector Modulation

TLBO: Teaching-Learning-Based Optimization

UC: Ultracapacitor Unit

UDDS: Urban Dynamometer Driving Schedule

List of Symbols

Indices

i: Index of equality constraint number

j: Index of inequality constraint number or population member number

k: Index of iteration number

m: Index of population member number

n: Index of sampled interval number

s: Index of vector X element

w: Index of population member number

Parameters

A_f: Equivalent frontal area of the vehicle (m^2)

C_b: Price of the battery cell in US dollars ($)

C_{con}: Price per kW of the DC-DC converter in US dollars ($)

C_d: Drag coefficient

C_u: Price of the ultracapacitor cell in US dollars ($)

C_0: Fixed capacitance of the ultracapacitor cell (F)

g: Gravitational acceleration (m/s^2)

$I_{b,max}$: Maximum value of the battery cell current (A)

$I_{b,min}$: Minimum value of the battery cell current (A)

N_g: Gear ratio of the gearbox

Pr: Tire pressure (psi)

Q_b: Rated capacity of the battery cell (Ah)

R_D: Series resistance of the IGBT anti-parallel diode (Ω)

R_{sw}: Series resistance of the IGBT switch (Ω)

r_{wh}: Wheels' radius (m)

SoC_{max}: Maximum value of the state of charge of battery cell

SoC_{min}: Minimum value of the state of charge of battery cell

t_{off}: Turn-off cross-over time of the IGBT switch (s)

t_{on}: Turn-on cross-over time of the IGBT switch (s)

T_s: Sampling time (s)

V_D: Fixed voltage drop of the IGBT anti-parallel diode (V)

$V_{DC,max}$: Maximum value of the DC bus voltage (V)

$V_{DC,min}$: Minimum value of the DC bus voltage (V)

V_{sw}: Fixed voltage drop of the IGBT switch (V)

v_w: Wind speed (m/s)

η_g: Efficiency of the gearbox

ρ_a: Air density (kg/m^3)

σ: Grade of the road

Variables

a_1: Fourier cosine coefficient of the fundamental component of the phase 'a' voltage (V)

b_1: Fourier sine coefficient of the fundamental component of the phase 'a' voltage (V)

C_{blt}: Long-transient capacitance of the battery cell (F)

C_{bst}: Short-transient capacitance of the battery cell (F)

C_1: Voltage-dependent capacitance of the ultracapacitor cell (F)

d: Duty ratio of the top switch in phase 'a' leg of the DC-AC converter

d_{max}: Maximum value of the switch duty ratio

d_{min}: Minimum value of the switch duty ratio

d_{sdn}: Duty ratio of the buck switch

d_{sup}: Duty ratio of the boost switch

f_{obj}: Objective function

f_s: Frequency of the stator voltage

f_{sdn}: Voltage conversion ratio for step-down mode of operation of the DC-DC converter

f_{sup}: Voltage conversion ratio for step-up mode of operation of the DC-DC converter

f_{sw}: Switching frequency of the IGBT switch

H_e: Equality constraint

H_{ine}: Inequality constraint

I: Amplitude of the phase 'a' current (A)

i_a: Phase 'a' current of the DC-AC converter (A)

i_b: Discharging current of the battery cell (A)

i_m: Magnetizing current of the induction machine (A)

I_r: rms value of the rotor current (A)

i_r: Rotor current of the induction machine (A)

I_s: rms value of the stator current (A)

i_s: Stator current of the induction machine (A)

i_u: Discharging current of the ultracapacitor cell (A)

$I_{u,max}$: Maximum value of the ultracapacitor cell current (A)

$I_{u,min}$: Minimum value of the ultracapacitor cell current (A)

i_x: Cell discharging current of the storage devices directly connected to the DC bus (A)

$L_{\ell r}$: Rotor leakage inductance referred to the stator frame (H)

$L_{\ell s}$: Stator leakage inductance (H)

L_m: Magnetizing inductance (H)

L_{th}: Thevenin equivalent inductance (H)

M: Modulating index

m: Modulating signal normalized to the peak value of the triangular waveform

M_{pop}: Mean value of all members of the population

M_t: Total mass of the vehicle (kg)

N_{bp}: Number of battery parallel branches

N_{bs}: Number of series-connected battery cells

N_e: Number of equality constraints

N_{ine}: Number of inequality constraints

N_p: Number of machine poles

n_r: rpm velocity of the rotor shaft (rpm)

N_{up}: Number of ultracapacitor parallel branches

N_{us}: Number of series-connected ultracapacitor cells

N_{xp}: Number of parallel branches of the storage devices directly connected to the DC bus

N_{xs}: Number of series-connected cells of the storage devices directly connected to the DC bus

P_a: AC-side average power of the first leg of the DC-AC converter (W)

P_{ag}: 3-phase airgap power (W)

$P_{b,max}$: Maximum value of the battery cell power (W)

$P_{b,min}$: Minimum value of the battery cell power (W)

P_{BU}: Power of the battery unit (W)

P_{con}: Power rating of the DC-DC converter (W)

P_d: Power demand (W)

P_{DC}: Power demand on the DC bus (W)

P_{loss}: Total losses of the three-phase DC-AC converter (W)

P_{mech}: 3-phase rotor mechanical power (W)

p_{sw}: Switching loss of the IGBT switch (W)

P_{sw-a}: Average switching loss for one leg of the DC-AC converter (W)

$P_{u,max}$: Maximum value of the ultracapacitor cell power (W)

$P_{u,min}$: Minimum value of the ultracapacitor cell power (W)

P_{UC}: Power of the ultracapacitor unit (W)

R_{bes}: Effective series resistance of the battery cell (Ω)

R_{blt}: Long-transient resistance of the battery cell (Ω)

R_{bst}: Short-transient resistance of the battery cell (Ω)

R_c: Core resistance (Ω)

$r_{k,1}$: Random number between 0 and 1

$r_{k,2}$: Random number between 0 and 1

$r_{k,3}$: Random number between 0 and 1

R_r: Rotor resistance referred to the stator frame (Ω)

R_s: Stator resistance (Ω)

R_{th}: Thevenin equivalent resistance (Ω)

R_{ues}: Effective series resistance of the ultracapacitor cell (Ω)

s: Rotor slip

s_{max}: Rotor slip corresponding to maximum mechanical torque

S: State of charge of the battery cell

T_{max}: Maximum mechanical torque $(N.m)$

T_{mech}: 3-phase rotor mechanical torque $(N.m)$

T_{wh}: Torque of the wheels $(N.m)$

v: Velocity of the vehicle (m/s)

v_a: Phase 'a' voltage of the DC-AC converter with respect to the middle point N of the DC-side capacitors (V)

V_{a1}: rms value of the fundamental component of the phase 'a' voltage (V)

v_{blt}: Long-transient voltage of the battery cell (V)

v_{bst}: Short-transient voltage of the battery cell (V)

v_{bt}: Terminal voltage of the battery cell (V)

V_{BU}: Terminal voltage of the battery unit (V)

V_{DC}: DC bus voltage (V)

v_{oc}: Open-circuit voltage of the battery cell (V)

V_s: rms value of the stator terminal voltage (V)

v_s: Stator terminal voltage of the induction machine (V)

V_{th}: rms value of the Thevenin voltage (V)

v_{th}: Thevenin voltage (V)

v_{ut}: Terminal voltage of the ultracapacitor cell (V)

$V_{ut,max}$: Maximum value of the terminal voltage of ultracapacitor cell (V)

$V_{ut,min}$: Minimum value of the terminal voltage of ultracapacitor cell (V)

v_{u1}: Open-circuit voltage of the ultracapacitor cell (V)

v_{xt}: Cell terminal voltage of the storage devices directly connected to the DC bus (V)

X: Vector of optimization variables

X_{inf}: An infeasible solution for the optimization problem

X_{new}: Temporarily-updated position of the member of population

$X_{teacher}$: Position of the best member of population

x: Element of the vector X

x_{max}: Maximum value of the element of the vector X

x_{min}: Minimum value of the element of the vector X

Z_{in}: Input impedance (Ω)

α: Coefficient which assumes values of 1 or 0 for motoring or regenerative braking mode of operation, respectively

β: Coefficient which assumes values of 1 or 0 for step-up or step-down operation mode of the DC-DC converter, respectively

γ: Coefficient which assumes values of 1 or 0 for motoring or regenerative braking mode of operation, respectively

ζ: Set of inputs

$\eta_{e,m}$: Efficiency of the electric motor during motoring mode of operation

$\eta_{e,r}$: Efficiency of the electric motor during regenerative braking mode of operation

$\eta_{g,m}$: Efficiency of the gearbox during motoring mode of operation

$\eta_{g,r}$: Efficiency of the gearbox during regenerative braking mode of operation

$\eta_{i,m}$: Efficiency of the DC-AC converter during motoring mode of operation

$\eta_{i,r}$: Efficiency of the DC-AC converter during regenerative braking mode of operation

η_m: Efficiency of the drivetrain during motoring mode of operation

η_r: Efficiency of the drivetrain during regenerative braking mode of operation

η_{sdn}: Efficiency of the DC-DC converter in step-down mode of operation

η_{sup}: Efficiency of the DC-DC converter in step-up mode of operation

θ: Angle of the modulating index

μ: Friction coefficient

ξ: Angle-equivalent element of the vector X

ϕ: Angle difference between the AC current and the modulating signal

ω_r: Angular velocity of the rotor shaft (rad/s)

ω_{sy}: Synchronous speed (rad/s)

$\omega_{sy,base}$: Base angular velocity (rad/s)

Chapter 1

Introduction

Concerns about environmental pollution, rapid increase in fuel cost, and depletion of fossil fuel reserves have been the main motivations behind the movement towards transportation electrification. Along with research sectors in the automotive industry, researchers in academia have been playing an important role in advancing the knowledge and technology supporting development of electric vehicles (EVs) and hybrid electric vehicles (HEVs) [1]. Although EVs and HEVs offer numerous benefits, there are some hurdles in the path of electrification of transportation that have to be overcome. One of the main issues is the limitations of the current technology of energy storage devices [2]. Statistical analysis shows that customers are reluctant to purchase electric and hybrid electric vehicles unless the performance and reliability of these types of vehicle match or exceed those of traditional internal combustion engine (ICE)-based vehicles, at a competitive price [3].

1.1 Motivations

A key component of every EV/HEV is the Energy Storage System (ESS). ESS consists of a source or a combination of two or more sources, which provides electric power for the drivetrain in an EV/HEV. Among electrical energy storage devices used in an ESS, batteries and ultracapacitors are the most well-known ones [4, 5].

In a battery, electric power is generated via an electrochemical reaction. Each battery cell is mainly composed of two electrodes (Anode and Cathode), an electrolyte, and a conducting separator. In the process of generating power, anions are oxidized at the anode and cations receive the free electrons if the circuit is closed. Batteries are known as sources with high specific energy (or gravimetric energy density in Wh/kg). However, the specific power (or gravimetric power density in W/kg) of batteries is normally low compared to that of ultracapacitors [4, 6].

Ultracapacitors are devices with relatively higher specific power than that of conventional batteries [4]. This makes ultracapacitors a favorable choice for relieving the battery-based energy storage systems in conditions of harsh power fluctuations.

Due to limitations imposed by economy, time, and available resources, optimization is a crucially important task in developing any new technology. This applies specially to technologies developed by automotive industry. In EVs and HEVs, optimization of the energy storage systems is important due to its impact on lowering manufacturing cost and weight/volume of the system, enhancing fuel economy, and reducing harmful gas emissions (in case of HEVs).

In an electric powertrain, the energy storage devices (batteries and ultracapacitor in this study) are configured in series-parallel combinations of individual cells. These series-parallel arrangements along with the interfacing infrastructure and control and protection

2

circuits define the storage systems. The cost of storage system is a large portion of the manufacturing price of the electric vehicle. Therefore, conducting a quantitative analysis which determines the optimum numbers of the parallel branches and series-connected cells and rating of the interfacing infrastructure installed in the powertrains of EVs will be beneficial to both car manufacturers and their costumers.

1.2 Literature Review

Optimal sizing of the powertrain components in electric and hybrid electric vehicles has been addressed in a vast body of literature. Different criteria can be used for classification of problems of optimal sizing for energy storage systems. One classification approach is based on the number of different types of energy sources responsible for meeting power requirements of the vehicle. From this viewpoint, the simplest form of optimization is when there is only one type of energy source (either battery or ultracapacitor in this study) in the powertrain. Battery-based ESS in Tesla Roadster and ultracapacitor-based ESS in Sinautecs electric bus are two examples [7, 8]. In this type of powertrain, control system is much simpler than that in the case where two or more different types of energy sources exist in the structure of powertrain. Examples are Honda Accord and Toyota Prius hybrid electric vehicles [9]. In the case of having more than one type of energy source installed, the control circuit requires sophisticated energy management techniques to split the power among different sources [10]. Considering the fact that the existing sources have different characteristics (from specific energy and specific power points of view), the problem of optimal sizing can become more complex. The optimization problem can be solved using different algorithms such as Linear Programming (if the system is convex and can be represented by a set of linear functions), Dynamic Programming (both deterministic

and stochastic), and Evolutionary methods such as Genetic Algorithm (GA), Simulated Annealing (SA), and Particle Swarm Optimization (PSO) [11]-[15]. It should be noted when more than one type of energy storage devices is installed in the powertrain, the ESS can be called a hybrid ESS or HESS (battery-ultracapacitor electric powertrain in this study).

Another approach for classifying the optimization problems is on the basis of types of constraints considered for solving the problem. In this regard, the easiest way of solving the problem is based on maximum power requirement from the storage system and rated terminal voltage on the DC bus (the voltage requirement and maximum power demand determine the numbers of series-connected cells and parallel branches of the devices in the storage system) [16]. The power requirement of the vehicle is normally calculated on a specific drive cycle. The drive cycle may be a standard one, available in public domain, or it can be generated by combining the standard drive cycles [17]. Calculating the size of storage units based on maximum value of the power demand, though simple to implement, does not consider behavior of the storage devices at different levels of state of charge (SoC). In other words, performance of the storage devices mainly maximum power capability, open-circuit voltage, and charge/discharge efficiency vary according to state of charge. Therefore, the powertrain may not meet the power requirement of the vehicle at specific moments of time in the course of a drive cycle. In [16], sizes of the battery and ultracapacitor units in a HESS installed in an HEV were determined using the set points of the upper and lower voltage limits defined for the ultracapacitors and the peak power demand. The ultracapacitor and battery units are connected to the DC bus via bidirectional switches. Battery unit is mainly responsible for meeting the energy requirement on the electric drivetrain during cruising. When the vehicle is under acceleration or deceleration, the ultracapacitor unit swap the battery unit on the DC bus. The paper did not present the models used for the

storage devices. In addition, it did not provide any model for efficiencies of the drivetrain components, i.e., the inverter and the traction motor.

For a more accurate analysis, a constraint on the energy requirement of the vehicle can be added to the problem. To do this, the energy demand (the area under the curve of power versus time) for completing a specific drive cycle is divided by a constant efficiency (accounting for the efficiency of the powertrain) to determine capacity in kWh required from the storage system. Using this constraint, along with maximum value of the power demand and the DC bus voltage, the numbers of parallel branches and series-connected cells are determined [18]. Like in the previous case, the solution obtained in this regard does not take performance of the storage devices at different levels of SoC into account. Reference [18] discussed design of a HESS composed of battery and ultracapacitor units for a fuel cell vehicle, based on splitting the total energy demand among fuel cell stacks, batteries, and ultracapacitors to successfully complete a priori known drive cycle. The fuel cell was supposed to provide the average power of the load during specific intervals while the battery and ultracapacitor units provided the remaining part. The paper formulated the sizing problem in a multi-objective format using the total mass of the vehicle and manufacturing cost of the storage units and fuel cell stacks.

To improve the accuracy of optimization, speed-versus-time profile of the vehicle under study (drive cycle) can be discretized using a specific sampling time. Then, the job of optimization platform is to determine the size of the storage system in such a way that the power requirement of the vehicle is met at every sampled interval of the drive cycle [3, 12, 19, 20].

As mentioned before, a very important issue in optimal sizing of the powertrains with more than one type of energy source is about the energy management technique used to split the power among the available sources. A common approach in this regard is to

use rule-based techniques [21]. In rule-based methods, modes of operation are determined based on some of the variables of the system such as power demand, state of charge of the storage devices and/or velocity of the vehicle. As an example, let's consider thermostat control as one of the rule-based approaches. In an HEV which has ICE and battery cells as the power sources, thermostat control keeps the engine off as long as the battery SoC is above the predefined lower limit. This type of control is normally utilized in series HEV [13, 14, 22, 23].

In [3], designing a HESS for installing in Chrysler Pacifia which had a parallel drivetrain was discussed. The HESS included battery and ultracapacitor cells. A rule-based procedure was used to determine the specifications of different components of the powertrain. Power management between batteries and ultracapacitors was based on the power demand and percentage of the maximum power deliverable by the cells. The behavior of the cells in terms of variation of open-circuit voltage versus SoC and the limits on the currents and voltages were not considered. In addition, no specific configuration of HESS in terms of interfacing batteries and ultracapacitors using DC-DC converters was clearly discussed when designing the powertrain components.

Reference [19] used a simple rule-based technique to determine the sizes of ICE and traction motor for a power-split plug-in HEV (PHEV) using the efficiency maps. It was assumed that the ICE would provide the average power demand and the rest of power would be supplied by the ESS. ADVISOR package was used for the purpose of optimization with three different drive cycles (UDDS, HWFET, and NEDC) being used for calculating the average power required from the ICE.

Another rule-based approach is based on fuzzy logic. In fuzzy-based techniques, two or more operating modes are used to control power management between different sources of the powertrain in a fuzzy logic fashion. Therefore, transition between one mode and

6

another does not occur at a specific moment of time which is the case in deterministic rule-based methods, but in a continuous manner. Reference [24] used an intelligent fuzzy logic controller to monitor charge of the battery cells while distributing the torque (power) in such a way that the efficiency of the internal combustion engine was maximized. The paper did not provide any mathematical model for representing the behavior of the components in the electric path of the powertrain (battery, inverter, and traction motor).

In optimization-based strategies, well-known optimization techniques are used to optimize the system for a given drive cycle. Optimization can be carried out based on a fixed control law (such as low-pass filtering of the power demand to generate the power reference for battery unit) or based on arbitrary splitting of the power demand among available sources [21, 25]. In [12], Sequential Quadratic Programming (SQP) was used for designing the size of battery pack and flywheel in a combat vehicle. Three different scenarios in terms of vehicle weight and harshness of the mission were considered for designing the components. In the first scenario, the vehicle did not carry any gun and the battery unit was sized based on a light-duty mission. In the second and third scenarios, due to having two different guns onboard, the mass and size of the storage system changed as the power and energy requirements of the vehicle's missions became totally different from those in the first scenario. Behavior of the storage devises in terms of variations of efficiency and open-circuit voltage versus SoC was not considered for sizing of the cells. In addition, efficiencies of inverter and traction motor were not modelled for the purpose of optimization.

Reference [20] presented a detailed analysis on sizing of the battery unit for an HEV using stochastic Dynamic Programming approach. The duration and power demand of the drive cycle were modeled by normal (Gaussian) distribution functions. The drive cycle was generated randomly using Markov chain to take stochastic variations of an unknown drive

7

cycle into considerations. The authors designed the battery unit based on two scenarios: (i) charge depletion (CD)-charge sustenance (CS) and (ii) blended procedure which took both cost of electricity and fuel economy into consideration. However, the authors did not consider the constraints on the terminal voltage of the battery bank. In addition, efficiencies of the converter and traction motor were not modelled.

In [26], a battery-ultracapacitor HESS was designed for an electric city bus. The power management was based on low-pass filtering of the power demand, where the low-frequency component of the power was supplied/absorbed by the battery unit and the high-frequency component was taken care of by the ultracapacitor unit. The authors used limits on the DC bus voltage to determine the number of series-connected cells of the storage unit connected across the DC bus. Two different configurations of interfacing battery and ultracapacitor units to the DC bus were compared in terms of sizes of the storage devices. The paper did not consider operational characteristics of the inverter and the traction motor during optimization.

Reference [27] used Genetic Algorithm (GA) to determine the sizes of powertrain components including the maximum powers of ICE and electric machine (EM) and the number of battery cells in an HEV. Charge sustaining strategy was used for keeping SoC within predefined limits. The optimization problem was formulated in a multi-objective format for maximizing fuel economy and minimizing emissions. A deterministic approach, in which the drive cycle (UDDS) was known ahead of time, was implemented for solving the optimization problem. The paper did not consider any constraint on the cell current and terminal voltage of the battery bank. In addition, efficiencies of the inverter and the traction motor were not modelled.

In [28], the authors determined optimal size of the battery unit in a plug-in hybrid electric vehicle. The design was based on three different types of battery cells (Li-ion,

NiMH, and Lead-acid) on a drive cycle generated by the data collected in Winnipeg, Manitoba, Canada, during weekdays and weekends for 30 vehicles in a 30-day period of the month of June. This way, the drive cycle closely approximated an actual driving pattern. Power split between the ICE and the battery pack was done based on the assumption that the power demand was met by the electric motor up to the maximum power capability of the electric motor. Beyond this point, the ICE took care of the remaining portion of the power demand. The paper did not model variation of the battery cells behavior such as power capability, efficiency, and open-circuit voltage in terms of SoC.

Reference [29] addressed the problem of optimal sizing of the HESS for an HEV using Genetic Algorithm (GA). The author used a sigmoid function as a power management tool between the ICE, the battery unit, and the ultracapacitor unit. The sigmoid function was formulated in such a way that the limits on SoC of the battery and ultracapacitor cells and power capability of the battery unit were taken into account. Depending on the number of occurrences of certain velocities and accelerations over the drive cycle, the optimization algorithm was run several times to find a suboptimal power management profile based on the chosen sigmoid function. The thesis did not consider any specific arrangement for interfacing the battery and ultracapacitor units to the DC bus and it was simply assumed that the arrangement and interfacing infrastructure did not affect the result of optimization significantly. Besides, operations of the inverter and the traction motor were not modelled.

In [30], problem of optimal sizing of the storage system in a plug-in hybrid electric vehicle was solved to find the sizes of battery and ultracapacitor units which were interfaced to the DC bus via a fully-decoupled configuration with two parallel DC-DC converters. The output of optimization also determined the degree of hybridization between the storage devices and the engine. The authors used MATLAB to solve the optimization problem and implemented the corresponding system in an RTDS platform in which a flywheel, a

generator, and a controlled load emulated the vehicle's powertrain. The efficiencies of the inverter and the traction motor were not modelled for the purpose of optimization.

Reference [31] addressed the problem of optimal sizing of the powertrain components in a series plug-in hybrid electric bus. A novel heuristic method based on Pontryagin maximum principle was used for solving the optimization problem. The storage unit, which was composed of battery cells, was sized based on operation of the bus in pure electric (EV), charge-depletion, and charge-sustenance modes. In the optimization results, in addition to the optimal sizes of the components of the powertrain, the moments at which the engine must turn on/off were determined as well. In this paper, the losses of the traction motor and the inverter were modelled using a quadratic equation. The authors did not consider the voltage constraints on the battery unit. In addition, efficiency of the electric motor was not modeled in the optimization procedure.

In [32], sizes of fuel cell stacks and ultracapacitor unit were determined for an electric powertrain. The storage units were directly connected together and interfaced to the DC bus via a DC-DC converter. This limited functionality of the ultracapacitor unit. The paper did not consider behavior of the ultracapacitor in term of variation of efficiency and power capability versus open-circuit voltage and operational characteristics of the inverter and the traction motor. Reference [33] addressed optimal sizing of battery and ultracapacitor units and fuel cell stacks in an electric bus using Genetic algorithm. Charge depletion-charge sustenance strategy was used for the purpose of optimization. The paper did not consider any power electronic converter for interfacing the storage units to the DC bus. Models of the battery and ultracapacitor cells, inverter, and traction motor were not presented in this paper.

1.3 Objectives of the Research

The objectives of this PhD research are:

- Having a detailed qualitative analysis on several topologies of battery/ultracapacitor-based energy storage systems in electric powertrains.

- Developing a simulation platform which includes electrical models of powertrain components, i.e., storage devices, DC-AC converter, and electric machine.

- Formulating the problem of optimal sizing for an electric vehicle.

- Developing an optimization tool for solving the optimal sizing problem.

- Solving the optimization problem for two different classes of vehicles: (i) a small-size, long-range car and (ii) a city bus.

- Analyzing the performance of the electric powertrain with the optimally-sized ESS.

1.4 Contributions of the Research

This thesis provides a detailed work on optimal sizing of battery/ultracapacitor-based energy storage systems in electric vehicles. The outcome of the thesis is a flexible optimization platform which can be used for the purpose of optimal sizing of powertrain of any electric vehicle if the vehicle's dimension and its driving conditions are known a priori. In formulating the optimization problem, different constraints such as limits on SoC, current, and power of the battery cells, current and power of the ultracapacitor cells, voltage conversion of the DC-DC converter, DC bus voltage, and operation characteristics of the inverter and

the traction motor are taken into consideration. For solving the optimization problem, a metaheuristic population-based algorithm named Teaching-Learning-Based Optimization (TLBO) technique is implemented in MATLAB environment. Although optimization of the sizes of the powertrain components is the main capability of the developed platform, it can also be used as a useful simulation tool for analyzing performance of the existing electric vehicles on the road.

1.5 Organization of the Thesis

The rest of this thesis is organized as follows: Chapter 2 provides schematic diagrams of the powertrains of a battery-only electric vehicle, an ultracapacitor-only electric vehicle, and a battery-ultracapacitor electric vehicle. A detailed qualitative analysis on different configurations of interfacing battery and ultracapacitor units to the DC bus is presented in this chapter as well. In addition, mathematical models of different components of the powertrains, i.e., battery and ultracapacitor cells, inverter, and traction motor are provided. In Chapter 3, implementation of the optimization platform including formulation of the problem of optimal sizing and the algorithm used to solve the problem is discussed. Chapter 4 presents the results of solving the problem of optimal sizing for two different classes of electric vehicles. Chapter 5 concludes the thesis.

Chapter 2

Powertrain of an Electric Vehicle

In this chapter, different components of a battery/ultracapacitor-based powertrain used in this thesis are discussed. These components include battery and ultracapacitor cells, DC-AC converter, electric motor, and transmission system. The models discussed in this chapter for these components are implemented in the optimization platform. The chapter also discusses different configurations for interfacing battery and ultracapacitor units to the DC bus in a hybrid energy storage system.

General schematic diagrams of the powertrains of a battery-only electric vehicle, an ultracapacitor-only electric vehicle, and a battery-ultracapacitor electric vehicle are shown in Figs. 2.1, 2.2, and 2.3, respectively. The battery unit (BU) and the ultracapacitor unit (UC) are composed of parallel branches of series-connected battery and ultracapacitor cells, as shown in Figs. 2.4 and 2.5, respectively. In Fig. 2.3, the interfacing bridge, though can directly connect both the battery and ultracapacitor units to the DC bus, normally includes one or two DC-DC conversion stages. It should be noted that charging infrastructures are not shown in Figs. 2.1, 2.2, and 2.3. The battery unit can be charged
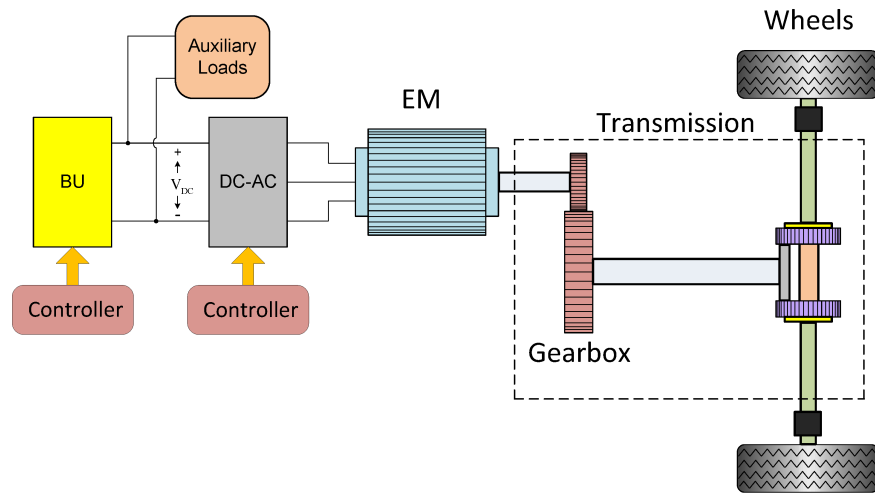
Figure 2.1: Powertrain of a Battery-only Electric Vehicle
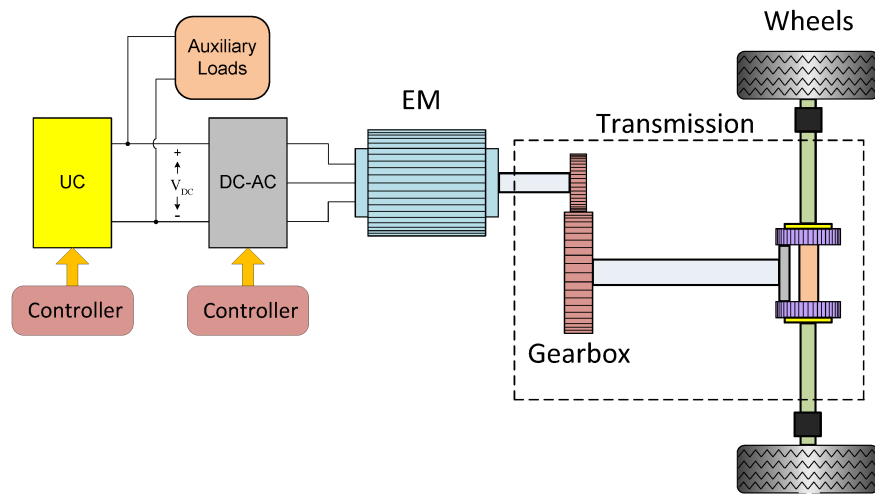
Figure 2.2: Powertrain of an Ultracapacitor-only Electric Vehicle

in two ways: onboard grid integration (for example in plug-in battery electric vehicles) and battery swap strategy. In onboard grid integration, the battery unit is plugged into the power grid (level-1, level-2, or level-3 charging scheme [34, 35]). In battery swap strategy,
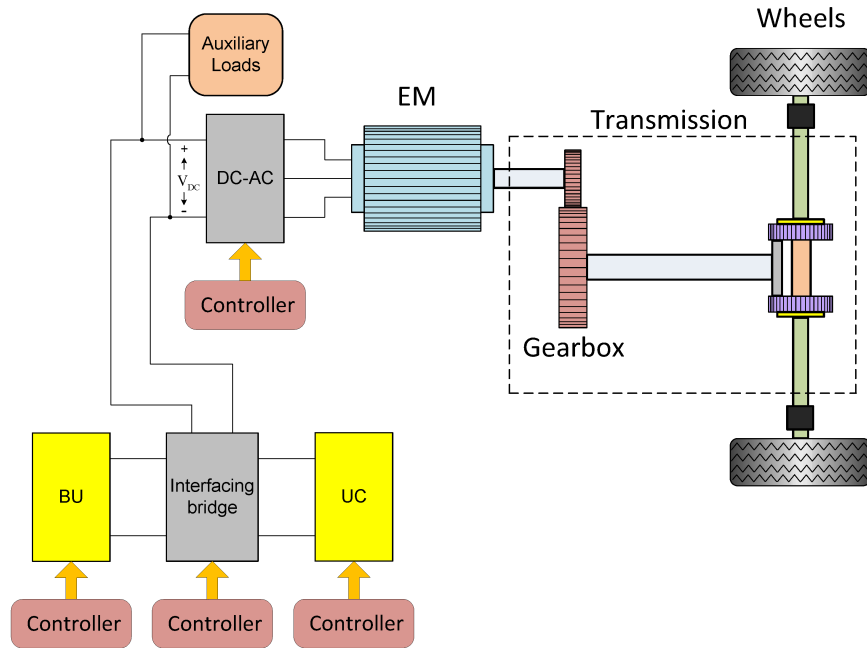
Figure 2.3: Powertrain of a Battery-Ultracapacitor Electric Vehicle

the discharged battery unit is swapped with a newly-charged one at a swapping station [36]. For the ultracapacitor unit, grid integration is the only charging method currently used in available ultracapacitor electric buses [8]. It is worth mentioning that charging the ultracapacitor units via grid integration is only carried out in the vehicles where UC is needed to be charged frequently like in ultracapacitor buses.

Figures 2.1, 2.2, and 2.3 also show the electric motor (EM) which is controlled by the DC-AC converter (inverter). The electric motor transfers the mechanical power to the wheels through the transmission system [37]. The numbers of parallel branches and series-connected cells in each branch for the battery and ultracapacitor units (N_{bp}, N_{up}, N_{bs}, and N_{us}) are found through an optimization process. In the case of battery-ultracapacitor HESS configuration, if DC-DC converters are included in the interfacing bridge, an additional

15
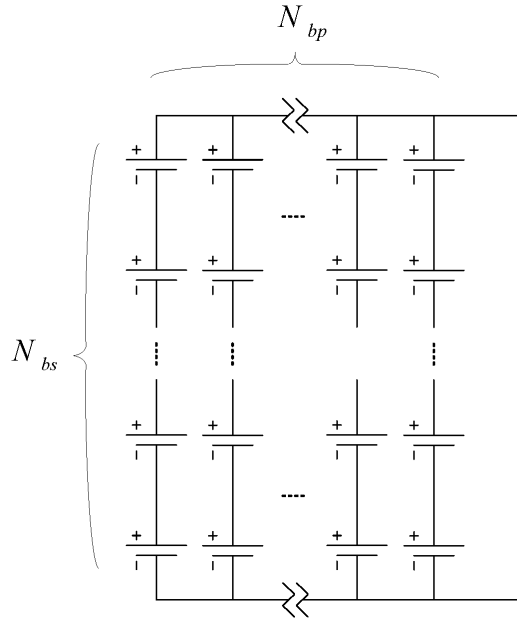
Figure 2.4: Structure of the battery unit

optimization variable accounting for the rating of one of the DC-DC converters in the bridge (it may be the only converter installed) will be added to the optimization problem. The result of optimization also determines ratings of the DC-AC converter and the electric motor.

It should be noted that the configuration shown in Figs. 2.2 has limited applications in electric vehicles. This structure cannot be implemented for a long-range vehicle. What is meant by long range is that the vehicle must be able to complete a long drive cycle with a single charge of the storage unit. The examples are Tesla Roadster and Nissan Leaf. Both of these cars can complete long ranges on a single charge of their storage units (battery packs installed). However, this objective could not be fulfilled if their storage units were just composed of ultracapacitor cells. This is due to low specific energy of ultracapacitors compared to that of batteries available in the market. If the optimization problem is solved
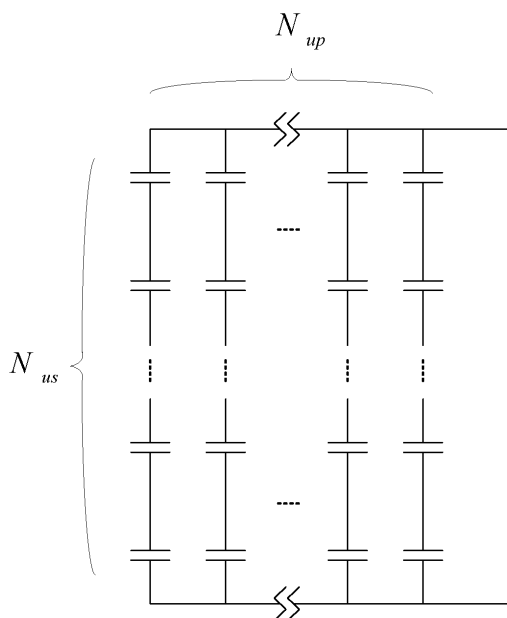
Figure 2.5: Structure of the ultracapacitor unit

based on the assumption of having only ultracapacitor cells onboard for long-range vehicles with a constraint to complete their drive cycles with a single charge, the optimization algorithm cannot converge to any solution. From the viewpoint of numerical analysis, what happens is as follows: once a random point is not found as a feasible solution due to shortage of energy available from the ultracapacitor unit to complete the drive cycle, the optimization algorithm examines the situation for a bigger size of the storage unit. However, due to large mass of the ultracapacitor cells, the power profile associated with the drive cycle will experience a significant increase as the total weight of the vehicle is raised. This implies more energy being required from the storage unit and therefore, the issue of meeting the energy constraint is aggravated in a positive feedback fashion. As a result, the algorithm cannot ever converge to a feasible solution.

2.1 Different Configurations of Interfacing Battery and Ultracapacitor Units to the DC Bus

One of the main challenges for solving the optimal sizing problem for a battery-ultracaapcitor HESS is how to interface the battery and ultracapacitor units to the DC bus. This concept has received a wide coverage in the literature. In the following, a qualitative analysis is provided on this concept.

2.1.1 Direct Connection of BU and UC to the DC Bus

Figure 2.6 shows a block diagram of direct connection of BU and UC to the DC bus. This is the simplest way of connecting battery and ultracapacitor units to the DC bus. The bold features of this configuration are as follows [3, 4, 10], [38]-[44]:

- This configuration is considerably easy to build and very cost-effective.

- The DC bus voltage experiences small and slow variations as the bus is directly clamped to the terminals of BU. This is a favourable feature for the input voltage of the DC-AC converter.
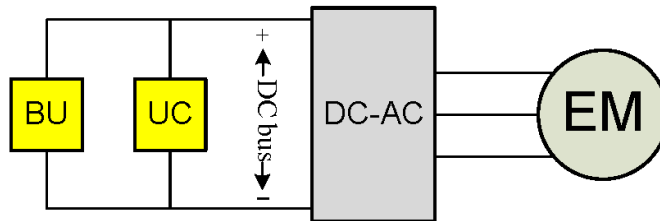
Figure 2.6: Direct connection of BU and UC to the DC bus

- The power management is straightforward as the magnitude and direction of power components associated with BU and UC are determined by their corresponding internal impedances and instantaneous value of the DC bus voltage.

- Since BU is directly connected to the DC bus, it can be exposed to large and fast variations of discharge/charge currents during acceleration/regenerative braking. This can quickly deteriorate the functionality of the battery and shorten its life.

- As the terminal voltage of UC is clamped to that of the battery unit, the terminal voltage of UC cannot vary freely and therefore, functionality of UC remains very limited, especially during acceleration and regenerative braking.

2.1.2 Partially-decoupled Interfacing of BU and UC to the DC Bus

In partially-decoupled configurations, either BU or UC is decoupled from the DC bus using a bidirectional DC-DC converter where the decoupled unit is connected on the low-voltage side. Although existence of the DC-DC converter adds to the cost and complexity of the control circuitry, this type of HESS configuration offers some important features to the system. Depending on whether BU or UC is connected directly to the DC bus, two topologies can be realized in this category. In topology I, shown in Figure 2.7, UC is connected directly to the DC bus. This configuration offers the following major advantages over the configuration of Fig. 2.6 [38, 41], [43]-[48]:

- As BU is decoupled from the DC bus, it is immune to highly-fluctuating charge/discharge currents as sharp rises and falls of the power demand during acceleration and regenerative braking events can be picked up by UC at the DC bus.
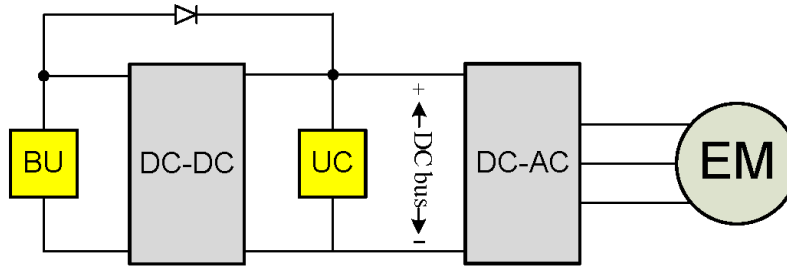
Figure 2.7: Partially-decoupled configurations: topology I

- As the battery unit is placed on the low-voltage side of the DC-DC converter, the number of series-connected battery cells is reduced. This makes voltage (charge) balancing procedure an easier task to implement for the battery cells.

It should be noted that the diode shown in Fig. 2.7 is to make sure that the DC bus voltage never falls below the terminal voltage of the battery unit installed on the low-voltage side of the DC-DC converter.

One of the drawbacks of this configuration is that the DC bus voltage may be exposed to wide fluctuations due to the fact that it is connected directly to UC terminals. This can have an adverse impact on the performance of the DC-AC converter from the viewpoint of speed control of the traction motor, especially in harsh driving conditions where UC may experience significant voltage variations over the drive cycle. This issue can be effectively resolved by proper voltage control of the DC-DC converter. However, stiff regulation of the DC bus voltage limits the functionality of ultracapacitor unit.

In topology II of partially-decoupled configurations, shown in Figure 2.8, BU is directly connected to the DC bus, while UC is decoupled from the DC bus via the bidirectional DC-DC converter. The bold features of this topology are [41], [44]-[50]:

- The DC bus does not undergo significant voltage fluctuations as it is clamped to the
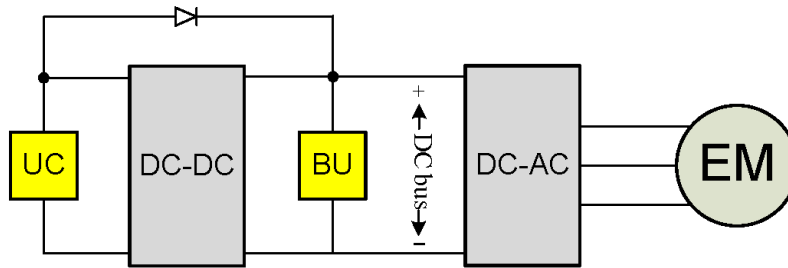
Figure 2.8: Partially-decoupled configurations: topology II

terminals of BU.

- Using the DC-DC converter, UC can operate over a wide voltage range which improves its functionality.

- Being installed directly on the DC bus, BU is exposed to large and fast-changing charge/discharge currents. This can result in shortening the life time of battery cells.

- The DC-DC converter is rated based on the power rating of UC, which is supposed to take care of sharp and large changes in the power demand. This necessitates using a high-power fast DC-DC converter which implies a large and expensive DC-DC conversion system.

- Placing the battery unit on the DC bus increases the number of series-connected battery cells. Therefore, a more complex and expensive voltage balancing circuitry is required compared to that of configuration of Fig. 2.7.

2.1.3 Fully-decoupled Configurations

In fully-decoupled configurations, BU and UC are completely decoupled from the DC bus using a power electronic-based interfacing bridge. A number of topologies fall under this category. The simplest structure is shown in Fig. 2.9 where parallel-connected BU and UC are decoupled from the DC bus by a DC-DC converter [3, 4, 10, 39, 40, 42]. Although this configuration offers an advantage in terms of the number of series-connected cells of the storage devices (from the viewpoint of voltage balancing circuits) compared to the one shown in Fig. 2.6, it still suffers from low level of functionality of UC, as it is clamped to the terminals of BU. In addition, battery life may be shortened due to occurrence of harsh driving conditions.

Figure 2.10 shows a fully-decoupled configuration in which BU and UC are interfaced to the DC bus via a multi-input DC-DC converter [44, 45]. The main drawback of multi-input converter is the complexity of control system and isolation transformer saturation.

Cascaded topologies are shown in Figs. 2.11 and 2.12 where two cascaded converters decouple BU and UC from the DC bus [3, 4, 10, 39, 40, 44, 45]. In topology I, shown in Fig. 2.11, BU is connected on the lowest voltage terminals and UC is installed at the intermediate level. This is a favorable topology as balancing the battery cells at lower
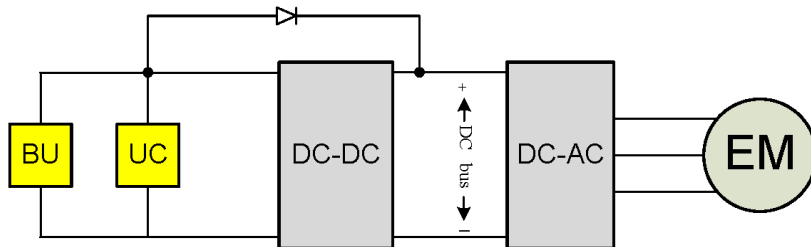
Figure 2.9: Fully-decoupled configuration with parallel connection of BU and UC

22
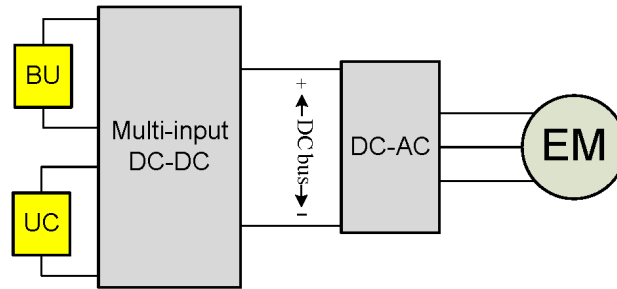
Figure 2.10: Fully-decoupled configuration with a multi-input converter
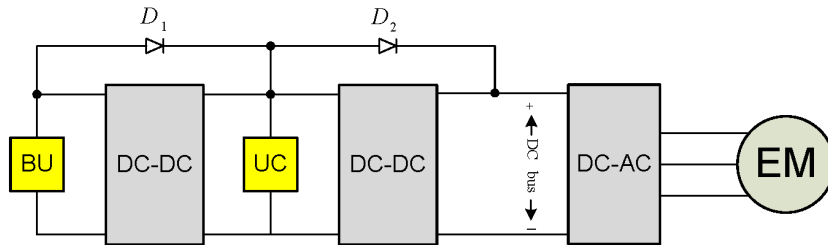
Figure 2.11: Fully-decoupled configurations with cascaded converters: topology I
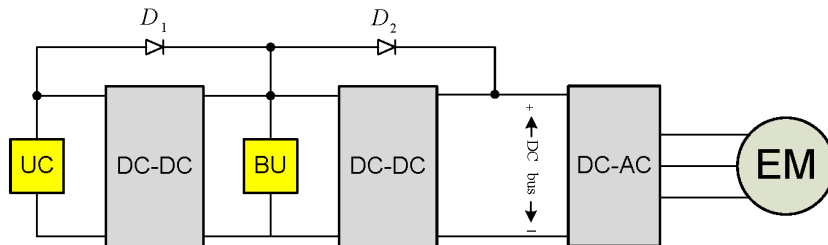
Figure 2.12: Fully-decoupled configurations with cascaded converters: topology II

voltage levels is easier and less expensive than that at higher voltage levels. In addition, the first DC-DC converter which interfaces BU to UC is rated at the power rating of BU. However, as the UC voltage is free to fluctuate at a higher voltage, significant care is needed when this topology is used. This is due to critical instability problems [51, 52]. To solve this problem, the positions of BU and UC can be exchanged as shown in Fig. 2.12.

23

In this configuration, BU is connected on the intermediate voltage level and provides a more stable voltage at the low-voltage terminals of the other converter through which BU is interfaced to the DC bus. However, this topology has its own drawbacks as balancing of battery cells at higher voltage levels is a more difficult and costly task. In addition, the cost of DC-DC converters is higher compared to that of topology I in Fig. 2.11, as both converters have to process the large and fast changes of power handled by UC.

The other fully-decoupled configuration is the parallel-converter topology shown in Fig. 2.13. This is a favorable and commonly-used topology in this category [3, 4, 10, 39, 41, 42, 45, 53]. The stability problems existing in cascaded topology are taken care of in this configuration. Besides, the converters are required to be rated separately for BU and UC, implying lower converter costs when compared with cascaded configurations. However, this configuration requires a very complex, and therefore, expensive control circuitry.
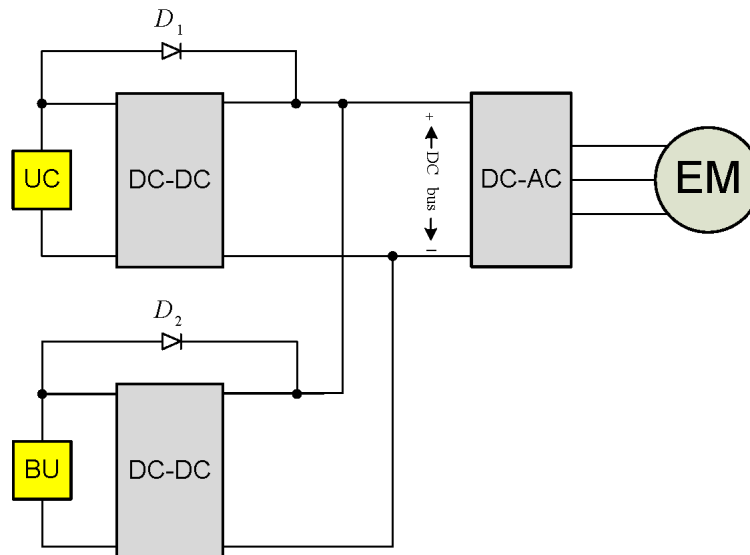
Figure 2.13: Fully-decoupled configuration with parallel converters

24

It should be noted that in the literature, different types of DC-DC converters have been discussed for interfacing the storage units to the DC bus in electric and hybrid electric vehicles. These bidirectional converters cover both non-isolated and isolated types. Some of the main examples are: Bidirectional Buck-Boost, Half-bridge, and Full-bridge converters [4, 39, 49, 54, 55]. The bidirectional Buck-Boost converter is the most commonly used DC-DC converter for applications in electric and hybrid electric vehicles, and is chosen as the interfacing bridge in the battery-ultracapacitor HESS configuration in this thesis.

2.2   Electrical Model of Battery Cell

Traditionally, rechargeable batteries have formed the building blocks of electrical energy storage systems of EVs/HEVs. Generally, an electrochemical cell is modeled as a combination of elements such as resistors, inductors, capacitors, and a voltage source [56]. To determine the components representing the electrical behavior of a cell, one of the most common methods is to apply ac currents at different frequencies to the cell and study the behaviour of the terminal voltage of the cell. If this is carried out at different operating temperatures, the impact of temperature on the behaviour of the cell can be evaluated as well [56, 57].

Various electrical models of batteries have been proposed in the literature [56]-[65]. In this thesis, the circuit diagram shown in Fig. 2.14 is used as the electrical model of the battery cells [61, 62]. This model has a variable voltage source shown as v_{oc} (open-circuit voltage) which is a function of SoC, an effective series resistance (R_{bes}), and two short- and long-transient RC branches (R_{bst}, C_{bst}, R_{blt}, and C_{blt}). The resistances and capacitances are functions of SoC as well. It should be noted that in this thesis, temperature dependence of open-circuit voltage, resistances, and capacitances has been neglected, assuming that
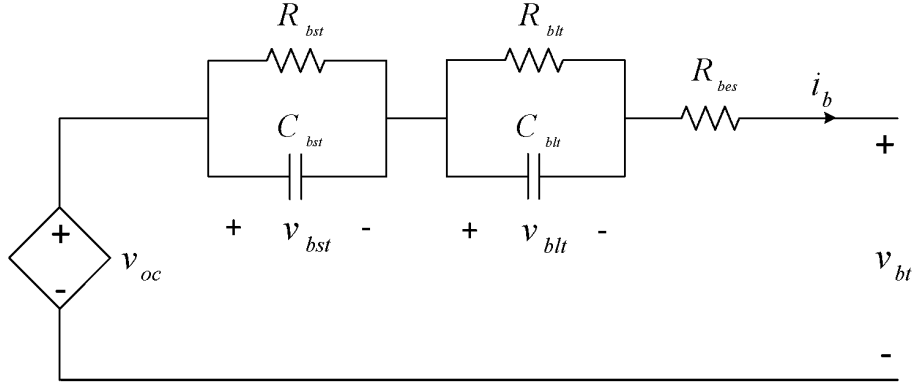
Figure 2.14: Electrical model of a battery cell [61, 62]

battery cell temperature is maintained at a constant value. For calculating the open-circuit voltage, it is required to determine SoC of the cell. There are different methods for calculating SoC such as Coulomb Counting, Monitoring Specific Gravity, and Kalman Filtering [65]-[70]. In this thesis, Coulomb Counting is used for calculating the state of charge of the battery cells. This is one of the most-widely used methods for estimation of SoC. To implement it, the battery current is integrated to calculate the charge transferred and then, the result is subtracted from the initial charge of the cell. Note that positive i_b denotes battery discharging. The mathematical model of the circuit diagram in Fig. 2.14 is represented by:

$$v_{oc} = F_b(SoC) \qquad i_b = -Q_b \frac{d(SoC)}{dt}$$

$$v_{bt} = v_{oc} - v_{bst} - v_{blt} - R_{bes}i_b$$

$$C_{bst} \frac{d\, v_{bst}}{dt} = i_b - \frac{v_{bst}}{R_{bst}}$$

$$C_{blt} \frac{d\, v_{blt}}{dt} = i_b - \frac{v_{blt}}{R_{blt}} \qquad (2.1)$$

26

where F_b is the nonlinear function representing open-circuit voltage in terms of SoC, Q_b rated capacity of the battery cell, v_{bt} the cell terminal voltage, i_b the cell discharging current, and d/dt the time-derivation operator.

2.3   Electrical Model of Ultracapacitor Cell

The concept behind an ultracapacitor is, to some extent, similar to the electrolytic capacitor in which charge separation creates an electric potential between the plates. However, due to special structure of the ultracapacitors, mainly larger equivalent surface areas on the electrodes and thinner layers of dielectric material, charge storage capacity is much larger than that of conventional capacitors [71]. In the literature, there are several electrical models for ultracapacitors [71]-[76]. In this thesis, the model shown in Fig. 2.15 is used for the purpose of simulation and optimization [75]. This model consists of a fixed capacitance (C_0), a voltage-dependent capacitance (C_1), and an effective series resistance (R_{ues}). Equation (2.2) formulates the model based on this circuit diagram.

$$v_{ut} = v_{u1} - R_{ues}i_u$$

$$\left(C_0 + C_1\right)\frac{d\ v_{u1}}{dt} = -i_u \tag{2.2}$$

where

$$C_1 = k_1 v_{u1} \tag{2.3}$$

27
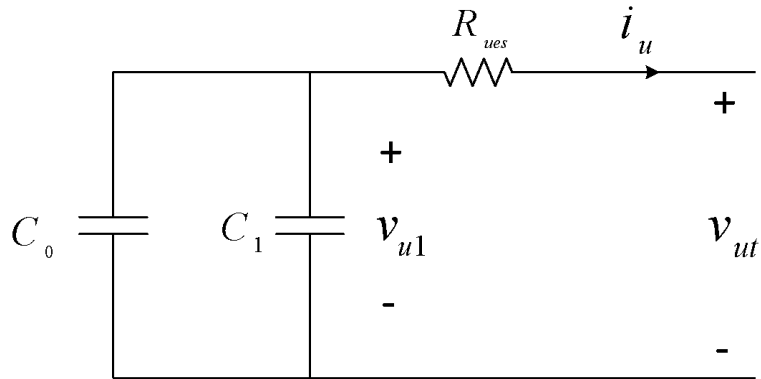
Figure 2.15: Electrical model of an ultracapacitor cell [75]

2.4 Electrical Model of DC-AC Converter

Figure 2.16 shows the circuit diagram of a three-phase IGBT-based DC-AC converter. The AC voltage sources represent the terminal voltages of the AC electric motor of the power-train. Each IGBT has been represented by a switch-diode combination. Different switching
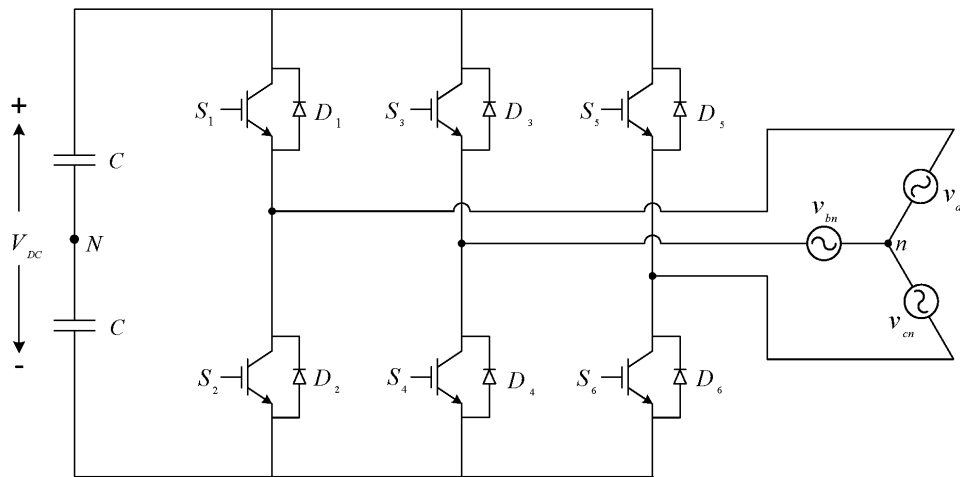
Figure 2.16: Circuit diagram of a three-phase DC-AC converter

28

techniques such as square-wave, sinusoidal pulse-width modulation (SPWM), and space vector modulation (SVM) can be applied for controlling the operation of inverter. In this thesis, SPWM has been considered as the switching technique. To implement it, three 120-degree phase-shifted sinusoidal modulating signals are compared to a triangular waveform. The intersection between each sinusoidal signal and the triangular waveform determines the instants of switching for the switches in the corresponding leg of the converter. This has been shown pictorially in Fig. 2.17 for controlling the operation of one leg of the converter. As seen in this figure, the sinusoidal modulating signal is intersected with the triangular carrier signal. Whenever the control signal is larger than the triangular waveform, the top switch of the corresponding leg is ON (the direction of load current determines whether the switch or the diode is conducting). The bottom switch is ON whenever the control signal is smaller than the triangular waveform. The dotted trace illustrates the widths of ON-state intervals for the top and bottom switches. By implementing this switching scheme, the AC voltage (with respect to the middle point N) will be a pulsed waveform fluctuating between $-0.5V_{DC}$ and $0.5V_{DC}$. As the frequency of switching is increased, the low-order harmonic
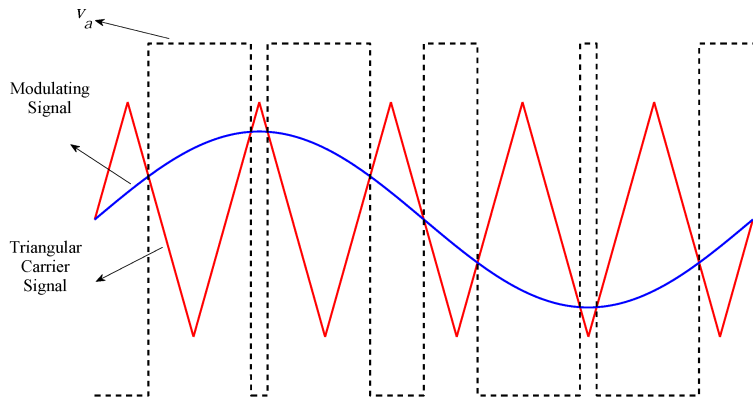
Figure 2.17: PWM switching signal generation

components of the pulsed waveform are reduced. However, it should be noted that the switching frequency cannot be significantly high as it increases the switching losses of the converter.

To implement a mathematical model for the inverter, each switch-diode combination is represented by an ideal switch and an ideal diode each in series with a resistance and a voltage source, as shown in Fig. 2.18 [77]-[79]. Under SPWM, when the AC current (i_a) is positive, the AC side voltage (v_a) is expressed as:

$$v_a = d\left(\frac{V_{DC}}{2} - R_{sw}i_a - V_{sw}\right) + (1-d)\left(-\frac{V_{DC}}{2} - R_D i_a - V_D\right) \tag{2.4}$$

where d is the duty ratio of S_1. For the negative current $(i_a < 0)$, one has:

$$v_a = d\left(\frac{V_{DC}}{2} - R_D i_a + V_D\right) + (1-d)\left(-\frac{V_{DC}}{2} - R_{sw}i_a + V_{sw}\right) \tag{2.5}$$

Considering $m = (2d - 1)$ as the modulating signal normalized to the peak value of the
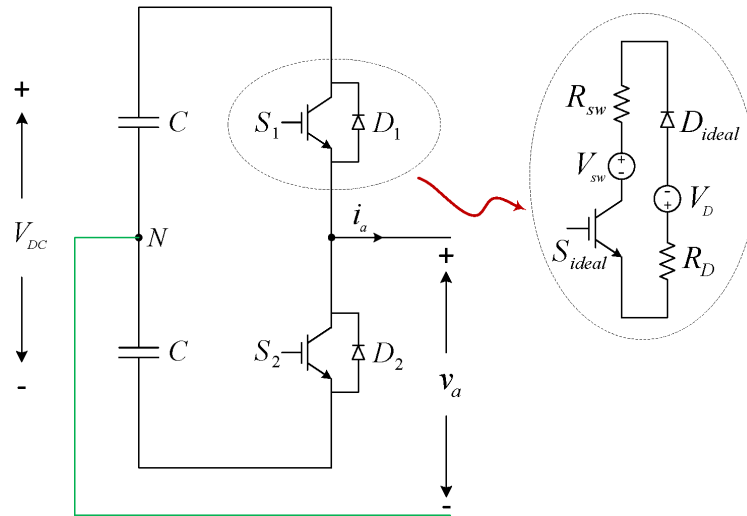
Figure 2.18: Electrical model of one leg of the DC-AC converter

30

triangular waveform, one gets:

$$v_a = m\left(\frac{V_{DC} - V_{sw} + V_D}{2}\right) - \left(\frac{R_{sw} + R_D}{2}\right)i_a -$$

$$\left(\frac{V_{sw} + V_D}{2} + m\left(\frac{R_{sw} - R_D}{2}\right)i_a\right)sgn(i_a) \tag{2.6}$$

where

$$sgn(x) = \begin{cases} -1 & \text{if } x < 0 \\ 0 & \text{if } x = 0 \\ 1 & \text{if } x > 0 \end{cases} \tag{2.7}$$

The AC-side average power of the first leg of the inverter is calculated by:

$$P_a = \frac{1}{2\pi} \int_\delta^{2\pi+\delta} \left(v_a i_a\right) d\theta \tag{2.8}$$

where δ is an arbitrary angle. With the switching frequency large enough and considering linear modulation, we can assume $m = M\sin(\theta)$ where M is the modulating index. Considering sinusoidal current on the AC-side of the inverter, i.e., $i_a = I\sin(\theta - \phi)$ where I and ϕ are the amplitude of the current and the angle difference between the current and the modulating signal, respectively, the AC-side power of the first leg of the inverter is calculated as:

$$P_a = \left(\frac{V_{DC} - V_{sw} + V_D}{4\pi}\right)MI \int_\delta^{2\pi+\delta} \left(\sin(\theta)\sin(\theta - \phi)\right) d\theta -$$

$$\left(\frac{R_{sw} + R_D}{4\pi}\right)I^2 \int_\delta^{2\pi+\delta} \left(\sin(\theta - \phi)\right)^2 d\theta -$$

$$\left(\frac{V_{sw} + V_D}{4\pi}\right)I \int_\delta^{2\pi+\delta} \left(\sin(\theta - \phi)sgn\left(\sin(\theta - \phi)\right)\right) d\theta -$$

31

$$\left(\frac{R_{sw} - R_D}{4\pi}\right) MI^2 \int_{\delta}^{2\pi+\delta} \left(\sin(\theta)\Big(\sin(\theta-\phi)\Big)^2 sgn\Big(\sin(\theta-\phi)\Big)\right) d\theta \qquad (2.9)$$

Different integration terms in (2.9) are calculated as:

$$\int_{\delta}^{2\pi+\delta} \Big(\sin(\theta)\sin(\theta-\phi)\Big) d\theta = \pi\cos(\phi)$$

$$\int_{\delta}^{2\pi+\delta} \Big(\sin(\theta-\phi)\Big)^2 d\theta = \pi$$

$$\int_{\delta}^{2\pi+\delta} \Big(\sin(\theta-\phi)sgn\Big(\sin(\theta-\phi)\Big)\Big) d\theta = 2\int_{\phi}^{\pi+\phi} \Big(\sin(\theta-\phi)\Big) d\theta = 4$$

$$\int_{\delta}^{2\pi+\delta} \left(\sin(\theta)\Big(\sin(\theta-\phi)\Big)^2 sgn\Big(\sin(\theta-\phi)\Big)\right) d\theta =$$
$$2\int_{\phi}^{\pi+\phi} \left(\sin(\theta)\Big(\sin(\theta-\phi)\Big)^2\right) d\theta = \frac{8}{3}\cos(\phi) \qquad (2.10)$$

Substituting from (2.10) into (2.9), one has:

$$P_a = \left(\frac{V_{DC} - V_{sw} + V_D}{4}\right) MI\cos(\phi) - \left(\frac{R_{sw} + R_D}{4}\right) I^2$$

$$-\left(\frac{V_{sw} + V_D}{\pi}\right) I - 2\left(\frac{R_{sw} - R_D}{3\pi}\right) MI^2 \cos(\phi) \qquad (2.11)$$

The output power calculated by (2.11) only includes the conduction loss of the switch-diode combinations. There is also switching loss associated with each switch in the inverter legs. It can be shown that during each on-off switching process, the switching loss (p_{sw}) of the corresponding semiconductor device in Fig. 2.18 is [78, 79]:

$$p_{sw} = k_{sw}V_{DC}|i_a|(t_{on} + t_{off})f_{sw} \qquad (2.12)$$

where k_{sw} is a constant coefficient in the range of $[\frac{1}{6}, \frac{1}{2}]$, t_{on} and t_{off} the turn-on and turn-off cross-over times, respectively, and f_{sw} the switching frequency. Considering the fact that the switch S_1 (S_2) bears the switching loss only when i_a is positive (negative), and $i_a = I\sin(\theta - \phi)$, the average switching loss for the converter leg (P_{sw-a}) is:

$$P_{sw-a} = \frac{k_{sw}\left(V_{DC}I(t_{on} + t_{off})f_{sw}\right)}{\pi} \int_{\phi}^{\pi+\phi} \left(\sin(\theta - \phi)\right) d\theta =$$

$$\frac{2k_{sw}\left(V_{DC}I(t_{on} + t_{off})f_{sw}\right)}{\pi} \tag{2.13}$$

From (2.11) and (2.13), the total losses of the three-phase inverter is calculated to be:

$$P_{loss} = 3\left(\left(\frac{V_{sw} - V_D}{4}\right)MI\cos(\phi) + \left(\frac{R_{sw} + R_D}{4}\right)I^2 + \left(\frac{V_{sw} + V_D}{\pi}\right)I+\right.$$

$$\left. 2\left(\frac{R_{sw} - R_D}{3\pi}\right)MI^2\cos(\phi) + \frac{2k_{sw}\left(V_{DC}I(t_{on} + t_{off})f_{sw}\right)}{\pi}\right) \tag{2.14}$$

To calculate the Fourier coefficients for the fundamental component of the AC-side voltage, we have:

$$a_1 = \frac{1}{\pi}\int_{\delta}^{2\pi+\delta}\left(v_a\cos(\theta)\right) d\theta \qquad b_1 = \frac{1}{\pi}\int_{\delta}^{2\pi+\delta}\left(v_a\sin(\theta)\right) d\theta \tag{2.15}$$

Substituting from (2.6) into (2.15) considering $m = M\sin(\theta)$ and $i_a = I\sin(\theta - \phi)$, we get:

$$a_1 = \left(\frac{V_{DC} - V_{sw} + V_D}{2\pi}\right)M \int_{\delta}^{2\pi+\delta}\left(\sin(\theta)\cos(\theta)\right) d\theta-$$

$$\left(\frac{R_{sw} + R_D}{2\pi}\right)I \int_{\delta}^{2\pi+\delta}\left(\sin(\theta - \phi)\cos(\theta)\right) d\theta-$$

33

$$\left(\frac{V_{sw}+V_D}{2\pi}\right)\int_{\delta}^{2\pi+\delta}\left(\cos(\theta)sgn\Big(\sin(\theta-\phi)\Big)\right)d\theta-$$

$$\left(\frac{R_{sw}-R_D}{2\pi}\right)MI\int_{\delta}^{2\pi+\delta}\left(\sin(\theta)\sin(\theta-\phi)\cos(\theta)sgn\Big(\sin(\theta-\phi)\Big)\right)d\theta \qquad (2.16)$$

and,

$$b_1=\left(\frac{V_{DC}-V_{sw}+V_D}{2\pi}\right)M\int_{\delta}^{2\pi+\delta}\left(\sin(\theta)\right)^2 d\theta-$$

$$\left(\frac{R_{sw}+R_D}{2\pi}\right)I\int_{\delta}^{2\pi+\delta}\left(\sin(\theta-\phi)\sin(\theta)\right)d\theta-$$

$$\left(\frac{V_{sw}+V_D}{2\pi}\right)\int_{\delta}^{2\pi+\delta}\left(\sin(\theta)sgn\Big(\sin(\theta-\phi)\Big)\right)d\theta-$$

$$\left(\frac{R_{sw}-R_D}{2\pi}\right)MI\int_{\delta}^{2\pi+\delta}\left(\left(\sin(\theta)\right)^2\sin(\theta-\phi)sgn\Big(\sin(\theta-\phi)\Big)\right)d\theta \qquad (2.17)$$

The integration terms in (2.16) and (2.17) are calculated as:

$$\int_{\delta}^{2\pi+\delta}\left(\sin(\theta)\cos(\theta)\right)d\theta=0$$

$$\int_{\delta}^{2\pi+\delta}\left(\sin(\theta)\right)^2 d\theta=\pi$$

$$\int_{\delta}^{2\pi+\delta}\left(\sin(\theta-\phi)\cos(\theta)\right)d\theta=-\pi\sin(\phi)$$

$$\int_{\delta}^{2\pi+\delta}\left(\sin(\theta-\phi)\sin(\theta)\right)d\theta=\pi\cos(\phi)$$

34

$$\int_{\delta}^{2\pi+\delta} \left(\cos(\theta) sgn\left(\sin(\theta - \phi) \right) \right) d\theta = 2 \int_{\phi}^{\pi+\phi} \left(\cos(\theta) \right) d\theta = -4\sin(\phi)$$

$$\int_{\delta}^{2\pi+\delta} \left(\sin(\theta) sgn\left(\sin(\theta - \phi) \right) \right) d\theta = 2 \int_{\phi}^{\pi+\phi} \left(\sin(\theta) \right) d\theta = 4\cos(\phi)$$

$$\int_{\delta}^{2\pi+\delta} \left(\sin(\theta) \sin(\theta - \phi) \cos(\theta) sgn\left(\sin(\theta - \phi) \right) \right) d\theta =$$
$$2 \int_{\phi}^{\pi+\phi} \left(\sin(\theta) \sin(\theta - \phi) \cos(\theta) \right) d\theta = -\frac{2}{3}\sin(2\phi)$$

$$\int_{\delta}^{2\pi+\delta} \left(\left(\sin(\theta) \right)^2 \sin(\theta - \phi) sgn\left(\sin(\theta - \phi) \right) \right) d\theta =$$
$$2 \int_{\phi}^{\pi+\phi} \left(\left(\sin(\theta) \right)^2 \sin(\theta - \phi) \right) d\theta = 2 + \frac{2}{3}\cos(2\phi) \qquad (2.18)$$

Substituting from (2.18) into (2.16) and (2.17), one gets:

$$a_1 = \left(\frac{R_{sw} + R_D}{2} \right) I \sin(\phi) + 2 \left(\frac{V_{sw} + V_D}{\pi} \right) \sin(\phi) + \left(\frac{R_{sw} - R_D}{3\pi} \right) MI \sin(2\phi) \qquad (2.19)$$

and,

$$b_1 = \left(\frac{V_{DC} - V_{sw} + V_D}{2} \right) M - \left(\frac{R_{sw} + R_D}{2} \right) I \cos(\phi) -$$

$$2 \left(\frac{V_{sw} + V_D}{\pi} \right) \cos(\phi) - \left(\frac{R_{sw} - R_D}{3\pi} \right) MI \left(3 + \cos(2\phi) \right) \qquad (2.20)$$

Using a_1 and b_1, the rms value of the fundamental component of v_a will be:

$$V_{a1} = \sqrt{\frac{a_1^2 + b_1^2}{2}} \qquad (2.21)$$

2.5   Electrical Model of Traction Motor

Different types of electric motors (DC and AC) have been used in variable speed drives. For vehicular applications, AC motors are always preferred against DC motors due to reasons such as higher efficiency, lower maintenance requirement, and higher volumetric power density. Among different AC machines, induction and permanent magnet synchronous motors are the most commonly-used options for electro-mechanical conversion in electrified powertrains (examples are induction motor in Tesla Roadster and permanent magnet motor in Nissan Leaf). In this thesis, induction machines have been considered as the traction motors of the electric powertrains shown in Figs. 2.1, 2.2, and 2.3.

Figure 2.19 shows the electrical circuit diagram of one phase of an induction machine. It includes the stator resistance (R_s) and leakage inductance $(L_{\ell s})$, the magnetizing inductance (L_m), the core resistance (R_c), and the rotor resistance (R_r) and leakage inductance $(L_{\ell r})$ referred to the stator frame [80]. In Fig. 2.19, s represents the rotor slip defined as:

$$s = 1 - \frac{\omega_r}{\omega_{sy}} \qquad \omega_{sy} = \frac{4\pi}{N_p}f_s \qquad \omega_r = \frac{\pi}{30}n_r \qquad (2.22)$$
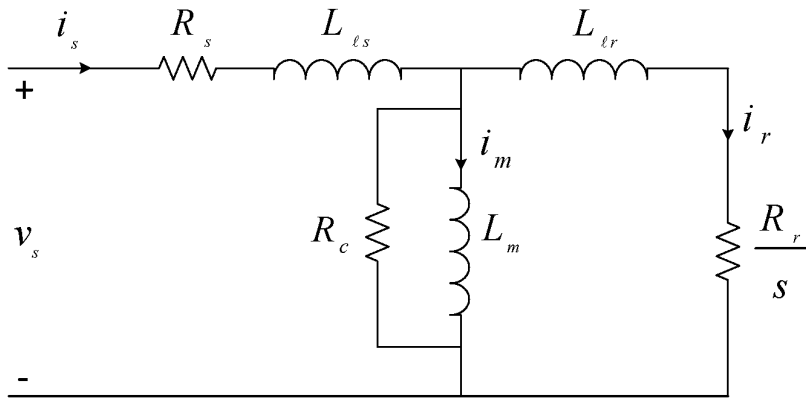
Figure 2.19: Electrical model of an induction machine

36

where ω_{sy} is the synchronous speed, ω_r and n_r the mechanical angular and rpm velocities of the rotor shaft, respectively, f_s the frequency of stator voltage, and N_p the number of machine poles. It should be noted that, in this thesis, following a common practice in the analysis of the electrical model of induction machines, R_c is neglected as shown in Fig. 2.20 [80]. Let's assume that the stator terminals are connected to a sinusoidal voltage source with phase rms value of V_s and frequency of f_s. To calculate the mechanical torque and power of the induction machine, one can convert the circuit diagram of Fig. 2.20 to its Thevenin equivalent model shown in Fig. 2.21, where

$$R_{th} = \frac{R_s \left(2\pi L_m f_s \right)^2}{R_s^2 + \left(2\pi \left(L_{\ell s} + L_m \right) f_s \right)^2}$$

$$L_{th} = \frac{R_s^2 + L_{\ell s} \left(L_{\ell s} + L_m \right) \left(2\pi f_s \right)^2}{R_s^2 + \left(2\pi \left(L_{\ell s} + L_m \right) f_s \right)^2} L_m$$
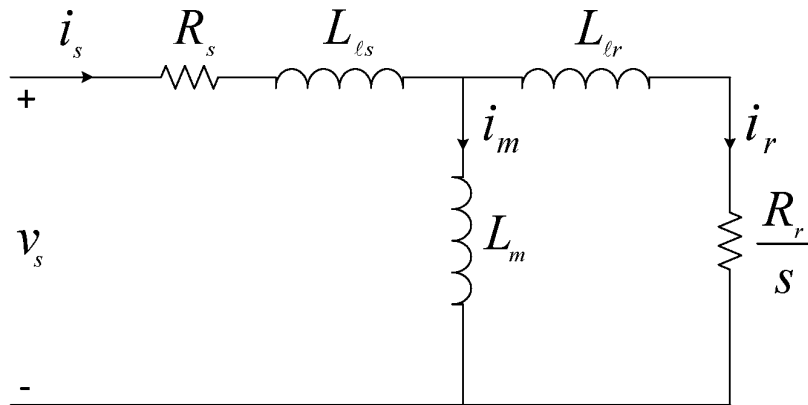
Figure 2.20: Electrical model of the induction machine neglecting R_c
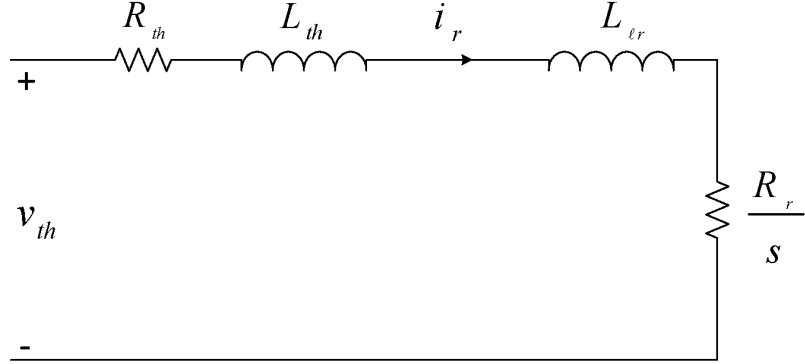
Figure 2.21: Thevenin equivalent model of the induction machine

$$V_{th} = \frac{2\pi L_m f_s}{\sqrt{R_s^2 + \left(2\pi\left(L_{\ell s} + L_m\right) f_s\right)^2}} V_s \qquad (2.23)$$

In (2.23), V_{th} is the rms value of the Thevenin voltage (v_{th}). Using the Thevenin equivalent model, the rms value of the rotor current (I_r) is calculated as:

$$I_r = \frac{sV_{th}}{\sqrt{\left(sR_{th} + R_r\right)^2 + s^2\left(2\pi\left(L_{th} + L_{\ell r}\right) f_s\right)^2}} \qquad (2.24)$$

Using (2.24), the 3-phase airgap power (P_{ag}), and rotor mechanical power (P_{mech}) and torque (T_{mech}) are:

$$P_{ag} = \frac{3R_r}{s} I_r^2 = \frac{3R_r s V_{th}^2}{\left(sR_{th} + R_r\right)^2 + s^2\left(2\pi\left(L_{th} + L_{\ell r}\right) f_s\right)^2}$$

$$P_{mech} = P_{ag} - 3R_r I_r^2 = (1 - s)P_{ag} = \frac{3R_r s(1 - s)V_{th}^2}{\left(sR_{th} + R_r\right)^2 + s^2\left(2\pi\left(L_{th} + L_{\ell r}\right) f_s\right)^2}$$

$$T_{mech} = \frac{P_{mech}}{\omega_r} = \frac{3R_r s V_{th}^2}{\omega_{sy}\left(\left(sR_{th} + R_r\right)^2 + s^2\left(2\pi\left(L_{th} + L_{\ell r}\right)f_s\right)^2\right)} \tag{2.25}$$

It should be noted that in real induction machines, there always exist core, friction, and windage losses, which affect the mechanical power and torque obtained by (2.25).

When Induction motors are used in variable speed drives (as in the powertrains of electric and hybrid electric vehicles), they are normally controlled in three different regions with respect to their operating frequency. Figure 2.22 shows the three regions of operation with their corresponding torque-speed and power-speed characteristic curves. The first region is Constant Torque in which the maximum value of the mechanical torque remains constant. This is a great advantage of electric motors for the electric powertrains where the vehicle can benefit from the maximum available torque during full acceleration at zero or low speeds. It can bo shown that for every operating frequency of the stator, the maximum torque occurs at:

$$s_{max} = \frac{R_r}{\sqrt{R_{th}^2 + \left(2\pi\left(L_{\ell r} + L_{th}\right)f_s\right)^2}} \tag{2.26}$$

Substituting for s in (2.25) from (2.26), one gets:

$$T_{max} = \frac{3V_{th}^2}{2\omega_{sy}\left(R_{th} + \sqrt{R_{th}^2 + \left(2\pi\left(L_{\ell r} + L_{th}\right)f_s\right)^2}\right)} \tag{2.27}$$

At fairly high values of stator frequency, the effect of stator resistance in Fig. 2.20 becomes negligible compared to that of magnetizing and stator leakage inductive reactances. Therefore,

$$L_{th} \approx \frac{L_{\ell s} L_m}{L_{\ell s} + L_m} \qquad V_{th} \approx \frac{L_m}{L_{\ell s} + L_m} V_s \qquad \left(2\pi\left(L_{\ell r} + L_{th}\right)f_s\right) >> R_{th} \tag{2.28}$$
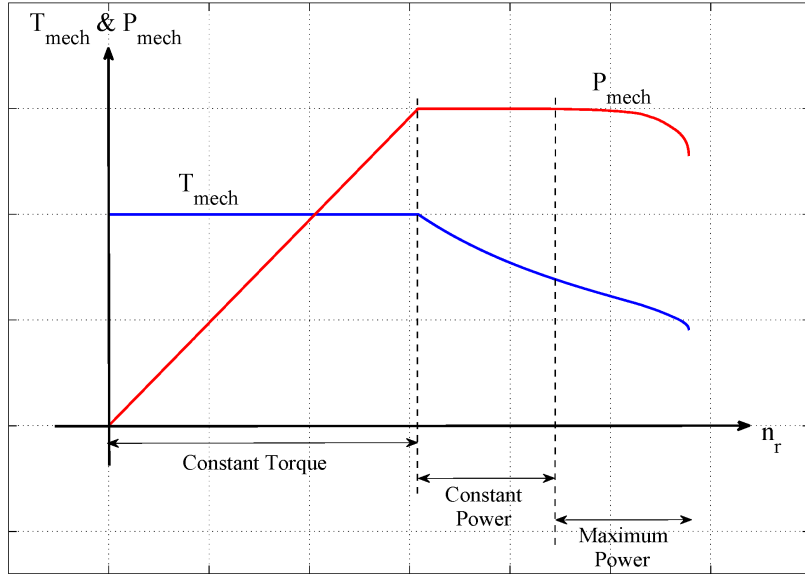
Figure 2.22: Regions of operation of an induction motor

Considering (2.28) and substituting for ω_{sy} from (2.22), (2.27) can be rewritten as:

$$T_{max} \approx \left(\frac{3N_p L_m^2}{(16\pi^2)\left(L_{\ell s} + L_m\right)\left(L_{\ell r}L_{\ell s} + L_{\ell r}L_m + L_{\ell s}L_m\right)} \right)\left(\frac{V_s}{f_s}\right)^2 \qquad (2.29)$$

During motoring operation, as the rotor speed increases, the synchronous speed, and so the stator frequency, need to be raised in order to keep the slip positive. Equation (2.29) shows that with an increase in the stator frequency, the amplitude of the terminal voltage is required to go up in order to keep the maximum torque constant. This procedure is fulfilled by controlling the DC-AC converter. Since there is always a limit on the *rms* value of the stator terminal voltage (the AC-side voltage of the inverter), the maximum torque cannot be kept constant in an unlimited frequency range. The frequency at which the terminal voltage reaches its maximum amplitude is called the base frequency. Beyond the base frequency, the terminal voltage bears its maximum amplitude while the speed of

40
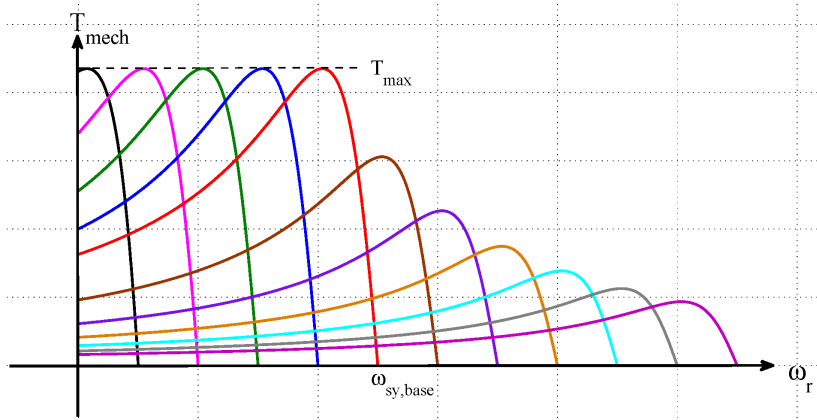
Figure 2.23: Torque-speed characteristic curves of an induction motor

machine may still increase. Figure 2.23 shows general torque-speed characteristic curves of an induction motor for different stator frequencies. As seen in this figure, the induction motor can deliver its maximum torque as long as the synchronous speed is below $\omega_{sy,base}$. Above this point, the *rms* value of the stator terminal voltage is fixed and thus, the maximum torque decreases as the rotor speed goes up. Normally, after the Constant Torque region, the machine is controlled under Constant Power condition. The Constant Power region is limited as the maximum power of the induction machine drops at high frequencies due to high impedances of the stator and rotor circuits. Therefore, at very high speeds, the induction machine is operated in a new region named Maximum Power in which the motor can deliver its maximum available power on the rotor shaft. As the speed of motor increases, this maximum available power drops. Since, normally, the load torque and load power increase with the shaft speed, there is a specific velocity after which the load power is beyond what can be delivered by the induction motor. This point refers to maximum speed of the motor which determines the maximum speed of vehicle in electric cars.

41

To calculate the stator current and the input power factor, one needs to formulate the stator terminal voltage (v_s) in terms of i_s. Using KCL in Fig. 2.20, the stator current i_s is expressed in terms of i_r as:

$$i_s = i_r + \left(\frac{\frac{R_r}{s} + j\left(2\pi L_{\ell r} f_s\right)}{j\left(2\pi L_m f_s\right)} \right) i_r = \left(1 + \frac{L_{\ell r}}{L_m} - j\left(\frac{R_r}{2\pi s L_m f_s}\right)\right) i_r \tag{2.30}$$

Defining A_r and B_r as:

$$A_r = 1 + \frac{L_{\ell r}}{L_m} \qquad B_r = \frac{R_r}{2\pi L_m f_s} \tag{2.31}$$

Then, one gets:

$$i_s = \left(A_r - j\left(\frac{B_r}{s}\right)\right) i_r \qquad I_s = \sqrt{A_r^2 + \left(\frac{B_r}{s}\right)^2}\, I_r \tag{2.32}$$

Using KVL in Fig. 2.20,

$$v_s = \left(R_s + j\left(2\pi L_{\ell s} f_s\right)\right) i_s + \left(\frac{R_r}{s} + j\left(2\pi L_{\ell r} f_s\right)\right) i_r \tag{2.33}$$

Substituting for i_r from (2.32), one has:

$$v_s = \left(R_s + j\left(2\pi L_{\ell s} f_s\right) + \frac{\frac{R_r}{s} + j\left(2\pi L_{\ell r} f_s\right)}{A_r - j\left(\frac{B_r}{s}\right)} \right) i_s \tag{2.34}$$

Then, the input impedance (Z_{in}) is defined as:

$$Z_{in} = \frac{v_s}{i_s} = \frac{R_s A_r + \frac{R_r A_s}{s} + j\left(2\pi\left(L_{\ell s} A_r + L_{\ell r}\right) f_s - \frac{R_s B_r}{s} \right)}{A_r - j\left(\frac{B_r}{s}\right)} \tag{2.35}$$

42

where

$$A_s = 1 + \frac{L_{\ell s}}{L_m} \tag{2.36}$$

Simplifying Z_{in}, the real and imaginary parts of the input impedance are:

$$Re\left(Z_{in}\right) = \frac{R_s A_r^2 + \dfrac{R_r}{s} + R_s\left(\dfrac{B_r}{s}\right)^2}{A_r^2 + \left(\dfrac{B_r}{s}\right)^2} \tag{2.37}$$

$$Im\left(Z_{in}\right) = \frac{\dfrac{R_r A_s B_r}{s^2} + 2\pi\left(L_{\ell s} A_r + L_{\ell r}\right) A_r f_s}{A_r^2 + \left(\dfrac{B_r}{s}\right)^2}$$

where $Re(Z_{in})$ and $Im(Z_{in})$ represent the real and imaginary parts of the impedance Z_{in}. The input power factor $(\cos(\phi))$ is calculated using (2.37) as:

$$\cos(\phi) = \frac{Re\left(Z_{in}\right)}{\sqrt{\left(Re\left(Z_{in}\right)\right)^2 + \left(Im\left(Z_{in}\right)\right)^2}} \tag{2.38}$$

where ϕ is the angle difference between v_s and i_s. The expressions for the rms value of stator current and the power factor given by (2.32) and (2.38), respectively, are used in determining the inverter losses and the fundamental component of the inverter AC-side voltage discussed in Section 2.4. Note that when the induction motor is fed from a voltage source inverter, v_s is the fundamental component of the inverter output and f_s is the corresponding frequency.

2.6 Model of Transmission System

The transmission system is responsible for transferring the mechanical torque of the motor shaft to the wheels during motoring operation and vice versa, when regenerative braking

takes place. In this thesis, the transmission system is modelled by a constant-efficiency gearbox with a fixed gear ratio of N_g. The mechanical torques of the motor shaft (T_{mech}) and the wheels (T_{wh}) are related by:

$$T_{wh} = \left(\gamma\eta_g + \frac{1-\gamma}{\eta_g}\right)N_gT_{mech} \tag{2.39}$$

where γ assumes values of 1 and 0 for motoring and regenerative braking operations, respectively, and η_g is the efficiency of gearbox. The torque of the wheels is calculated as [81]:

$$T_{wh} = \left(M_t\left(\frac{dv}{dt} + g\sin(\sigma) + \mu g\cos(\sigma)\right) + \frac{1}{2}C_d\rho_aA_f\left(v+v_w\right)^2\right)r_{wh} \tag{2.40}$$

where v is the vehicle velocity, M_t the total vehicle mass, g the gravitational acceleration, σ the road grade, μ the friction coefficient, C_d the drag coefficient, ρ_a the air density, A_f the equivalent frontal area of the vehicle, v_w the component of wind speed opposing vehicle's movement, and r_{wh} the wheels' radius. In this paper, friction coefficient is variable and a function of tire pressure (Pr) and vehicle velocity as:

$$\mu = 0.005 + \frac{0.14696}{Pr} + \left(\frac{1}{5526.9}\right)\left(\frac{v^2}{Pr}\right) \tag{2.41}$$

2.7 Summary

In this chapter, schematic diagrams of powertrains of battery-only, ultracapacitor-only, and battery-ultracapacitor electric vehicles were discussed with a detailed qualitative analysis provided for different topologies of interfacing battery and ultracapacitor units to the DC bus in a configuration. The chapter also provided mathematical models for different components of the powertrain, i.e., battery and ultracapacitor cells, DC-AC converter, traction motor, and transmission system, used in this thesis.

Chapter 3

Implementation of the Optimization Platform

To solve the problem of optimal sizing of the storage systems in powertrains of electric vehicles, an optimization platform is required. This platform includes formulation of the optimization problem as well as optimization technique used to solve the problem. In the followings, implementation of this platform is discussed. It should be noted that when discussing the optimal sizing of the storage system for a battery-ultracapacitor HESS configuration, the problem is addressed only for the configuration shown in Fig. 2.7. The reason is that through qualitative analysis based on literature review and considering cons and pros of each of the existing topologies (discussed in Chapter 2), partially-decoupled configuration (type I) is chosen as the most promising topology for interfacing the battery and ultracapacitor units to the DC bus, taking flexibility of power control, cost of the interfacing bridge, and life of the battery cells into account.

3.1 Formulation of the Problem

Optimal sizing of the storage system in the powertrain of an electric vehicle is a constrained optimization problem. Equation (3.1) presents formulation of the optimization problem in its general form.

$$
\begin{aligned}
&Minimize \quad f_{obj}(X, \zeta) \\
&Subject\ to \\
&\qquad H_{e,i}(X, \zeta) = 0 \quad i = 1, 2, \ldots, N_e \\
&\qquad H_{ine,j}(X, \zeta) \leq 0 \quad j = 1, 2, \ldots, N_{ine}
\end{aligned}
\tag{3.1}
$$

where ζ is the set of inputs, X the set of optimization variables, f_{obj} the objective function, $H_{e,i}$ the ith equality constraint, $H_{ine,j}$ the jth inequality constraint, and N_e and N_{ine} the numbers of equality and inequality constraints, respectively, defined in the following subsections.

3.1.1 Set of Inputs

The inputs to the system are the speed-versus-time profile (drive cycle) for which the storage system is being optimally sized, prices of the battery and ultracapacitor cells in US dollars (C_b and C_u, respectively), price per kW of the DC-DC converter in US dollars (C_{con}), and the parameters required to calculate the power demand, i.e.,

$$
P_d = \frac{T_{wh}}{r_{wh}} v
\tag{3.2}
$$

where T_{wh} is the torque on the wheels calculated using (2.40).

3.1.2 Optimization Variables

The optimization variables vary depending on the configuration of the storage system. In any case, they include the numbers of parallel branches of the storage devices (battery and/or ultracapacitor) and series-connected cells in each branch (N_{bp}, N_{up}, N_{bs} and N_{us}, respectively). It should be noted that if the powertrain includes the battery-ultracapacitor HESS configuration, power rating of the DC-DC converter (P_{con}) is also an optimization variable.

3.1.3 Objective Function

In this thesis, for the cases of battery-only and ultracapacitor-only configurations, the objective functions (f_{obj}) are the numbers of battery and ultracapacitor cells, as formulated by (3.3) and (3.4), respectively.

$$f_{obj} = N_{bs}N_{bp} \tag{3.3}$$

$$f_{obj} = N_{us}N_{up} \tag{3.4}$$

For the battery-ultracapacitor HESS, the cost of system formulated in (3.5) is considered as the objective function. It should be noted that in the cases of battery-only and ultracapacitor-only configurations, the objective functions can also be formulated based on the cost of storage units. However, as there is only one type of storage device in either of these two configurations, the results of optimization do not change with the choice of cell prices. This is due to the fact that in the battery-only and ultracapacitor-only configurations, no matter what the cell prices are, the results of optimization correspond to

minimum numbers of the cells which are required to meet the power and energy require-ments of the vehicle, while respecting all the constraints over the course of the drive cycle. Considering the fact that the costs of BU and UC are simply the numbers of battery and ultracapacitor cells multiplied by the cell prices, minimum numbers of the cells found as the optimal sizes of the storage units correspond to minimum costs of the battery and ultracapacitor units, as well. This is not the case for the battery-ultracapacitor HESS as the result of optimization can change depending on the values of prices considered for the battery and ultracapacitor cells and the rating of the DC-DC converter.

$$f_{obj} = N_{swap}N_{bs}N_{bp}C_b + N_{us}N_{up}C_u + P_{con}C_{con} \tag{3.5}$$

In (3.5) N_{swap} is the number of battery units used when swapping strategy is considered in solving the optimization problem. In the case where there is no battery swapping strategy, $N_{swap} = 1$.

3.1.4   Equality Constraints

Meeting the power requirement on the DC bus between the inverter and the storage system over the course of the drive cycle is the main equality constraint. Mathematical models of the powertrain components presented in Chapter 2 are used for formulating the constraints. A very important fact about the mathematical models of the battery and ultracapacitor cells is existence of the differential equations presented in (2.1) and (2.2). To deal with these differential equations in the optimization platform, a practical method is to discretize the power demand using a specific sampling time T_s and convert all continuous differential equations to their equivalent discrete forms. Choosing smaller values of T_s leads to more accurate optimization results. Using (2.1), the mathematical model of battery cells is

represented in discrete domain by:

$$i_{b,n} = -Q_b \left(\frac{S_{(n+1)} - S_n}{T_s} \right)$$

$$v_{bt,n} = v_{oc,n} - v_{bst,n} - v_{blt,n} - R_{bes,n} i_{b,n}$$

$$C_{bst,n} \left(\frac{v_{bst,(n+1)} - v_{bst,n}}{T_s} \right) = i_{b,n} - \frac{v_{bst,n}}{R_{bst,n}}$$

$$C_{blt,n} \left(\frac{v_{blt,(n+1)} - v_{blt,n}}{T_s} \right) = i_{b,n} - \frac{v_{blt,n}}{R_{blt,n}} \tag{3.6}$$

where subscript n denotes the values of the variables at $t = nT_s$. In a similar way, using (2.2), (3.7) formulates the mathematical model of ultracapacitor cells in discrete domain as:

$$v_{ut,n} = v_{u1,n} - R_{ues,n} i_{u,n}$$

$$\left(C_0 + C_{1,n} \right) \frac{v_{u1,(n+1)} - v_{u1,n}}{T_s} = -i_{u,n} \tag{3.7}$$

where

$$C_{1,n} = k_1 v_{u1,n} \tag{3.8}$$

Using the discretized equations in (3.6) and (3.7), for the battery-only and the ultracapacitor-only configurations, power balance between the storage system and the demand on the DC bus at $t = nT_s$, where n represents any arbitrary sampled interval, is formulated as:

$$N_{xs} N_{xp} v_{xt,n} i_{x,n} = \left(\frac{\alpha_n}{\eta_{m,n}} + (1 - \alpha_n) \eta_{r,n} \right) P_{d,n} \tag{3.9}$$

49

where

$$\eta_{m,n} = \eta_{i,m,n}\eta_{e,m,n}\eta_{g,m,n} \qquad \eta_{r,n} = \eta_{i,r,n}\eta_{e,r,n}\eta_{g,r,n} \qquad (3.10)$$

In (3.9), x denotes the storage devices that are directly connected to the DC bus ($x = b$ for battery and $x = u$ for ultracapacitor) and α_n assumes values of 1 or 0 for motoring or regenerative braking mode of operation, respectively, with $\eta_{m,n}$ and $\eta_{r,n}$ being the corresponding efficiencies of the drivetrain. In (3.10), $\eta_{i,m,n}$, $\eta_{e,m,n}$ and $\eta_{g,m,n}$ are efficiencies of the inverter, electric motor, and gearbox, respectively, during motoring operation. Similarly, $\eta_{i,r,n}$, $\eta_{e,r,n}$ and $\eta_{g,r,n}$ are the efficiencies of inverter, electric motor and gearbox, respectively, during regenerative braking. For the battery-ultracapacitor HESS configuration (partially-decoupled configuration, topology I, Fig. 2.7), the power balance on the DC bus is formulated as:

$$P_{BU,n}\left(\beta_n\eta_{sup,n} + \frac{1 - \beta_n}{\eta_{sdn,n}}\right) + P_{UC,n} = \left(\frac{\alpha_n}{\eta_{m,n}} + (1 - \alpha_n)\eta_{r,n}\right)P_{d,n} \qquad (3.11)$$

where β_n assumes values of 1 or 0 for step-up or step-down operation mode of the DC-DC converter, respectively, $\eta_{sup,n}$ and $\eta_{sdn,n}$ are the respective efficiencies of the DC-DC converter in step-up and step-down modes of operation, and

$$P_{BU,n} = N_{bs}N_{bp}v_{bt,n}i_{b,n} \qquad P_{UC,n} = N_{us}N_{up}v_{ut,n}i_{u,n} \qquad (3.12)$$

To split the power demand on the DC bus between BU and UC, the following rules are implemented:

- If the value of power demand on the DC bus is positive (discharging the storage system), the power component of the battery unit ($P_{BU,n}$) is determined using the

equality constraint given by (3.13).

$$P_{BU,n} = \frac{min\left(P_{con}, \dfrac{P_{d,n}}{\eta_{m,n}}\right)}{\eta_{sup,n}} \tag{3.13}$$

- For negative value of the power demand on the DC bus (charging the storage system), the equality constraint given by (3.14) determines $P_{UC,n}$.

$$P_{UC,n} = \eta_{r,n}P_{d,n} \tag{3.14}$$

3.1.5 Inequality Constraints

The inequality constraints are formulated by the limits defined for SoC and power of the battery cells, charge/discharge current of the battery and/or ultracapacitor cells, and terminal voltage and power of the ultracapacitor cells as:

$$SoC_{min} \leq SoC_n \leq SoC_{max}$$

$$P_{b,n,min} \leq v_{bt,n}i_{b,n} \leq P_{b,n,max}$$

$$I_{b,min} \leq i_{b,n} \leq I_{b,max}$$

$$V_{ut,min} \leq v_{ut,n} \leq V_{ut,max}$$

$$I_{u,min} \leq i_{u,n} \leq I_{u,max}$$

$$P_{u,n,min} \leq v_{ut,n}i_{u,n} \leq P_{u,n,max} \tag{3.15}$$

where SoC_{min}, $I_{b,min}$, $V_{ut,min}$, and $I_{u,min}$ are the minimum values of SoC, and current of the battery cells, and terminal voltage and current of the ultracapacitor cells, respectively. Similarly, SoC_{max}, $I_{b,max}$, $V_{ut,max}$, and $I_{u,max}$ are the maximum values of the above-mentioned variables, respectively. In (3.15), $P_{b,n,min}$, $P_{b,n,max}$, $P_{u,n,min}$, and $P_{u,n,max}$ are the minimum and maximum values of the powers of battery and ultracapacitor cells, respectively, at the sampled interval corresponding to $t = nT_s$. In the case of battery-ultracapacitor HESS configuration, the following set of equations are added to the constraints:

$$d_{min} \leq d_{sup,n} \leq d_{max} \qquad\qquad d_{min} \leq d_{sdn,n} \leq d_{max}$$

$$N_{bs}N_{bp}|v_{bt,n}i_{b,n}| \leq \left(\frac{\beta_n}{\eta_{sup,n}} + (1 - \beta_n)\eta_{sdn,n} \right) P_{con} \qquad (3.16)$$

where d_{min} and d_{max} are minimum and maximum values of the duty ratios of the switches of DC-DC converter ($d_{sup,n}$ for boost switch and $d_{sdn,n}$ for buck switch) which are determined by (3.17) for step-up and step-down operation modes of the DC-DC converter.

$$\frac{N_{us}v_{ut,n}}{N_{bs}v_{bt,n}} = f_{sup}(d_{sup,n}) \qquad\qquad \frac{N_{bs}v_{bt,n}}{N_{us}v_{ut,n}} = f_{sdn}(d_{sdn,n}) \qquad (3.17)$$

In (3.17), f_{sup} and f_{sdn} are the voltage conversion ratios between the high- and low-voltage sides of the DC-DC converter for step-up and step-down operation modes, respectively. Beside the constraints given by (3.15) and (3.16), additional constraints are considered for the numbers of series-connected battery cells (in the battery-only configuration) by (3.18) and series-connected ultracapacitor cells (in the ultracapacitor-only and battery-ultracapacitor HESS configurations) by (3.19):

$$V_{DC,min} \leq N_{bs}v_{oc,1} \leq V_{DC,max} \qquad (3.18)$$

$$V_{DC,min} \leq N_{us}v_{u1,1} \leq V_{DC,max} \qquad (3.19)$$

where $V_{DC,min}$ and $V_{DC,max}$ are the minimum and maximum values of the DC bus voltage, respectively, defined based on the open-circuit terminal voltage of the storage unit directly connected to the DC bus at full-charge status of the storage cells installed in the structure of the corresponding unit. It should be noted that if at any sampled interval, current of battery/ultracapacitor cells results in violation of any of the constraints given by (3.15) and (3.16), then, the corresponding current is set to be equal to the border value that respects the previously-violated constraint(s). Once the updated value of the current is determined, the following rules are implemented:

- When the updated value corresponds to the battery current ($i_{b,n}$ is equal to the corresponding border value), the new value of $i_{b,n}$, (3.11), and (3.12) are used to determine $v_{bt,n}$, $v_{ut,n}$, and $i_{u,n}$. If the new values of $v_{bt,n}$, $i_{b,n}$, $v_{ut,n}$, and $i_{u,n}$ respect all of constraints given by (3.15) and (3.16), the next sampled interval of the drive cycle is checked for respecting all equality and inequality constraints of the problem at the corresponding sampled interval. If not, the selected point (vector of optimization variables) is considered as an infeasible solution.

- When the updated value corresponds to the ultracapacitor current ($i_{u,n}$ is equal to the corresponding border value), $v_{bt,n}$, $i_{b,n}$, and $v_{ut,n}$ are calculated based on the new value of $i_{u,n}$, (3.11), and (3.12). If the new values of $v_{bt,n}$, $i_{b,n}$, $v_{ut,n}$, and $i_{u,n}$ respect all of constraints given by (3.15) and (3.16), the next sampled interval of the drive cycle is checked for respecting all equality and inequality constraints of the problem at the corresponding sampled interval. If not, the selected point (vector of optimization variables) is considered as an infeasible solution.

It should be noted that the rules implemented in Sections 3.1.4 and 3.1.5 indicate that in motoring mode, priority is given to the battery unit for providing the required power on the

53

DC bus taking the limits defined by (3.15) and (3.16) into account. On the other hand, in regenerative braking mode, the priority is given to the ultracapacitor unit to absorb the regenerated power on the DC bus while respecting the constraints given in (3.15) and (3.16).

3.2 Optimization Algorithm

There are several factors which affect the choice of a specific algorithm for solving an optimization problem. These include [82]:

- Nature of the objective function and constraints (linear or nonlinear, convex or non-convex)

- Number of optimization variables (small or large)

- Type of optimization variables (discrete or continuous)

- Smoothness of the objective function and constraints (differentiable or nondifferentiable).

When the objective function and constraints are convex and differentiable, the number of optimization variables is small, and the objective function does not have considerable number of optima, conventional derivative-based (gradient-based) algorithms such as Newton method can be applied to find the global optimum [82, 83]. Metaheuristic algorithms are significantly useful when the objective function and/or constraints have nonlinearity and the numbers of constraints and/or optimization variables are considerably large. Specially, in integer/mixed integer programming, metaheuristic methods become very popular

as the conventional gradient-based techniques cannot be applied in most of the cases. In computer science, a metaheuristic algorithm is a computational method that solves an optimization problem by iteratively trying to improve a candidate solution with regard to specific objectives [83, 84]. There are two categories for metaheuristic algorithms:

- Population-based algorithms: In population-based metaheuristic algorithms, an initial population is generated randomly and the optimization proceeds for different members of the population in a stochastic fashion. Genetic Algorithm (GA) and Particle Swarm Optimization (PSO) are two well-known examples of this category.

- Trajectory-based algorithms: In trajectory-based methods, such as Simulated Annealing (SA), a single agent moves through the search space in a piecewise style. It is assumed that every trajectory in the search space has a non-zero probability to reach the global optimum [85].

The problem of optimal sizing of battery-only and ultracapacitor-only storage systems in electric vehicle applications is an integer nonlinear programming (INLP) problem (in the case of a battery-ultracapacitor HESS configuration, it is a mixed-integer nonlinear programming (MINLP) problem) with quite a large number of constraints, considering the discretized equations of the system at every sampled interval. Due to nonlinearity of the problem, existence of integer values in the domain of solutions (the numbers of parallel branches of the storage devices and series-connected cells in each branch), and excessive number of constraints, a population-based metaheuristic optimization algorithm is used for solving the problem of optimal sizing of the storage systems. This algorithm is Teaching-Learning-Based Optimization (TLBO).

Teaching-Learning-Based Optimization (TLBO) algorithm is a metaheuristic optimization method which is based on interactions between a teacher and the students in a class,

and among the students, to increase the average grade of the class. Compared to other nature-based methods such as Genetic Algorithm (GA) and Ant Colony Optimization (ACO), TLBO benefits from lower computational effort. In addition, this method does not require specific controlling parameters such as mutation and cross-over coefficients in GA, which can affect the results of optimization [86]-[88]. The TLBO algorithm has two phases: teacher phase and learner phase.

3.2.1 Teacher Phase

In teacher phase, the learners try to improve their grades through what they learn from a high-quality teacher in the class. In this phase, the best grade in the class mimics the teacher and the objective is to raise the other marks to get as close as possible to the best one. Like any other population-based optimization method, TLBO algorithm starts with an initial randomly-chosen group of solutions (learners in the class). As there are several students in the class, their levels of knowledge are not the same. A good index representing the general knowledge of the learners is the mean value of the grades. In teacher phase, the teacher tries to improve the mean value of grades in the class. If at iteration k, the best member of population is defined as $X_{k,teacher}$, the mean value of all members as $M_{pop,k}$, and the jth particle as $X_{k,j}$, then, the temporarily-updated value of $X_{k,j}$ is defined as:

$$X_{k,j-new} = X_{k,j} + r_{k,1j} \left(X_{k,teacher} - (1 + r_{k,2j}) M_{pop,k} \right) \tag{3.20}$$

In (3.20), $r_{k,1j}$ and $r_{k,2j}$ are random numbers between 0 and 1. Once a member is temporarily updated using (3.20), it is compared to its former value to check if the new point results in a better position. If this occurs, then, the new position $(X_{k,j-new})$ replaces the previous position $(X_{k,j})$ of the jth particle at iteration k. This process is repeated for every member of the population.

It should be noted that in constrained optimization problems, choosing the best solution among a group of points is not just fulfilled by comparing their corresponding values of the objective function as done in unconstrained optimization problems. In the case of constrained optimization problems, beside the objective function, the equality and inequality constraints must be taken into account as well. In this thesis, a tournament-based procedure is used for choosing the best solution among two or more individuals of the population using the following rules (for a minimization problem) [89]:

- When comparing two feasible solutions, whichever has a lower value for the objective function is chosen as the better particle. A feasible solution is the one for which the equality and inequality constraints are not violated.

- When comparing one feasible solution with one infeasible solution, the feasible one is chosen as the better particle. An infeasible solution is the one for which at least one of the constraints is violated.

- When comparing two infeasible solutions, the one with a lower degree of violation is chosen as the better particle. For the minimization problem formulated by (3.1), for an infeasible solution, X_{inf}, the degree of violation is defined as:

$$\text{Degree of violation} = \sum_{i=1}^{N_e} \Big(H_{e,i}(X_{inf}, \zeta)\Big)^2 + \sum_{j=1}^{N_{ine}} \Big(max\{0, H_{ine,j}(X_{inf}, \zeta)\}\Big)^2 \quad (3.21)$$

3.2.2   Learner Phase

In learner phase, the participants in the class interact randomly with one another to increase the public knowledge of the class. To show this mathematically, let's assume the jth learner is going to raise its grade at iteration k by sharing knowledge with two other

randomly-chosen members $X_{k,m}$ and $X_{k,w}$, where $m \neq w \neq j$. The temporary update for $X_{k,j}$ is formulated as follows:

$$X_{k,j-new} = X_{k,j} + r_{k,3j} \left(X_{k,m} - X_{k,w} \right) \quad \text{if } X_{k,m} \text{ is better than } X_{k,w}$$

$$X_{k,j-new} = X_{k,j} + r_{k,3j} \left(X_{k,w} - X_{k,m} \right) \quad \text{if } X_{k,w} \text{ is better than } X_{k,m} \tag{3.22}$$

In (3.22), $r_{k,3j}$ is a random number between 0 and 1. After evaluating $X_{k,j-new}$, it is compared to $X_{k,j}$ to check whether the new position is better than the previous one or not. In every phase of optimization, after any modification to the positions of the members, the new positions are monitored to be within the specified limits associated with every particle in the group. Figure 3.1 shows the flowchart of the TLBO algorithm. As shown in this flowchart, the algorithm stops once the termination criteria are satisfied. The final solution will be the best solution among the final updated population. It should be noted that during solving the optimization problem, $r_{k,1j}$, $r_{k,2j}$, and $r_{k,3j}$ in (3.20) and (3.22) are generated using the *rand* function in MATLAB.

To save time and search space required for monitoring every individual variable in a multidimensional optimization problem, in this thesis, the positions of particles in TLBO algorithm are modeled with angles. Using this technique, the lower and upper limits of the new optimization variables will be $-\pi/2$ and $\pi/2$, respectively [87]. To formulate this process, let's consider the optimization problem to be q-dimensional, i.e., $X = [x_1, x_2, \ldots, x_q]$. Then, in TLBO algorithm, a variable x_s $(s = 1, 2, 3, \ldots, q)$ is modeled by an angle ξ_s using the following formula:

$$x_s = \frac{x_{s-max} - x_{s-min}}{2} \sin(\xi_s) + \frac{x_{s-max} + x_{s-min}}{2} \tag{3.23}$$

where x_{s-max} and x_{s-min} are the maximum and minimum values of the variable x_s, respectively.

3.3 Summary

This chapter provided formulation of the optimal sizing problem. The objective functions, set of inputs, optimization variables, and equality and inequality constraints were defined. In addition, the optimization algorithm required to solve the problem of optimal sizing was formulated and discussed.

Start optimization with initial population with q members

Teacher phase

Determine the mean value among members of population (M_{pop})

Determine the best solution ($X_{teacher}$)

$j=1$

Modify the solutions using
$$X_{j-new} = X_j + r_{1j}\left(X_{teacher} - \left(1 + r_{2j}\right)M_{pop}\right)$$

Is new position better than the existing one?

No — Yes

Replace X_j with X_{j-new}.

$j=j+1$

Is $j \leq q$? — Yes

No

Learner phase

Select any two random members X_m and X_w where $m \neq w \neq j$

Is X_m better than X_w?

No — Yes

Modify the solutions using
$$X_{j-new} = X_j + r_{3j}\left(X_w - X_m\right)$$

Modify the solutions using
$$X_{j-new} = X_j + r_{3j}\left(X_m - X_w\right)$$

Is new position better than the existing one?

No — Yes

Replace X_j with X_{j-new}.

$j=j+1$

Is $j \leq q$? — Yes

No

Are termination criteria met?

No — Yes

Determine the best solution as the optimum point

60

Figure 3.1: Flowchart of the TLBO algorithm

Chapter 4

Optimization Results

In this chapter, the problem of optimal sizing of the storage system is solved for two different classes of electric vehicles: (i) a small-size, long-range car and (ii) a city bus. For the first case, parameters of Tesla Roadster (mass excluding the storage unit and dimensions) are used. For this vehicle, the problem of optimal sizing is solved for the battery-only configuration shown in Fig. 2.1. In the second case, a city bus is considered for the purpose of optimization and simulation. The three configurations shown in Figs. 2.1, 2.2, and 2.3 are studied when solving the problem of optimal sizing for the city bus. For each of these vehicles, the storage system is optimally sized based on specific assumptions in terms of vehicle parameters and driving conditions. It should be noted that as explained in Chapter 2, the ultracapacitor-only powertrain cannot be technically used for the small-size, long-range car. Besides, the reason behind not using the battery-ultracapacitor HESS powertrain for the purpose of optimal sizing of the storage system for the small-size, long-range car is due to lower level of specific energy and higher price of the ultracapacitor cells compared to those of battery cells. Although, this powertrain is feasible to be implemented for the

small-size, long-range vehicle from energy and power viewpoints, the cost of the resulting system is much higher than that of the battery-only configuration. In other words, even though both of battery-only and battery-ultracapacitor HESS configurations can complete the required drive cycle, the storage system is much cheaper for the former case. These issues can be resolved if the ultracapacitor unit has the option of being frequently charged over the course of the drive cycle. That is why both of ultracapacitor-only and battery-ultracapacitor HESS powertrains are considered for the purpose of optimal sizing of the storage system in the case of electric city bus.

For optimal sizing of the storage systems which include battery units, Panasonic 18650 battery cells are used. These battery cells have Lithium-Iron Phosphate ($LiFePO_4$) chemistry, with the data given in Table 4.1 [90]. For the electrical model of the battery cells shown in Fig. 2.14, (4.1) gives the open-circuit voltage, resistances, and capacitances as functions of SoC of the battery cells (S) at $t = nT_s$ [91]. It should be noted that in this thesis, the battery cell capacity is assumed to be constant.

$$V_{oc,n} = -1.031e^{-35S_n} + 3.685 + 0.2156S_n - 0.1178S_n^2 + 0.3201S_n^3$$

$$R_{bes,n} = 0.1562e^{-24.37S_n} + 0.07446$$

$$R_{bst,n} = 0.3208e^{-29.14S_n} + 0.04669$$

$$R_{blt,n} = 6.603e^{-155.2S_n} + 0.04984$$

$$C_{bst,n} = -752.9e^{-13.51S_n} + 703.6$$

$$C_{blt,n} = -6056e^{-27.12S_n} + 4475 \tag{4.1}$$

When an ultracapacitor unit is used in the storage system, Maxwell BoostCAP3000 cells with the data given in Table 4.2, are used [92]. For the electrical model of the ultracapacitor

Table 4.1: Data of Panasonic 18650 battery cell [90]

Parameter	Value
Mass (g)	43
Rated capacity (Ah)	2.25
Nominal voltage (V)	3.7
Max discharge current (A)	11.25 (5C)
Max charge current (A)	2.25 (1C)

Table 4.2: Data of Maxwell BoostCAP3000 ultracapacitor cell [92]

Parameter	Value
Mass (g)	510
Rated capacity (F)	3000
Nominal voltage (V)	2.7
Max discharge current (A)	1900
Max charge current (A)	1900

cells shown in Fig. 2.15, $R_{ues} = 0.29 \ m \ \Omega$, $C_0 = 521.441 \ F$, and $k_1 = 917.985 \ F/V$ [92, 93]. For solving the problem of optimal sizing, two approaches are considered for modeling the efficiencies of the DC-AC converter and the traction motor.

1. **Approach I:** In this approach, efficiencies of the DC-AC converter and the traction motor are functions of the output powers of the DC-AC converter and the traction motor per-unitized using the maximum ratings of these devices as the base. Tables 4.3 and 4.4 show the efficiencies of the DC-AC converter at specific loads (in per-unit)

63

for inversion and rectification modes, respectively. The efficiencies of the traction motor at specific loads (in per-unit) for motoring and regenerative braking modes are shown in Tables 4.5 and 4.6, respectively.

2. **Approach II:** In this approach, the detailed models of the DC-AC converter and the traction motor discussed in Chapter 2 are used for the purpose of optimization

Table 4.3: Efficiency of the DC-AC converter at specific loads for inversion mode

Load (pu %)	0	1.5	20	40	60	80	100
Efficiency (%)	0	59.80	81.09	88.11	91.33	93.15	94.40

Table 4.4: Efficiency of the DC-AC converter at specific loads for rectification mode

Load (pu %)	0	1.5	20	40	60	80	100
Efficiency (%)	0	55.02	78.73	87.39	91.08	93.08	94.33

Table 4.5: Efficiency of the electric machine at specific loads for motoring mode

Load (pu %)	0	1.5	20	40	60	80	100
Efficiency (%)	0	47.59	73.64	81.42	84.61	86.30	87.40

Table 4.6: Efficiency of the electric machine at specific loads for regenerative braking mode

Load (pu %)	0	1.5	20	40	60	80	100
Efficiency (%)	0	44.01	70.75	80.67	84.36	86.25	87.40

and simulation. For the DC-AC converter, 400 V, 150 A IGBT switches with the parameters given by (4.2) are used. In this thesis, for calculating the switching loss of the DC-AC converter using (2.12), $k_{sw} = 0.25$ is considered. In addition, it is assumed that the switching frequency of the DC-AC converter is 21 times the fundamental frequency of the stator current (this is to reduce harmonic distortion of the AC-side voltage of the inverter).

$$R_{sw} = 0.0132 \ \Omega \qquad R_D = 0.016 \ \Omega \qquad V_{sw} = 1.25 \ V \qquad V_D = 0.7 \ V$$

$$t_{on} = 0.09 \ \mu s \qquad t_{off} = 0.15 \ \mu s \tag{4.2}$$

When solving the optimization problem, at each iteration of the optimization, depending on the number of series-connected cells of the ESS devices which are connected directly to the DC bus and the power rating of the traction motor, the number of IGBT switches connected in series-parallel arrangement (to meet the voltage and current requirements of the DC-AC converter) are determined. This way, the equivalent parameters of the IGBT switches would be selected corresponding to the solutions of the optimization problem. It should be noted that in addition to the converter losses calculated using (2.14), in this thesis, 5% of the load power in both inversion and rectification modes of operation is considered for the losses due to harmonic components and other factors not modelled mathematically in Section 2.4.

4.1 Optimal Sizing of the Battery Unit for a Small-size, Long-range Electric Vehicle

This section presents the results of solving the problem of optimal sizing for a small-size, long-range EV based on specifications of Tesla Roadster. Tesla Roadster is the first electric

sport car on the road which has used lithium-ion batteries as the storage device [94]. It should be noted that although the parameters of Tesla Roadster, i.e., mass (excluding the storage unit) and dimensions, are used as the inputs for solving the optimization problem, parameters of any other passenger vehicle, such as Nissan Leaf, could have been chosen for the purpose of optimization and simulation. The main objective in this section is to address solving the problem of optimal sizing for a small-size vehicle which is capable of fulfilling a long range (for instance, beyond 200 km) on a given drive cycle with a single charge of the battery unit. In Section 4.1.1, the results of optimization based on specific assumptions for solving the problem, are presented. Beside the optimization results, the section provides simulation results for speed-versus-time of the vehicle (used for determining the duration of $0 - 60$ $mile/h$ ($0 - 96.6$ km/h) acceleration and top speed of the car) and torque-versus-rpm of the electric motor during full acceleration. It is worth mentioning that even though it is shown how the limits defined by (3.18) can affect the duration of $0 - 60$ $mile/h$ acceleration, this duration is not considered as a constraint when solving the optimization problem. Section 4.1.2 studies the performance indexes of the vehicle such as duration of $0 - 60$ $mile/h$ acceleration and top speed under different conditions, and range based on constant-speed operation and driving on well-known drive cycles.

Table 4.7 provides the parameters required for calculating power demand. When solving the optimization problem, the following assumptions are made [94]-[96]:

Table 4.7: Parameters used to calculate power demand

A_f (m^2)	v_w (m/s)	ρ_a (kg/m^3)	C_d	g (m/s^2)	Pr (psi)	r_{wh} (m)	N_g
2.086	3.5	1.202	0.35	9.81	36	0.31	8.2752

- EPA Federal Test Procedure (FTP75) is used as the speed-versus-time profile based on which the drive cycle required for solving the optimization problem is constructed. FTP75 is a 17.76 km drive cycle $(1,874\ s$ long), with the average speed of 34.11 km/h, maximum speed of 91.23 km/h, and several acceleration and deceleration events. Figure 4.1 shows the speed-versus-time profile of this drive cycle. It is assumed that the vehicle is expected to travel 355.3 km on this drive cycle (20 repetition of FTP75) with a single charge of the battery unit.

- All prices are expressed in US dollars.

- The total power loss of the traction motor due to core, friction, windage, and stray components, is fixed and equal to 10% of the load power in both motoring and regenerative braking modes.

- Mass of the vehicle without the battery unit is considered to be equal to 940 kg. An additional mass of 80 kg is considered for the driver. At every iteration of the
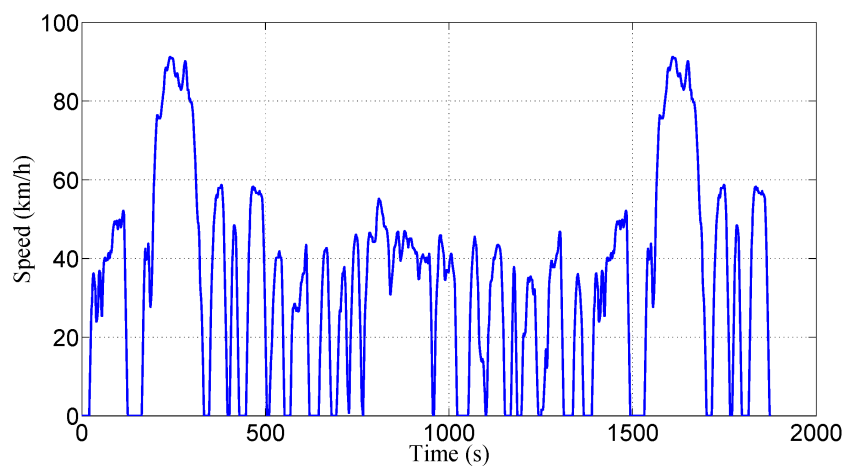
Figure 4.1: Speed-versus-time characteristic of FTP75 drive cycle

optimization process, for each member of population, this $1,020\ kg$ mass is summed up with the mass of the battery unit corresponding to the chosen energy storage system size to determine the total mass of the vehicle required for calculating the power demand from speed-versus-time characteristic of the drive cycle.

- Battery cells are fully charged at the beginning of drive cycle.

- SoC of battery cells is allowed to vary between 2% and 100% over the drive cycle.

- The maximum and minimum numbers of series-connected cells on the DC bus are determined based on the upper and lower limits of $430\ V$ and $300\ V$ for the DC bus open-circuit voltage.

- The transmission system has a fixed efficiency of 96% with a gearbox of fixed gear ratio of $8.2752:1$.

- Temperature is constant at $25^o\ C$.

In this thesis, an analytical procedure based on targeted performance (Fig. 4.2) is used to determine the approximate values for the parameters of the traction motor (required for approach II) which are:

$$L_m = 1,438.01\ \mu H \qquad L_{\ell s} = 38.77\ \mu H \qquad L_{\ell r} = 38.77\ \mu H$$

$$R_s = 7.43\ m\Omega \qquad R_r = 4.73\ m\Omega \qquad \omega_{sy,base} = 667\ rad/s \tag{4.3}$$

Figure 4.2 shows the torque-speed characteristic curves of the traction motor calculated based on the parameters given in (4.3). The last curve shown in red corresponds to the maximum AC voltage on the terminals of the traction motor which is equivalent to maximum achievable AC voltage from series connection of 99 battery cells on the DC bus when

68
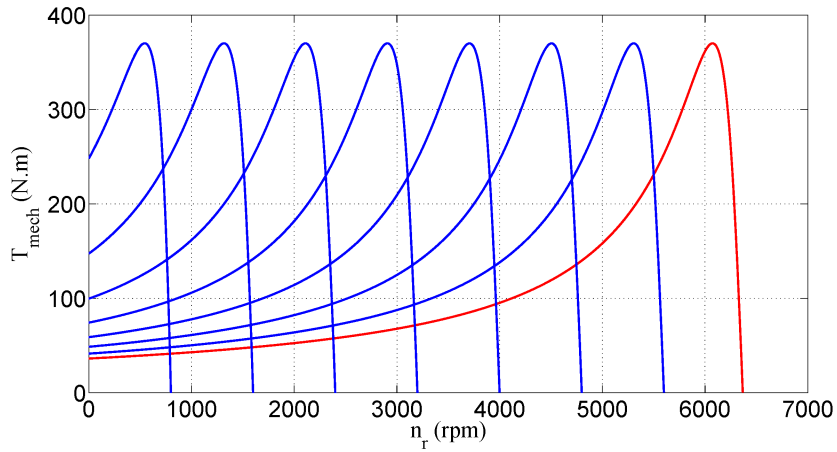
Figure 4.2: Torque-speed characteristic curves of the traction motor used for optimal sizing of the battery unit of the small-size, long-range EV

linear modulation is considered for the operation of DC-AC converter. It should be noted that in Tesla Roadster, 99 battery cells are connected in series to the DC bus. As seen in this figure, the traction motor can keep a constant torque of 370 $N.m$ up to around 6, 400 rpm. When solving the optimization problem, the no-load DC bus voltage is calculated based on the number of series connected cells corresponding to the position of each individual at every iteration. Using this voltage, the base frequency of the traction motor is calculated assuming that the ratio of the no-load voltage over the base frequency is fixed for different traction motors used in the optimization. Once the base frequency is known, the maximum torque of the corresponding machine is calculated using (2.27).

4.1.1 Optimization Results

Considering all constraints of the problem, the optimization results are shown in Table 4.8 based on approaches I and II. Figures 4.3 and 4.4 show SoC of the battery cells and

69

Table 4.8: Optimization results for the small-size, long-range EV

Approach	N_{bs}	N_{bp}	Number of battery cells $(N_{bs} \times N_{bp})$	cost of BU considering $ 2 as the price of battery cells ($)	cost of BU considering $ 7 as the price of battery cells ($)	Mass of BU (kg)
I	101	71	7,171	14,342	50,197	308.4
II	74	83	6,142	12,284	42,994	264.1

the DC bus voltage versus time, respectively, for the whole drive cycle (20 repetitions of FTP75), based on Approach II with $N_{bs} = 74$ and $N_{bp} = 83$. In Fig. 4.5, variations of the power of BU and the power demand on the DC bus versus time are depicted for the first FTP75 of the whole drive cycle. This figure shows an exact match between these two power components. This match represents respecting the equality constraint (Equation (3.9)) at each sampled interval of the drive cycle.

Figure 4.6 shows the speed-versus-time characteristics of the vehicle with $N_{bs} = 74$ and $N_{bp} = 83$ during full acceleration on a flat road at $v_w = 0$. With this size of BU, the vehicle can reach speed of 60 $mile/h$ in 6.06 s and achieve the top speed of 197.2 km/h. Considering full acceleration of the vehicle with the optimally-sized battery unit, maximum torque of the traction motor is calculated to be 276.6 $N.m$. Variation of torque with respect to rpm speed of the traction motor during full acceleration of the vehicle is shown in Fig. 4.7. As mentioned before, during full acceleration, the electric motor starts operating at its maximum torque (276.6 $N.m$) which is kept constant up to around $3,760$ rpm and then, it operates under constant-power and maximum-power conditions, respectively.
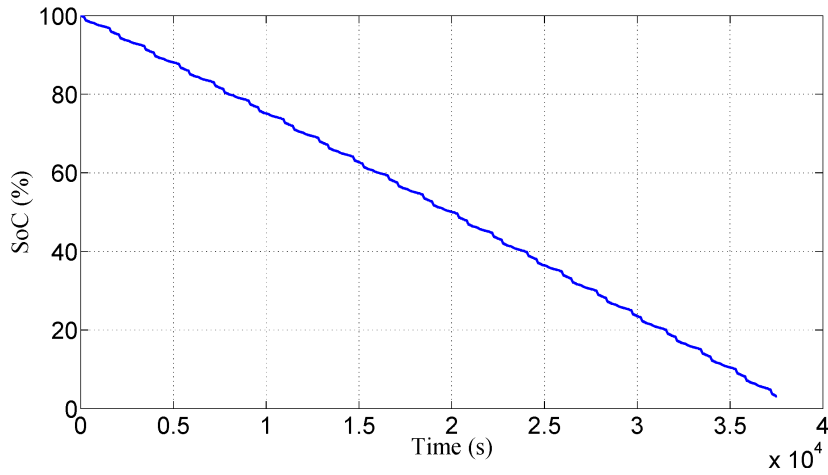
Figure 4.3: SoC of the battery cells versus time with $N_{bs} = 74$ and $N_{bp} = 83$
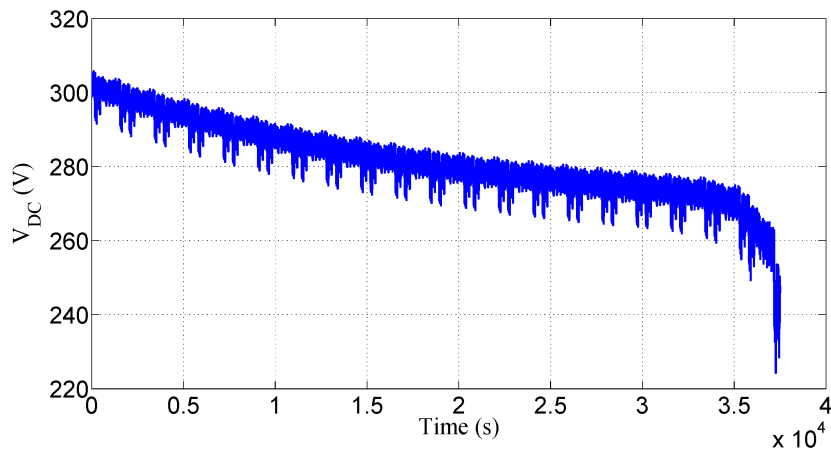
Figure 4.4: DC bus voltage versus time with $N_{bs} = 74$ and $N_{bp} = 83$

The maximum torque and the number of series-connected battery cells on the DC bus have direct impact on the duration of $0 - 60 \ mile/h$ acceleration of the vehicle. To shorten the duration of $0 - 60 \ mile/h$ acceleration, it is required to increase the number of series-connected cells on the DC bus and use a traction motor capable of exerting a larger torque.
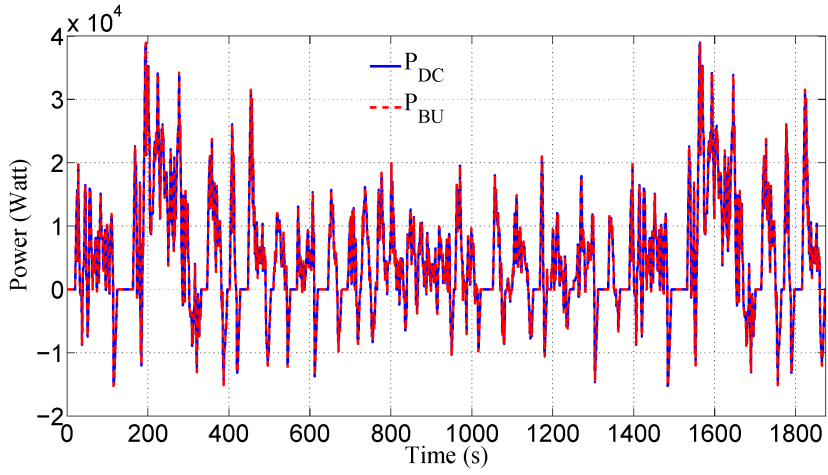
Figure 4.5: Power of battery unit and power demand on the DC bus versus time over one FTP75 cycle with $N_{bs} = 74$ and $N_{bp} = 83$
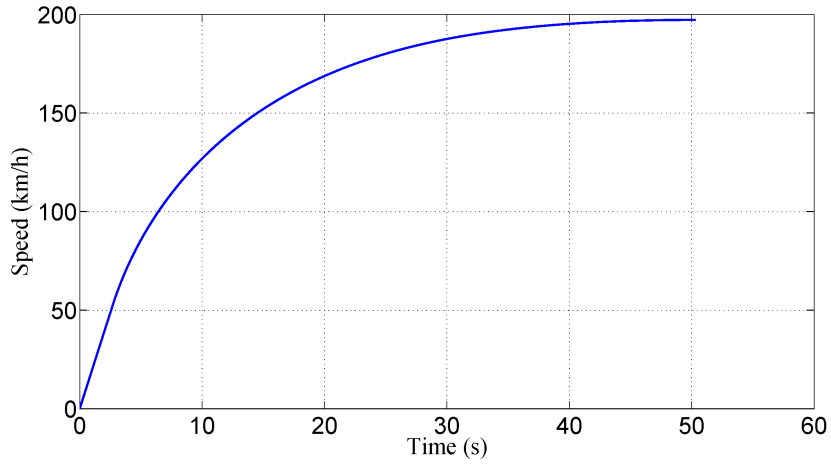
Figure 4.6: Speed versus time during full acceleration with $N_{bs} = 74$ and $N_{bp} = 83$

As an example, if we solve the optimization problem with the assumption that the open-circuit voltage limits of 470 V and 430 V are considered for determining the maximum and minimum numbers of series-connected cells on the DC bus, with other assumptions
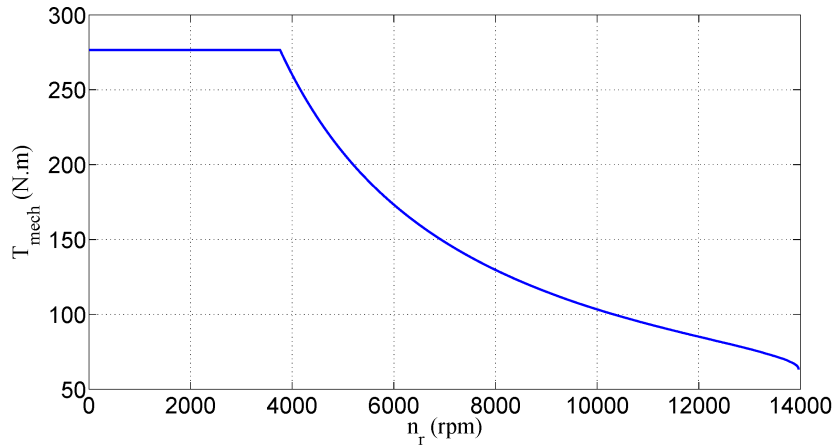
Figure 4.7: Torque versus rpm speed of the traction motor during full acceleration with $N_{bs} = 74$ and $N_{bp} = 83$

unchanged, the optimization results are $N_{bs} = 106$ and $N_{bp} = 60$. With this size of the battery unit, the no-load DC bus voltage at full charge status of the battery cells is 434.9 V which can exert a maximum torque of 396.2 $N.m$ on the motor shaft at full acceleration. With this torque, the vehicle can reach speed of 60 $mile/h$ in 3.95 s and attain top speed of 237.3 km/h. The variations of speed versus time and torque versus rpm speed of the traction motor in this case are shown in Figs. 4.8 and 4.9, respectively.

4.1.2   Analysis of the Performance Indexes

A very important fact about the performance indexes of an electric vehicle such as top speed and duration of $0 - 60$ $mile/h$ acceleration is that they are always valid for specific conditions. These conditions can include initial SoC and maximum discharge current of the battery cells, wind speed, and road grade. Tables 4.9 and 4.10 show variations of the above-mentioned performance indexes for the vehicle under study with $N_{bs} = 74$ and
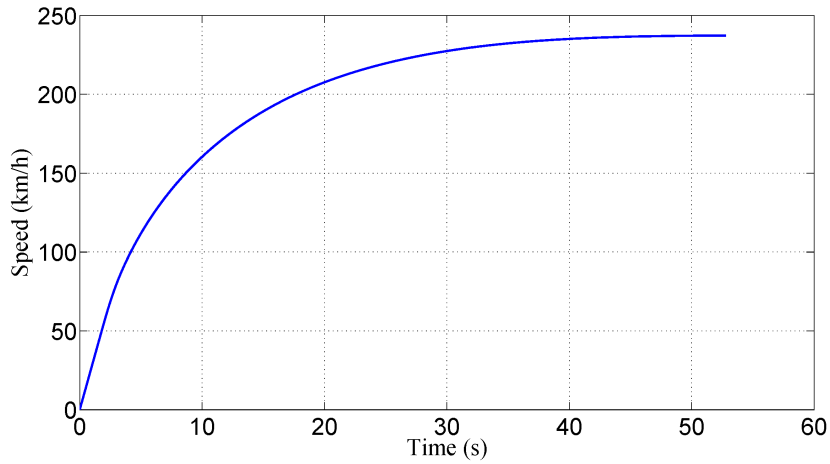
Figure 4.8: Speed versus time during a full acceleration with $N_{bs} = 106$ and $N_{bp} = 60$
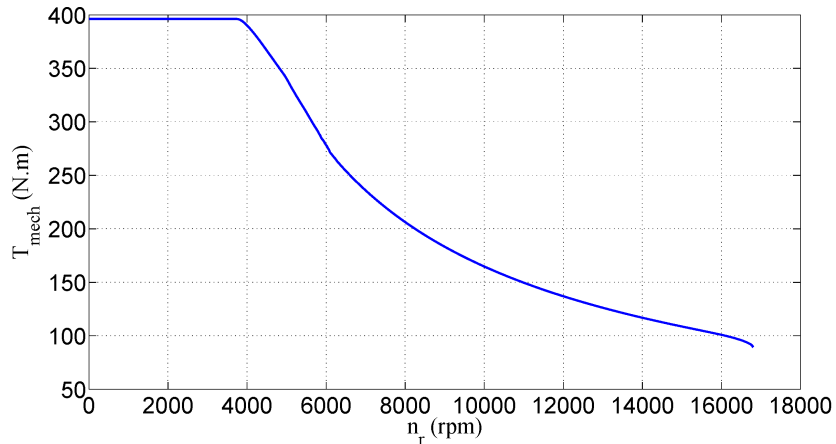
Figure 4.9: Torque versus rpm speed of the traction motor during a full acceleration with $N_{bs} = 106$ and $N_{bp} = 60$

$N_{bp} = 83$ based on different values of initial SoC and maximum discharge current ($I_{b,max}$) of the battery cells. As seen from these tables, the top speed achievable by the vehicle decreases with lowering the initial SoC and maximum discharge current of the cells. At lower values of initial SoC, the DC bus voltage is low and the battery unit cannot deliver

74

Table 4.9: Top speed and duration of $0-60\ mile/h$ acceleration with $N_{bs} = 74$ and $N_{bp} = 83$ on a flat road when $v_w = 3\ m/s$ and $I_{b,max} = 5\ C$

Initial SoC (%)	20	40	60	80	100
Top speed (km/h)	184.40	185.39	187.04	189.09	192.13
Duration of $0-60\ mile/h$ acceleration (s)	6.66	6.57	6.46	6.31	6.11

Table 4.10: Top speed and duration of $0-60\ mile/h$ acceleration with $N_{bs} = 74$ and $N_{bp} = 83$ on a flat road when $v_w = 3\ m/s$ and $I_{b,max} = 2\ C$

Initial SoC (%)	20	40	60	80	100
Top speed (km/h)	165.63	166.65	167.65	169.39	170.86
Duration of 0-60 $mile/h$ acceleration (s)	8.26	8.12	7.96	7.74	7.45

its maximum power capability. Therefore, the duration of constant torque becomes shorter and the constant power region starts at a lower power. Consequently, the duration of $0-60$ $mile/h$ acceleration becomes longer. This is also valid for the case when the maximum discharging current of the battery cells decreases which means that the power capability of the battery cells is lower. The decrease in the maximum power due to lower initial SoC and/or maximum discharging current of the battery cells has a direct impact on the top speed of the vehicle as shown by the results of Tables 4.9 and 4.10. In Tables 4.11 and 4.12, variations of the duration of $0-60\ mile/h$ acceleration and top speed with respect to initial level of SoC are given for different values of wind speed and grade of the road. At higher values of wind speed and road grade, the opposing force against the vehicle acceleration is larger resulting in lower top speed and longer duration of $0-60\ mile/h$ acceleration.

Table 4.11: Top speed and duration of $0-60\ mile/h$ acceleration with $N_{bs} = 74$ and $N_{bp} = 83$ on a flat road when $v_w = 11\ m/s$ and $I_{b,max} = 5\ C$

Initial SoC (%)	20	40	60	80	100
Top speed (km/h)	171.64	172.45	174.10	176.09	179.36
Duration of 0-60 $mile/h$ acceleration (s)	6.93	6.83	6.70	6.54	6.32

Table 4.12: Top speed and duration of $0-60\ mile/h$ acceleration with $N_{bs} = 74$ and $N_{bp} = 83$ on a road with the grade of 15 % when $v_w = 3\ m/s$ and $I_{b,max} = 5\ C$

Initial SoC (%)	20	40	60	80	100
Top speed (km/h)	120.55	122.30	124.29	127.42	131.74
Duration of 0-60 $mile/h$ acceleration (s)	11.80	11.40	10.98	10.41	9.73

Another important performance index normally reported by EV manufacturers is the range capability based on constant speeds. Figure 4.10 shows the range capability based on constant velocities of the vehicle under study in the range of $5-100\ km/h$ for four different values of wind speed. As seen in this figure, the curves of constant-speed range have maximum values corresponding to points in the range of $15-21\ km/h$ depending on the wind speed. The behavior of the curves in Fig. 4.10 can be better explained using the average battery-to-wheel efficiencies shown in Fig. 4.11. To calculate this efficiency at a constant velocity of the vehicle and a wind speed, with the optimally-sized battery unit onboard, powertrain of the vehicle is simulated for the total permissible range of SoC while respecting all constraints on the current and power of the battery cells. Then, the average battery-to-wheel efficiency is calculated as the mean value of the vector of

76
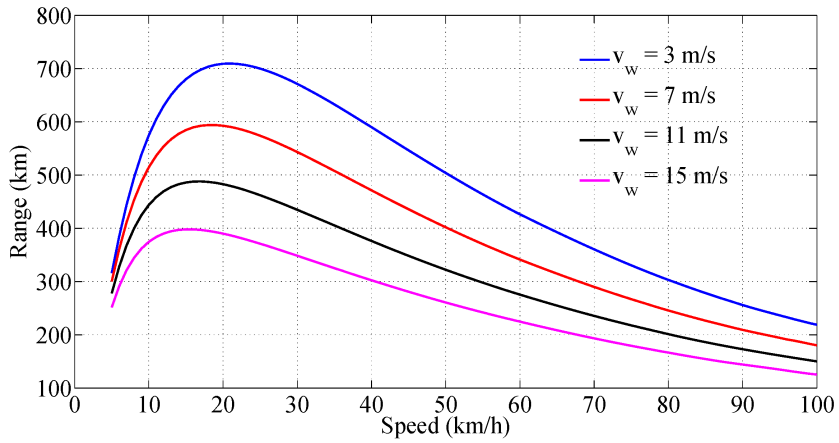
Figure 4.10: Range capability versus constant speed with $N_{bs} = 74$ and $N_{bp} = 83$ at four different wind speeds
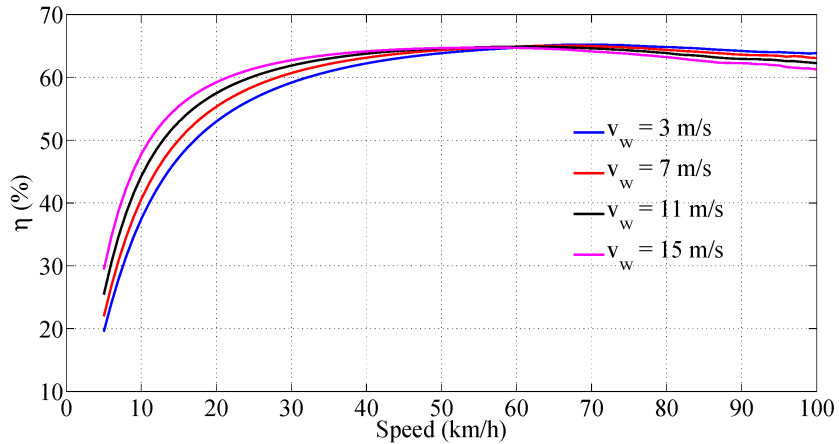
Figure 4.11: Average battery-to-wheel efficiency versus constant speed with $N_{bs} = 74$ and $N_{bp} = 83$ at four different wind speeds

powertrain efficiency whose elements are calculated at each sampled interval over the course of simulation. At very low values of constant speed, the battery-to-wheel efficiency is quite low due to low efficiencies of the inverter and the traction motor at light loads. Therefore,

most of the power of BU is lost, leading to short driving range capabilities. On the other hand, at high values of constant speed, the battery-to-wheel efficiency is quite high. This indicates that most of the power of the battery unit is transferred to the wheels during constant-speed driving. However, at high speeds, the power demand is also large, resulting in fast depletion of the storage unit. This means that the vehicle cannot travel very long as the battery cells are discharged completely over shorter intervals. As a result, there are always some points in-between where the constant-speed range capability becomes maximum.

Range capabilities of EVs can be analyzed based on travelling on well-known drive cycles. As an example, let's consider three drive cycles as: FTP75, Highway Fuel Economy Driving Schedule (HWFET), and New European Driving Cycle (NEDC). The time-speed characteristics of HWFET and NEDC are shown in Figs. 4.12 and 4.13, respectively. Different speed levels as well as acceleration and deceleration trends of these drive cycles result in different power demands when the vehicle undergoes each of these driving patterns.
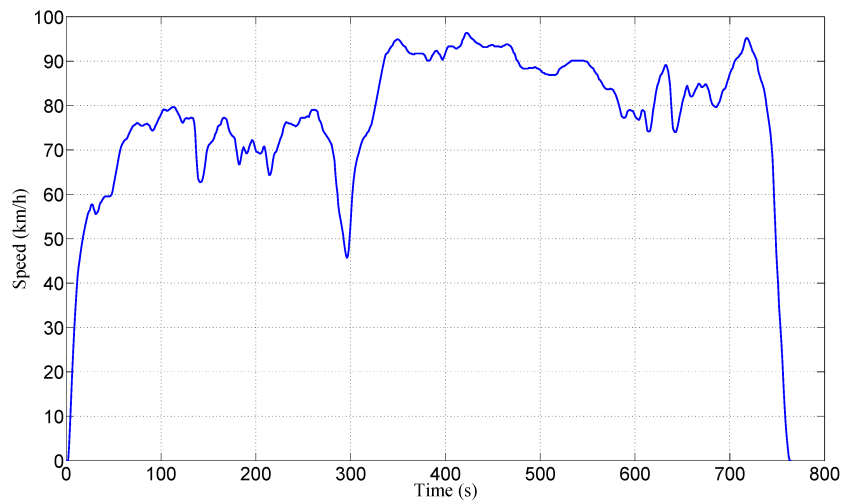
Figure 4.12: Speed-versus-time characteristic of HWFET drive cycle
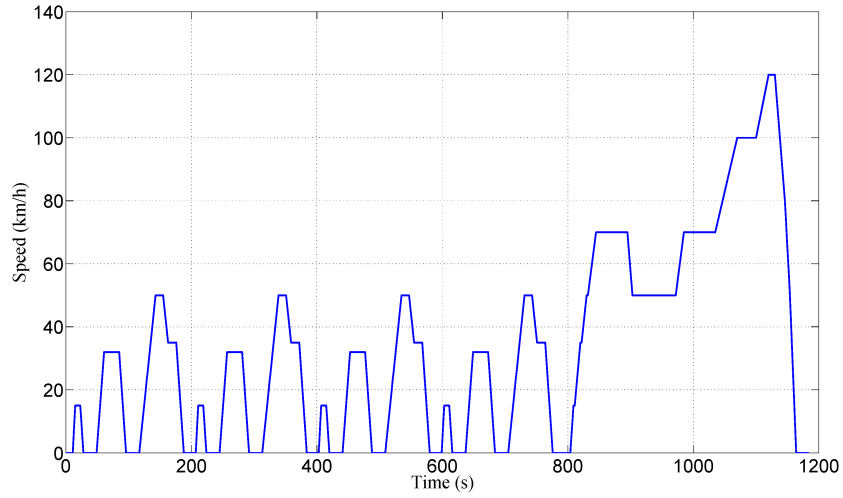
Figure 4.13: Speed-versus-time characteristic of NEDC drive cycle

Table 4.13: Comparison of range capabilities for different drive cycles

Drive cycle	FTP75	HWFET	NEDC
Top speed (km/h)	91.2	96.4	120
Maximum power of BU (W)	39,444.1	33,578.8	56,056.9
Average power of BU (W)	4,805.7	13,983.5	5,256.7
Range (km)	355.3	277.2	305.0

Table 4.13 compares the driving ranges of the vehicle under study on these drive cycles when the wind speed is equal to 3.5 m/s, the road is assumed to be flat, and full energy of the battery is allowed to be used over the drive cycles. As seen in the results of this table, the vehicle travels the longest range on the FTP75 drive cycle while it has the shortest range on HWFET. An indirect reason for these observations is very low and high average powers of the battery unit on the FTP75 and HWFET drive cycles, respectively.

This indicates that the battery unit is depleted much faster when the vehicle undergoes HWFET. It should be noted that the average power of battery unit for a specific drive cycle (FTP75, HWFET, or NEDC) in Table 4.13 is equal to the mean value of the vector of BU power whose elements are calculated based on the power demand at each sampled interval of the corresponding drive cycle.

An important advice from car manufacturers is not to over-charge or over-discharge the battery units. The cycle life of battery cells is reduced when deep charge and discharge cycles are experienced. Therefore, it is always recommended that SoC of the battery cells is maintained within specific limits. A typical recommended example is the SoC range of $30\% - 70\%$. Although limiting the range of SoC variation helps delay the aging process of the battery cells, it has the disadvantage of losing range capability due to narrower span of energy available to complete a drive cycle. Table 4.14 provides a comparison among the ranges on FTP75, HWFET, and NEDC drive cycles for different permissible ranges of SoC. As seen in this table, for the SoC range of $30\% - 70\%$, the completed range is significantly shorter than those obtained for the larger SoC ranges and full SoC range given in Table 4.13.

It should be noted that the auxiliary loads specially air conditioning power can have

Table 4.14: Comparison of range capabilities based on different permissible ranges of SoC of battery cells

Drive cycle	FTP75	HWFET	NEDC
Range based on SoC variation of $10\% - 90\%$ (km)	292.9	226.4	259.6
Range based on SoC variation of $20\% - 80\%$ (km)	218.5	170.2	194.3
Range based on SoC variation of $30\% - 70\%$ (km)	144.9	112.6	129.2

a significant effect on the performance of the vehicle [97]. The range that an EV can travel may vary significantly if driving is taking place in a mild whether condition or in a very hot day in the middle of summer. Table 4.15 compares the obtainable ranges of the vehicle under study on the selected drive cycles for different air conditioning powers in the range of $500 - 2,000\ W$. As seen in this table, depending on the air conditioning power and driving pattern of each drive cycle, the range can be different. For example, in the case of FTP75 drive cycle, the air conditioning power can significantly reduce the driving range of the vehicle. The reason is that the average power of BU on this drive cycle is quite low $(4,805.7\ W)$ and is comparable with the additional air conditioning power. For instance, when the air conditioning power is $2,000\ W$, the average load of the battery unit increases by 42% which is quite significant. Therefore, the reduction in the driving range is quite large (from $355.3\ km$ with no air-conditioning load, Table 4.13, to $252.4\ km$ with the air-conditioning load equal to $2,000\ W$). In the case of HWFET cycle, the original average load of the battery unit is $13,983.5\ W$. Even when the air conditioning load is $2,000\ W$, the average load of BU increases by 14%. Consequently, the effect on the driving range, when the vehicle is on the HWFET drive cycle, is not as large as that in the case of FTP75.

Table 4.15: Comparison of range capabilities based on different air conditioning power

Drive cycle	FTP75	HWFET	NEDC
Range based on air conditioning power of 500 W (km)	324.1	267.9	283.0
Range based on air conditioning power of 1,000 W (km)	297.3	258.0	261.1
Range based on air conditioning power of 1,500 W (km)	272.9	249.7	239.3
Range based on air conditioning power of 2,000 W (km)	252.4	241.4	217.6

4.2 Optimal Sizing of the Storage System of an Electric City Bus

In this section, the problem of optimal sizing of the storage system is solved for an electric city bus. The results of optimization are provided for the battery-only, ultracapacitor-only, and battery-ultracapacitor HESS configurations, in Sections 4.2.1, 4.2.2, and 4.2.3, respectively. When solving the optimization problem, the following assumptions are made [90, 92, 95, 98, 99]:

- Daily operation of the electric bus is equivalent to travelling 240 km on EPA Urban Dynamometer Driving Schedule (UDDS) (20 repetitions of the UDDS cycle). Figure 4.14 shows speed-versus-time profile of this drive cycle. UDDS is a 12 km city cycle (1,370 s long), with the average speed of 31.5 km/h and maximum speed of 91.2 km/h. In this thesis, the time difference between the starting points of two consecutive UDDS cycles is 45 minutes which includes 1370-second length of the cycle and the waiting period at the end-point terminals. This waiting period can be used for swapping the battery unit and/or charging the ultracapacitor unit.

- All prices are expressed in US dollars.

- Duty ratio of the DC-DC converter interfacing BU and UC is allowed to vary between 0.2 and 0.8.

- The total power loss of the traction motor due to core, friction, windage, and stray components, is fixed and equal to 10% of the load power in both motoring and regenerative braking modes.
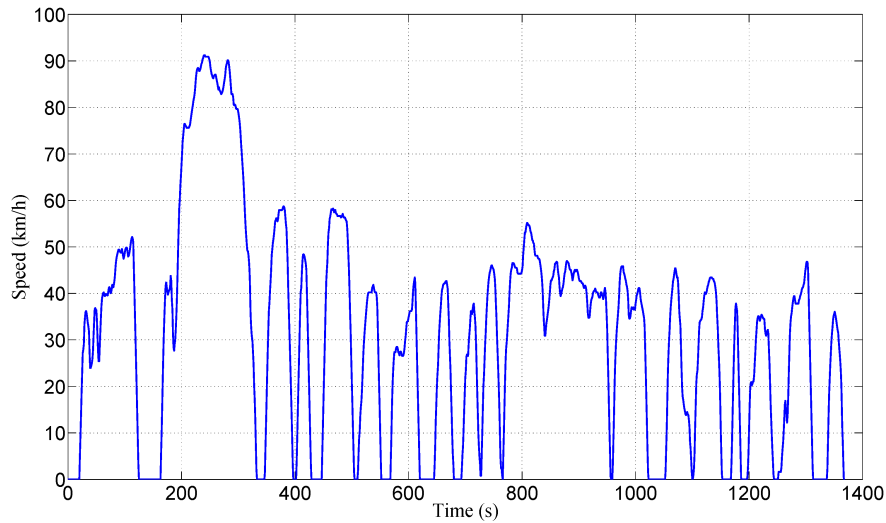
Figure 4.14: Speed-versus-time characteristic of UDDS drive cycle

- In systems which include battery units, SoC of the battery cells is allowed to vary between 30% and 90% over the drive cycle.

- The maximum and minimum numbers of series-connected cells on the DC bus are determined based on open-circuit voltage limits of 200 V and 600 V on the DC bus.

- Mass of the bus without the storage system is considered to be equal to $11,000$ kg. An additional mass of $2,000$ kg is considered for the passengers. At every iteration of the optimization process, for each member of population, this $13,000$ kg mass is summed up with the mass of storage system corresponding to the chosen individual to determine the total mass of the vehicle required for calculating the power demand from speed-versus-time characteristic of the drive cycle.

- For charging the ultracapacitor unit in corresponding stations, the efficiency of charging is 90%.

- Charging of ultracapacitor unit is done under constant power condition. Maximum permissible time for charging at the end-point terminals is $1,200 \ s$.

- The transmission system has a fixed efficiency of 96% with a gearbox of fixed gear ratio of 9.333 : 1.

- Temperature is constant at $25^o \ C$.

Similar to Section 4.1, parameters of the traction motor (required for approach II) are estimated through an analytical procedure based on targeted performance (Fig. 4.15) as:

$$L_m = 2,034.88 \ \mu H \qquad L_{\ell s} = 54.86 \ \mu H \qquad L_{\ell r} = 54.86 \ \mu H$$

$$R_s = 7.43 \ m\Omega \qquad R_r = 4.73 \ m\Omega \qquad \omega_{sy,base} = 157 \ rad/s \tag{4.4}$$
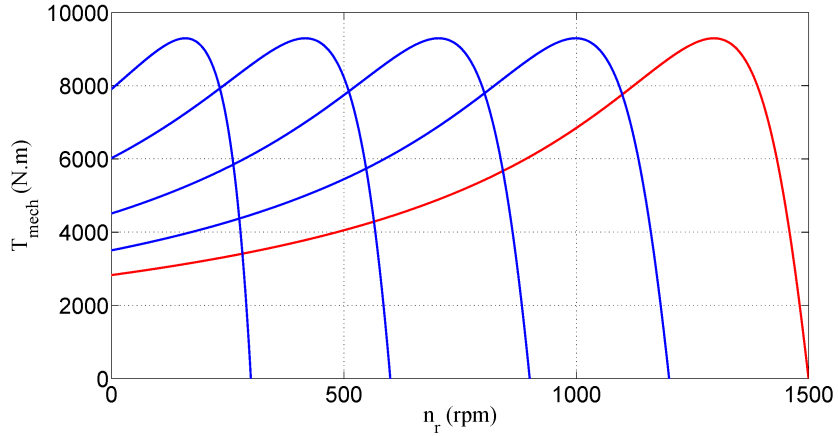
Figure 4.15: Torque-speed characteristic curves of the traction motor used for optimal sizing of the storage system of the electric city bus

The torque-speed characteristic curves of the traction motor are shown in Fig. 4.15. The maximum AC voltage for which the last curve (in red) has been plotted corresponds to series connection of 149 battery cells on the DC when linear modulation is considered for the operation of DC-AC converter. As seen in Fig. 4.15, the traction motor can keep a constant torque of $9,300$ $N.m$ up to around $1,500$ rpm. During solving the optimization problem, as mentioned before, every member of population determines the number of series-connected cells on the DC bus. Using, this number, the base frequency of the traction motor is calculated with the assumption that the ratio of the no-load voltage on the DC bus over the base frequency is fixed for different traction motors. This base frequency along with other parameters of the machine are used to calculate the maximum torque of the corresponding machine by (2.27).

To calculate the power demand, the parameters given in Table 4.16 are used. It should be noted that an additional 30 kW of power is added to the power demand accounting for air conditioning and other auxiliary loads in the bus [100].

4.2.1 Optimal Sizing of the Battery-only Configuration

For the battery-only configuration, two scenarios are studied for the storage unit. The first scenario considers one battery unit installed on the powertrain of the bus responsible for fulfilling the total driving range requirements in daily operation with a single over-night

Table 4.16: Parameters used to calculate power demand

A_f (m^2)	v_w (m/s)	ρ_a (kg/m^3)	C_d	g (m/s^2)	Pr (psi)	r_{wh} (m)	N_g
7.316	2.0	1.202	0.79	9.81	120	0.95	9.333

Table 4.17: Optimization results for the battery-only configuration

Approach	N_{bs}	N_{bp}	Number of battery cells $(N_{bs} \times N_{bp})$	cost of BU considering $ 2 as the price of battery cells ($)	cost of BU considering $ 7 as the price of battery cells ($)	Mass of BU (kg)
I	78	1,546	120,588	241,176	844,116	5,185.3
II	143	737	105,391	210,782	737,737	4,531.8

charge. To complete 240 km on the UDDS drive cycle, optimal sizes of the battery unit based on approaches I and II are as shown in Table 4.17.

Figures 4.16 and 4.17 show variations of SoC of the battery cells and DC bus voltage versus time for the battery-only configuration with the optimally-sized BU based on ap-
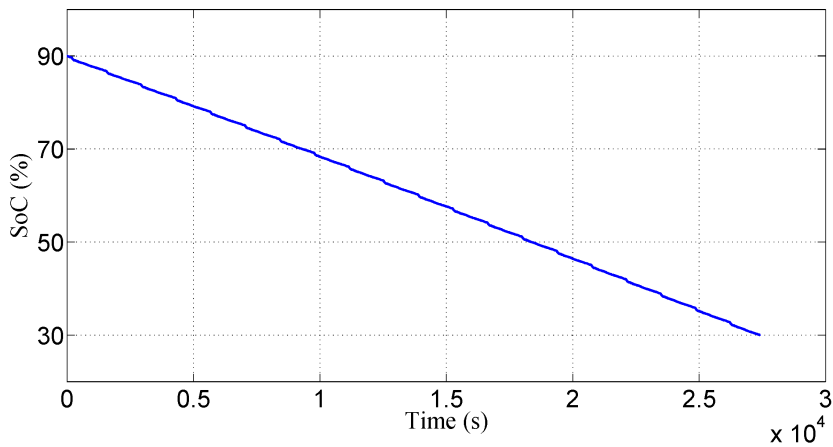
Figure 4.16: SoC of the battery cells versus time for the battery-only configuration with $N_{bs} = 143$ and $N_{bp} = 737$
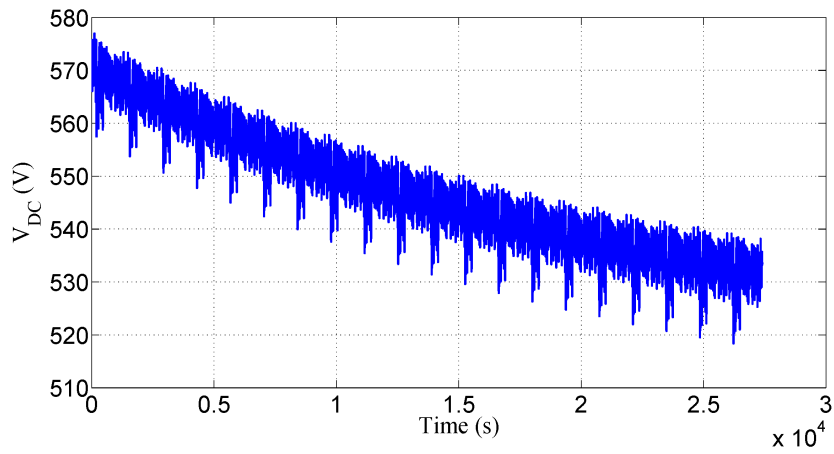
Figure 4.17: DC bus voltage versus time for the battery-only configuration with $N_{bs} = 143$ and $N_{bp} = 737$

proach II. In Fig. 4.18, power demand on the DC bus (P_{DC}) and battery unit power (P_{BU}) versus time are shown for one UDDS cycle. The exact match between these two power
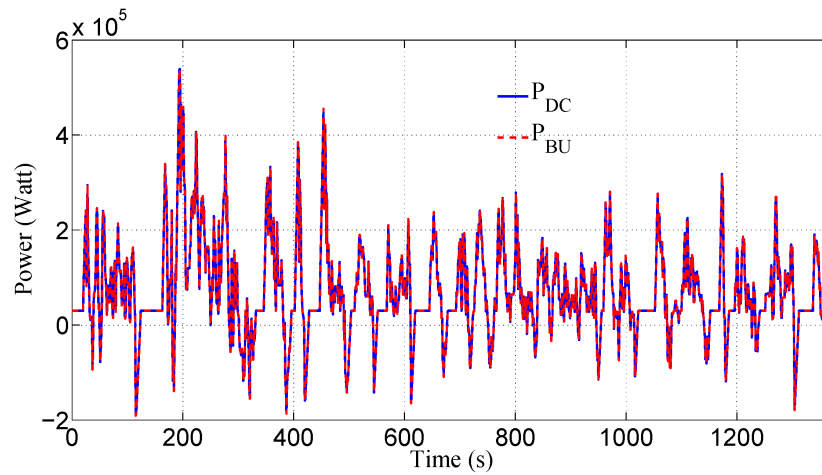
Figure 4.18: Power demand and BU power versus time for the battery-only configuration with $N_{bs} = 143$ and $N_{bp} = 737$

87

components indicates that the equality constraint on the power demand is respected at each sampled interval of the drive cycle.

In the second scenario, a battery-swap strategy is used to replace the discharged battery unit with the newly-charged one at some of the end-point terminals. This reduces the mass of onboard battery unit and, therefore, a smaller room is required for the storage system. The size of storage system varies depending on the number of battery units considered for this scenario and swap frequency during the daily operation. Tables 4.18 and 4.19 show the optimization results in terms of the number of battery replacements (with $N_{swap} = 2$) during daily operation of the bus based on approaches I and II, respectively. Number of replacements determines how many UDDS drive cycles must be completed before the discharged battery unit is swaped with the charged one. The higher the number of replacements is, the lower the optimal size of the battery unit will be. It is seen how battery swap strategy reduces the size of onboard storage unit (the mass of onboard battery unit without any swap is $4,531\ kg$ while it is almost $553\ kg$ with 10 battery replacements, based on approach II). However, battery swap strategy requires facilities capable of faster charging of battery units. For example, with two participating battery units ($N_{swap} = 2$), for ten replacements during a daily operation, the depleted battery unit must be recharged in less than 2×45 minutes (1.5 hour). If constant-current scheme is used for charging the battery unit, the battery cells must be charged at the rate of approximately 2/3 C. In addition to the charging infrastructure requirements, battery swap strategy shortens the cycle life of battery cells. Therefore, in long term, additional cost of purchasing new battery units should be considered. As an example, in the case of 10 battery replacements per day, each battery unit is charged to 90% and discharged to 30% five times during the daily operation of the bus. If we consider the cycle life of the battery cells to be around 800 times at this depth of discharge, it means that the battery units should be permanently

Table 4.18: Optimization results for the battery-only configuration with swap strategy based on approach I

Number of replacements of BU	N_{bs}	N_{bp}	Number of battery cells $(2 \times N_{bs} \times N_{bp})$	cost of the battery units considering $ 2 as the price of battery cells ($)	cost of the battery units considering $ 7 as the price of battery cells ($)	Mass of the onboard battery unit (kg)
2	93	607	112,902	225,804	790,314	2,427.4
4	112	249	55,776	111,552	390,432	1,199.2
10	101	126	25,452	50,904	178,164	547.2

Table 4.19: Optimization results for the battery-only configuration with swap strategy based on approach II

Number of replacements of BU	N_{bs}	N_{bp}	Number of battery cells $(2 \times N_{bs} \times N_{bp})$	cost of the battery units considering $ 2 as the price of battery cells ($)	cost of the battery units considering $ 7 as the price of battery cells ($)	Mass of the onboard battery unit (kg)
2	146	346	101,032	202,064	707,224	2,172.2
4	145	174	50,460	100,920	353,220	1,084.9
10	55	234	25,740	51,480	180,180	553.4

replaced with new ones after around 160 days, while, in the case of no replacement, the battery unit can be used for 800 days.

Table 4.20: Optimization results for the ultracapacitor-only configuration

Approach	N_{us}	N_{up}	Number of ultracapacitor cells $(N_{us} \times N_{up})$	cost of UC considering $ 40 as the price of ultracapacitor cells ($)	cost of UC considering $ 50 as the price of ultracapacitor cells ($)	Mass of UC (kg)
I	222	82	18,204	728,160	910,200	9,284.0
II	218	61	13,298	531,920	664,900	6,782.0

4.2.2   Optimal Sizing of the Ultracapacitor-only Configuration

In the case of ultracapacitor-only configuration, the optimal size of the ultracapacitor unit with its corresponding cost are given in Table 4.20 based on approaches I and II. Figures 4.19 shows variation of the DC bus voltage versus time for two UDDS cycle with $N_{us} = 218$ and $N_{up} = 61$. As seen in this figure, the ultracapacitor unit is charged between the consecutive UDDS cycles with the charging power calculated to be 95.3 kW extracted from the grid (charging time has not been shown in this figure). Unlike the case of battery-only configuration, in the ultracapacitor-only configuration, the DC bus experiences a large voltage variation between each two consecutive charging, which can be a disadvantage for operation of the inverter from control point of view. In Fig. 4.20, power demand and ultracapacitor unit power versus time are shown for two UDDS cycles. The patterns shown in Figs. 4.19 and 4.20 are repeated 10 times during daily operation of the city bus (20 repetitions of the UDDS cycle).

An important point to notice about the ultracapacitor-only configuration is that the

90
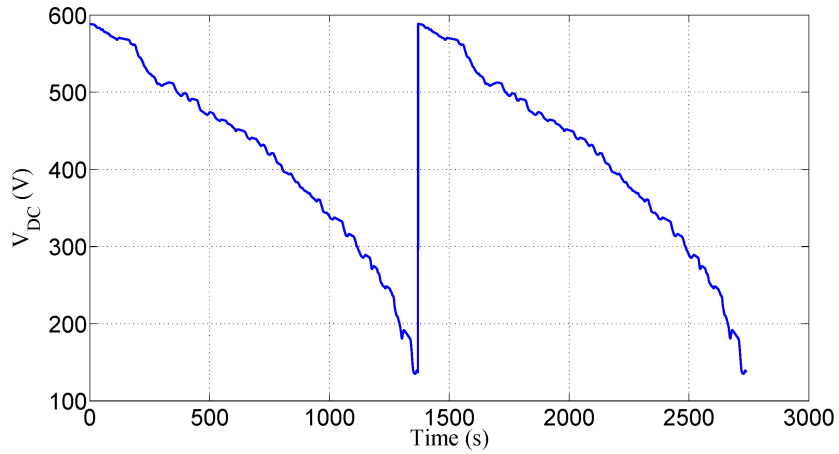
Figure 4.19: DC bus voltage versus time for the ultracapacitor-only configuration with $N_{us} = 218$ and $N_{up} = 61$
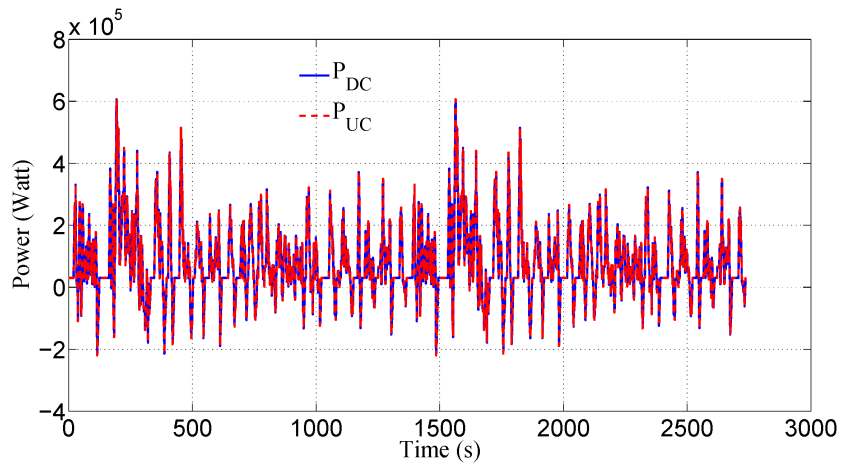
Figure 4.20: Power demand and UC power versus time for the ultracapacitor-only configuration with $N_{us} = 218$ and $N_{up} = 61$

size of UC can be reduced if more charging stations are considered over the course of the drive cycle [8]. For example, along with charging at the end of each UDDS cycle, charging can take place at four more points of the UDDS cycle as shown by red arrows in Fig.

91
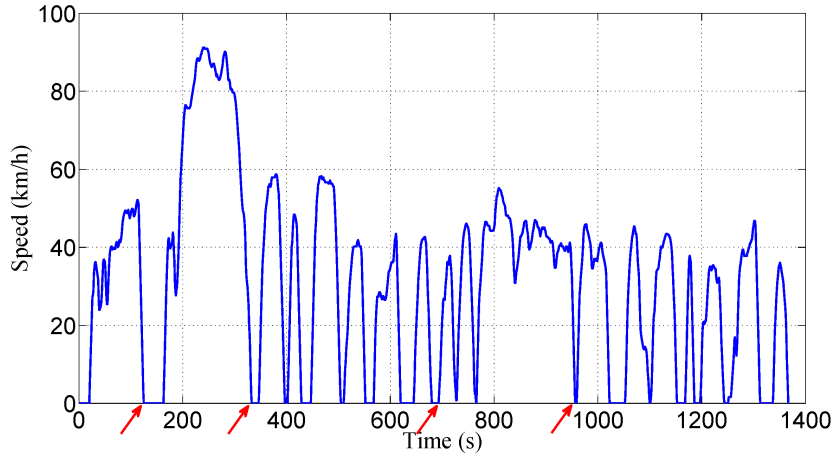
Figure 4.21: Charging points on the UDDS drive cycle

4.21 (points corresponding to $t = 126$, 334, 694, and 958 s). Assuming 60 s limit on the charging time at the additional points (charging times at these points are chosen to be much shorter than those at the end-point terminals as the bus is in the middle of its trip over the course of each UDDS cycle) and 95.3 kW limit on charging power available from the grid, using approach II, the optimal size of UC will be $N_{us} = 218$ and $N_{up} = 46$. It is seen that with more charging points included, the mass of ultracapacitor unit drops from 6, 782.0 kg to 5, 114.3 kg. Table 4.21 summarizes the optimization results for the two cases of (i) UC charged only at the end-point terminals and (ii) charging at $t = 126$, 334, 694, and 958 s of each UDDS drive cycle is considered in addition to charging at the end-point terminals.

Table 4.21: Comparison of the optimization results for the ultracapacitor-only configuration for the two cases of (i) UC charged only at the end-point terminals and (ii) charging at $t = 126$, 334, 694, and 958 s of each UDDS drive cycle is considered in addition to charging at the end-point terminals

	N_{us}	N_{up}	Number of ultracapacitor cells $(N_{us} \times N_{up})$	Mass of UC (kg)
case (i)	218	61	13,298	6,782.0
case (ii)	218	46	10,028	5,114.3

4.2.3 Optimal Sizing of the Battery-Ultracapacitor HESS Configuration

In the case of ultracapacitor-only configuration with $N_{us} = 218$ and $N_{up} = 61$, to meet the daily operational power and energy requirements, the maximum charging power for the ultracapacitor unit is 95.3 kW. A battery-ultracapacitor HESS configuration makes it possible to have a limit on the charging power of UC, if it is required to do so. When a limit is placed on the charging power of UC, the ultracapacitor cells cannot participate in meeting energy requirement of the powertrain as in the case of ultracapacitor-only configuration. However, this is compensated for by participation of battery cells in energy management in the HESS configuration. Table 4.22 shows the results of optimization when the battery unit is replaced once (with $N_{swap} = 2$) during the daily operation of the city bus (after 10 repetitions of the UDDS cycle), the limit on the charging power of UC is equal to 50 kW, $C_b = \$ 7$, $C_u = \$ 50$, and $C_{con} = \$ 250$ per kW. It should be noted that when solving

Table 4.22: Optimization results for the battery-ultracapacitor HESS configuration with $C_b = \$ 7$, $C_u = \$ 50$, $C_{con} = \$ 250$ per kW, and a single swap of BU during the daily operation when the limit on the charging power of UC is equal to 50 kW

Approach	N_{bs}	N_{bp}	N_{us}	N_{up}	DC-DC rating (kW)	Cost ($)	Total mass of the onboard storage units (kg)
I	36	941	222	32	63.224	845,263	5,079.8
II	33	795	222	31	46.430	722,997	4,637.9

the problem of optimal sizing for the battery-ultracapacitor HESS configuration, for both approaches I and II, efficiencies of the DC-DC converter during step-down and step-up modes of operation are calculated using Tables 4.3 and 4.4, respectively. Using Table 4.22, it can be calculated that using the HESS configuration, mass of the storage system is reduced from $6,782.0\ kg$ in the case of ultracapacitor-only configuration to $4,637.9\ kg$ based on approach II. Moreover, as mentioned before, the HESS configuration keeps the battery unit immune from fast charging/discharging current (compared to the case of battery-only configuration) when the vehicle undergoes unpredictable driving patterns.

As mentioned before, when solving the problem of optimal sizing for the battery-ultracapacitor HESS configuration, the result of optimization can be affected by the choice of prices of the battery and ultracapacitor cells and the DC-DC converter per kW as included in calculating the cost using (3.5). Table 4.23 provides a comparison among the optimization results for four different sets of prices of the storage cells and the DC-DC converter per kW. As this table shows, when the ultracapacitor cells are not very expensive compared to the battery cells ($C_b = \$ 2$, $C_u = \$ 10$, and $C_{con} = \$ 100$ per kW),

the optimal size of UC is found in such a way that the maximum charging power of the ultracapacitor unit becomes equal to the limit set for this power component (50 kW). Once the ratio of the price of ultracapacitor cells to that of the battery cells gets larger, the size of UC decreases resulting in more participation of the battery cells in meeting the power requirements of the city bus over the course of its drive cycle. In addition, it is seen that when such a condition occurs, the price of DC-DC converter per kW has an inverse relationship with the size of battery unit. This has been shown in the last two rows of Table 4.23 where $C_b = \$ 2$ and $C_u = \$ 40$ for both rows. In the former case, the price of DC-DC converter is \$ 250 per kW while in the latter case, it is \$ 100 per kW. Therefore, in the latter case, the optimal size of BU is larger than that in the former case indicating more participation of the battery unit in meeting the power demand while the reduced size of UC results in lower cost of the storage system.

Figures 4.22 and 4.23 show variations of SoC of the battery cells and the terminal voltage of BU versus time based on approach II with $N_{bs} = 33$, $N_{bp} = 795$, $N_{us} = 222$, $N_{up} = 31$, and $P_{con} = 46.430 \, kW$. As seen in these figures, there are two identical segments. This similarity is the result of the single battery replacement over the course of the drive cycle. Variation of the DC bus voltage versus time is shown in Fig. 4.24 for the daily operation of the bus (20 repetitions of the UDDS cycle). Like the case of ultracapacitor-only configuration, as the DC bus is solidly connected to the terminals of UC, the DC bus voltage experiences fast and wide variations. Figure 4.25 shows the power demand and BU and UC power components versus time for one UDDS cycle.

Table 4.23: Comparison of the optimization results for the battery-ultracapacitor HESS configuration based on four sets of prices of the battery and ultracapacitor cells and the DC-DC converter with a single swap of BU during the daily operation when the limit on the charging power of UC is equal to 50 kW

Prices of the battery cell, the ultracapacitor cell, and the DC-DC converter	N_{bs}	N_{bp}	N_{us}	N_{up}	DC-DC rating (kW)	Cost ($)	Total mass of the onboard storage units (kg)	Maximum power required for charging of UC (kW)
$C_b = \$\ 2$, $C_u = \$\ 10$, and $C_{con} = \$\ 100$ per kW	33	769	222	32	44.481	176,996	4,714.3	49.999
$C_b = \$\ 7$, $C_u = \$\ 50$, and $C_{con} = \$\ 250$ per kW	33	795	222	31	46.430	722,997	4,637.9	48.712
$C_b = \$\ 2$, $C_u = \$\ 40$, and $C_{con} = \$\ 250$ per kW	48	1,057	222	6	133.281	289,544	2,861.0	8.497
$C_b = \$\ 2$, $C_u = \$\ 40$, and $C_{con} = \$\ 100$ per kW	46	1,316	222	1	270.008	278,025	2,716.3	1.462
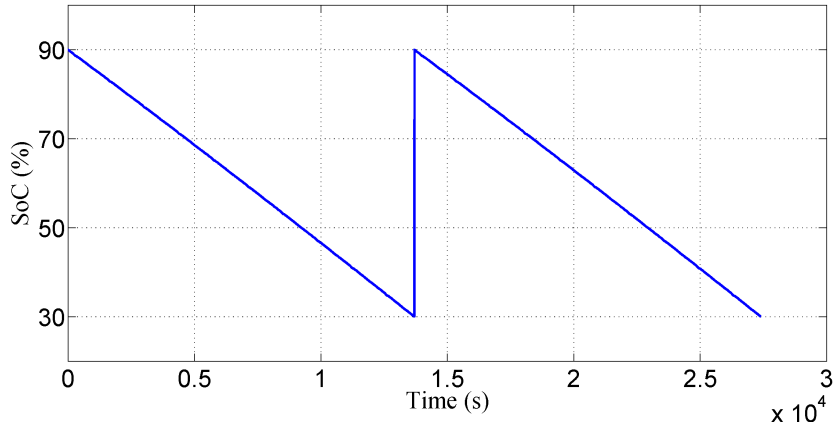
Figure 4.22: SoC of the battery cells versus time for the battery-ultracapacitor HESS configuration with $N_{bs} = 33$, $N_{bp} = 795$, $N_{us} = 222$, $N_{up} = 31$, and $P_{con} = 46.430 \ kW$
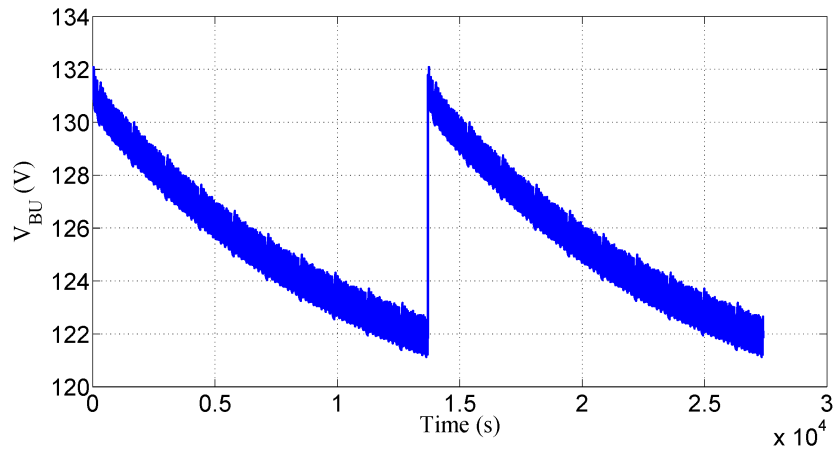
Figure 4.23: Terminal voltage of BU versus time for the battery-ultracapacitor HESS configuration with $N_{bs} = 33$, $N_{bp} = 795$, $N_{us} = 222$, $N_{up} = 31$, and $P_{con} = 46.430 \ kW$

4.3   Summary

In this chapter, the results of optimal sizing of the storage systems were provided for a small-size, long-range electric car and an electric city bus. For the first case, the problem

of optimal sizing was solved for the battery-only configuration while the latter included the battery-only, the ultracapacitor-only, and the battery-ultracapacitor HESS configurations.
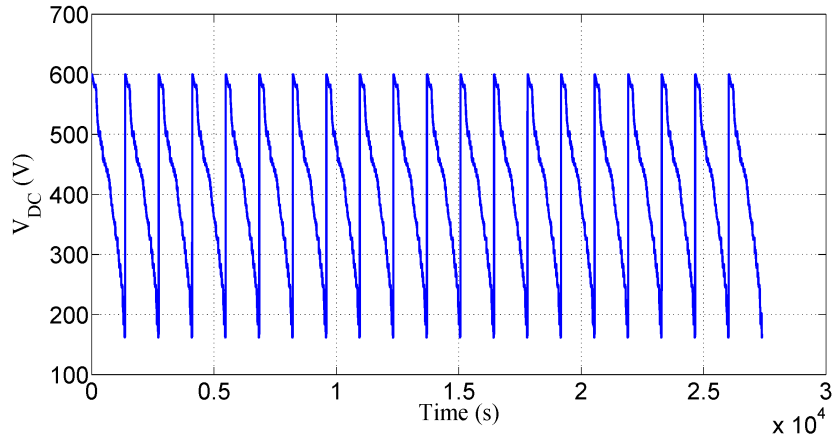
Figure 4.24: DC bus voltage versus time for the battery-ultracapacitor HESS configuration with $N_{bs} = 33$, $N_{bp} = 795$, $N_{us} = 222$, $N_{up} = 31$, and $P_{con} = 46.430$ kW
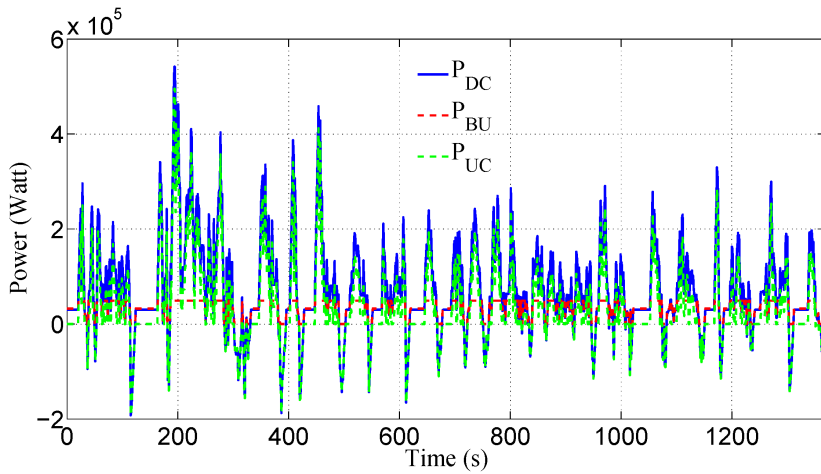
Figure 4.25: Power demand and BU and UC powers versus time for the battery-ultracapacitor HESS configuration with $N_{bs} = 33$, $N_{bp} = 795$, $N_{us} = 222$, $N_{up} = 31$, and $P_{con} = 46.430$ kW

Beside the optimization results, the chapter provided simulation results for different cases confirming how the constraints of the problem were respected.

Chapter 5

Conclusions, Contributions, and Future Work

5.1   Summary and Conclusions

In the following, a summary and some conclusions based on the previous chapters are given.

- Due to the issues such as concerns about environmental pollution, rapid increase in fuel cost, and depletion of fossil fuel reserves, Electric Vehicles (EVs)/Hybrid Electric Vehicles (HEVs) have drawn significant attention in recent decades.

- One of the key components of every EV/HEV is the Energy Storage System (ESS). ESS consists of a source or a combination of two or more sources (when more than one ESS device is installed, the structure can also be called a hybrid energy storage system or HESS), which provides electric power to the drivetrain in an EV/HEV.

- Batteries and ultracapacitors are two major types of ESS in EVs/HEVs. Batteries are well-known for their high specific energy while suffering from their low specific power. Ultracapacitors have very high specific power and low specific energy. Therefore, ultracapacitors have application in the storage systems where they can be charged frequently over the course of drive cycle and/or hybridized with battery units in a battery-ultracapacitor HESS configuration.

- There are different structures for hybridizing the ESS based on a battery unit (BU) and an ultracapacitor unit (UC) and taking advantage of the best of the two worlds. In most of the cases, Power Electronic (PE) converters are used as an interface between BU, UC, and the DC bus. Choice of a specific configuration depends on various factors such as cost, flexibility, and level of reliability required from the system.

- Cost of the storage system is a significant portion of every EV. Price of an EV varies depending on the types of ESS devices installed in the powertrain and whether PE converter(s) exists in the interfacing infrastructure between the storage unit(s) and the DC bus. Due to limitation of money and available resources, optimal sizing of the storage system is a requirement which is beneficial for both EV manufacturers and costumers.

- A quantitative analysis is required to determine the optimal size of the storage system for an EV using the dimensions of the vehicle and driving conditions including road parameters and speed-versus-time profile. By this analysis, the optimum numbers of parallel branches and series-connected cells in each branch of the storage units interfaced to the DC bus in electric powertrains are determined. In addition, in the case of a HESS, if any DC-DC converter exists in the interfacing infrastructure, its

101

rating is also determined through the course of this quantitative analysis.

- Mathematical models of battery and ultracapacitor cells bear differential equations. To deal with these differential equations in the optimization platform, a practical method is to discretize the power demand using a specific sampling time and convert all continuous differential equations to their equivalent discrete forms.

- The problem of optimal sizing of battery-only and ultracapacitor-only storage systems in electric vehicle applications is an integer nonlinear programming (INLP) problem (in the case of a battery-ultracapacitor HESS configuration, it is a mixed-integer nonlinear programming (MINLP) problem) with quite a large number of constraints, considering the discretized equations of the system at every sampled interval. Due to nonlinearity of the problem, existence of integer values in the domain of solutions (the numbers of parallel branches of the storage devices and series-connected cells in each branch), and excessive number of constraints, conventional gradient-based methods cannot be used to optimize the problem. In this thesis, a population-based metaheuristic algorithm named Teaching-Learning-Based Optimization (TLBO) is used for solving the problem of optimal sizing of the storage systems.

- Choice of a storage device (battery and/or ultracapacitor in this study) for installing in the powertrain of EVs depends on the power profile of the vehicles. For small-size, long-range vehicles, while the battery-ultracapacitor HESS is a possible choice, battery-only configuration is the better option from economical viewpoint. It should be noted that the ultracapacitor-only configuration cannot be used as the powertrain of a small-size, long-range vehicle (no frequent charging considered for this vehicle) due to low specific energy of ultracapacitor cells available in the market. For a vehicle like an electric city bus, the scenario can be different as there is possibility of

frequent charging for the ultracapacitor units and swapping strategy for the battery units. Therefore, all three configurations of battery-only, ultracapacitor-only, and battery-ultracapacitor HESS are possible candidates for this class of vehicles.

- In a battery electric vehicle, performance indexes such as duration of $0 - 60 \ mile/h$ acceleration and top speed vary with the initial SoC of the battery cells and the road conditions including wind speed and road grade. At lower values of SoC, higher wind speeds, and/or larger grades of the road, the vehicle can reach speed of $60 \ mile/h$ over a longer time period with its achievable top speed reduced.

5.2   Contributions

The contributions of this research are:

- Developing a flexible optimization platform which can be used for the purpose of optimal sizing of battery/ultracapacitor-based energy storage system of any electric vehicle if the vehicle's dimension and its driving conditions are known a priori; in formulating the optimization problem, different constraints such as limits on SoC, current, and power of the battery cells, current and power of the ultracapacitor cells, voltage conversion of the DC-DC converter, DC bus voltage, and operation characteristics of the inverter and the traction motor are taken into consideration.

- Implementing a metaheuristic population-based algorithm named Teaching-Learning-Based Optimization (TLBO) technique in MATLAB environment; the implemented technique is a powerful optimization tool that can be used for solving different types of optimization problems (linear, nonlinear, convex, non-convex, continuous, discrete, etc.)

- Developing a simulation platform which includes electrical models of powertrain components, i.e., battery and ultracapacitor cells, DC-AC converter, and Traction Motor; the models developed for the DC-AC converter and the traction motor can also be used for studying any induction motor-based variable-speed drive.

- Quantitative analysis of the performance of two popular classes of EV, i.e., small-size long-range car and city bus, equipped with the optimally-sized ESS.

5.3   Future Work

This research can be extended based on the following future work:

- Inclusion of battery aging in the optimization platform.

- Studying the effect of temperature variations of the storage devices on the optimization results.

- Including the detailed model of DC-DC converter interfacing BU and UC to the DC bus.

- Considering the uncertainty associated with the parameters used in the modeling of the storage devices.

- Including the control system and charge balancing circuits in the structure of storage units in the optimization platform.

- Solving the problem of optimal sizing with other types of traction motors such as permanent magnet synchronous machine (PMSM).

References

[1] A. Emadi, "Transportation 2.0," *IEEE Power and Energy Magazine*, Vol. 9, No. 4, pp. 18-29, July-Aug. 2011.

[2] A. Ostadi and M. Kazerani, "Optimal Sizing of the Battery Unit in a Plug-in Electric Vehicle," *IEEE Transactions on Vehicular Technology*, Vol. 63, No. 7, pp. 3077-3084, Sept. 2014.

[3] Karl BA. Mikkelsen (2010), *Design and Evaluation of Hybrid Energy Storage Systems for Electric Powertrains*, Master of Applied Science, University of Waterloo.

[4] A. Khaligh and Z. Li, "Battery, ultracapacitor, fuel cell, and hybrid energy storage systems for electric, hybrid electric, fuel cell and plug-in hybrid electric vehicles-state of the art," *IEEE Transactions on Vehicular Technology*, Vol. 59, No. 6, pp. 2806-2814, July 2010.

[5] A. Emadi, K. Rajashekara, S.S. Williamson, and S. Lukic, "Topological overview of hybrid electric and fuel cell vehicular power system architectures and configurations," *IEEE Transactions on Vehicular Technology*, Vol. 54, No. 3, pp. 763-770, May 2005.

[6] O. Caumont, P. Le Moigne, C. Rombant, X. Muneret, and P. Lenain, "Energy gauge for lead-acid batteries in electric vehicles," *IEEE Transactions on Energy Conversion*, Vol. 15, No. 3, pp. 354-360, Sept. 2000.

[7] K. Rajashekara, "Present Status and Future Trends in Electric Vehicle Propulsion Technologies," *IEEE Journal of Emerging and Selected Topics in Power Electronics*, Vol. 1, No. 1, pp. 3-10, Mar. 2013.

[8] A Sustainable Solution for Public Transportation, SINAUTEC Automobile Technologies LLC, *http://www.sinautecus.com*

[9] J.M. Miller, "Hybrid Electric Vehicle Propulsion System Architectures of the e-CVT Type," *IEEE Transactions on Power Electronics*, Vol. 2, No. 3, pp. 756-767, May 2006.

[10] S.M. Lukic, J Cao, R.C. Bansal, F. Rodriguez, and A. Emadi, "Energy Storage systems for Automotive Applications," *IEEE Transactions on Industrial Electronics*, Vol. 55, No. 6, pp. 2258-2267, June 2008.

[11] V. Galdi, L. Ippolito, A. Piccolo, and A. Vaccaro, "A Genetic Based Methodology for Hybrid Electric Vehicle Sizing," *Soft Computing*, Vol. 5, No. 6, pp. 451-457, Dec. 2001.

[12] S. Fish and T.B. Savoie, "Simulation-Based Optimal Sizing of Hybrid Electric Vehicle Components for Specific Combat Missions," *IEEE Transactions on Magnetics*, Vol. 37, No. 1, pp. 485-488, Jan. 2001.

[13] C. Desai (2010), *Design and Optimization of Hybrid Electric Vehicle Drivetrain and Control Strategy Parameters Using Evolutionary Algorithms*, Master of Science, Concordia University.

[14] E. Cacciatori, N. D. Vaughan, and J. Marco, "Energy Management Strategies for a parallel hybrid electric powertrain: Fuel economy optimisation with driveability requirements," *Proceedings of IET Hybrid Vehicle Conference*, pp. 157-172, Coventry, England, 12-13 Dec. 2006.

[15] K. Chen, Y. Deng, F. Zhou, G. Sun, and Y. Yuan, "Control Strategy Optimization for Hybrid Electric Vehicle Based on Particle Swarm and Simulated Annealing Algorithm," *Proceedings of International Conference on Electric Information and Control Engineering (ICEICE)*, pp. 2054-2057, Wuhan, China, 15-17 Apr. 2011.

[16] S. Lu, K.A. Corzine, and M. Ferdowsi, "A New Battery/Ultracapacitor Energy Storage System Design and Its Motor Drive Integration for Hybrid Electric Vehicles," *IEEE Transactions on Vehicular Technology*, Vol. 56, No. 4, pp. 1516-1523, July 2007.

[17] G. Souffran, L. Miegeville, and P. Guerin, "Simulation of Real-World Vehicle Missions Using a Stochastic Markov Model for Optimal Powertrain Sizing," *IEEE Transactions on Vehicular Technology*, Vol. 61, No. 8, pp. 3454-3465, Oct. 2012.

[18] X. Liu, D. Diallo, and C. Marchand, "Cycle-Based Design Methodology of Hybrid Electric Vehicle Powertrain: Application to Fuel Cell Vehicles," *Proceedings of IEEE Vehicle Power and Propulsion Conference (VPPC)*, pp. 1853-1857, Dearborn, MI, USA, 7-10 Sept. 2009.

[19] S. Overington and S. Rajakaruna, "A Modified Method for the Sizing of the Plug-In Hybrid Electric Vehicle Propulsion Devices," *Proceedings of Australasian Universities Power Engineering Conference (AUPEC)*, pp. 1-7, Brisbane, AUS, 25-28 Sept. 2011.

[20] S.J. Moura, D.S. Callaway, H.K. Fathy, and J.L. Stein, "Impact of Battery Sizing on Stochastic Optimal Power Management in Plug-in Hybrid Electric Vehicles," *Pro-*

ceedings of International Conference on Vehicular Technology and Safety, pp. 96-102, Columbus, OH, USA, 22-24 Sept. 2008.

[21] S.G. Wiransingha and A. Emadi, "Classification and Review of Control Strategies for Plug-In Hybrid Electric Vehicles," *IEEE Transactions on Vehicular Technology*, Vol. 60, No. 1, pp. 111-122, Jan. 2011.

[22] N. Jalil, N. A. Kheir, and M. Salman, "A Rule-Based Energy Management Strategy for a Series Hybrid Vehicle," *Proceedings of American Control Conference*, pp. 689-693, Albuquerque, NM, USA, 4-6 June 1997.

[23] G. Steinmauer and L. d. Re, "Optimal control of dual power sources," *Proceedings of IEEE International Conference on Control Applications (CCA)*, pp. 422-427, Mexico City, 5-7 Sept. 2001.

[24] B.M. Baumann, G. Washington, B.C. Glenn, and G. Rizzoni, "Mechatronic Design and Control of Hybrid Electric Vehicles," *IEEE Transactions on Mechantronics*, Vol. 5, No. 1, pp. 58-72, Mar. 2000.

[25] E. D. Tate and S. P. Boyd, "Finding ultimate limits of performance for hybrid electric vehicles," *Proceedings of Future Transportation Technology Conference, Society of Automotive Engineers (SAE)*, Aug. 2000.

[26] X. Liu, Q. Zhang, and C. Zhu, "Design of battery and ultracapacitor multiple energy storage in hybrid electric vehicle," *Proceedings of IEEE Vehicle Power and Propulsion Conference (VPPC)*, pp. 1395-1398, Dearborn, MI, USA, 7-10 Sept. 2009.

[27] Li-C. Fang and Shi-Y. Qin, "Concurrent Optimization for Parameters of Powertrain and Control System of Hybrid Electric Vehicle Based on Multi-Objective Genetic Al-

gorithms," *Proceedings of SICE-ICASE International Joint Conference*, pp. 2424-2429, Busan, South Korea, 18-21 Oct. 2006.

[28] E. Tara, S. Shahidinejad, S. Filizadeh, and E. Bibeau, "Battery Storage Sizing in a Retrofitted Plug-in Hybrid Electric Vehicle," *IEEE Transactions on Vehicular Technology*, Vol. 59, No. 6, pp. 2786-2794, July 2010.

[29] B. Su-Ming Fan Rosario (2011), *Multidisciplinary Optimization of Hybrid Electric Vehicles: Component Sizing and Power Management Logic*, PhD, University of Waterloo, Canada.

[30] L. Wang, E.G. Collins, and H. Li, "Optimal Design and Real-Time Control for Energy Management in Electric Vehicles," *IEEE Transactions on Vehicular Technology*, Vol. 60, No. 4, pp. 1419-1429, May 2011.

[31] N. Murgovski, L.M. Johannesson, and J. Sjoberg, "Engine On/Off Control for Dimensioning Hybrid Electric Powertrains via Convex Optimization," *IEEE Transactions on Vehicular Technology*, Vol. 62, No. 7, pp. 2949-2962, Sept. 2013.

[32] Y. Wu and H. Gao, "Optimization of Fuel Cell and Supercapacitor for Fuel-Cell Electric Vehicles," *IEEE Transactions on Vehicular Technology*, Vol. 55, No. 6, pp. 1748-1755, Nov. 2006.

[33] M. Jain, C. Desai, and S.S. Williamson, "Genetic algorithm based optimal powertrain component sizing and control strategy design for a fuel cell hybrid electric bus," *Proceedings of IEEE Vehicle Power and Propulsion Conference (VPPC)*, pp. 980-985, Dearborn, MI, USA, 7-10 Sept. 2009.

[34] M.M. Amin and O.A. Mohammed, "A three-phase high frequency semi-controlled battery charging power converter for plug-in hybrid electric vehicles," *In Proceedings*

of IEEE Energy Conversion Congress and Exposition (ECCE), pp. 2641-2648, Phoenix, AZ, USA, 17-22 Sept. 2011.

[35] M. Yilmaz and P.T. Krein, "Review of Battery Charger Topologies, Charging Power Levels, and Infrastructure for Plug-In Electric and Hybrid Vehicles," *IEEE Transactions on Power Electronics*, Vol. 28, No. 5, pp. 2151-2169, May 2013.

[36] Q. Dai, T. Cai, S. Duan, and F. Zhao, "Stochastic Modeling and Forecasting of Load Demand for Electric Bus Battery-Swap Station," *IEEE Transactions on Power Delivery*, Vol. 29, No. 4, pp. 1909-1917, Aug. 2014.

[37] I. Aharon and A. Kuperman, "Topological Overview of Powertrains for Battery-Powered Vehicles with Range Extenders," *IEEE Transactions on Power Electronics*, Vol. 26, No. 3, pp. 868-876, Mar. 2011.

[38] L. Gao, R.A. Dougal, and S. Liu, "Active Power Sharing in Hybrid Battery/Capacitor Power Sources," *Proceedings of Eighteenth Annual IEEE Applied Power Electronics Conference and Exposition (APEC)*, pp. 497-503, Miami Beach, FL, USA, 9-13 Feb. 2003.

[39] A.L. Allegre, A. Bouscayrol, and R. Trigui, "Influence of control strategies on battery/supercapacitor hybrid energy storage systems for traction applications," *Proceedings of IEEE Vehicle Power and Propulsion Conference*, pp. 213-220, Dearborn, MI, USA, 7-10 Sept. 2009.

[40] O. Onar and A. Khaligh, "Dynamic modeling and control of a cascaded active battery/ultracapacitor based vehicular power system," *Proceedings of IEEE Vehicle Power and Propulsion Conference*, pp. 1-4, Harbin, China, 3-5 Sept. 2008.

[41] T.P. Kohler, D. Buecherl, and H-Georg Herzog, "Investigation of control strategies for hybrid energy storage systems in hybrid electric vehicles," *Proceedings of IEEE Vehicle Power and Propulsion Conference*, pp. 1687-1693, Dearborn, MI, USA, 7-10 Sept. 2009.

[42] Z. Amjadi and S.S. Williamson, "Power-Electronics-based solutions for plug-in hybrid electric vehicle energy storage and management systems," *IEEE Transactions on Industrial Electronics*, Vol. 57, Issue 2, pp. 608-616, Feb. 2010.

[43] L. Gao, R.A. Dougal, and S. Liu, "Power enhancement of an actively controlled battery/ultracapacitor hybrid," *IEEE Transactions on Power Electronics*, Vol. 20, Issue 1, pp. 236-243, Jan. 2005.

[44] Neenu. M. PG and S. Muthukumaran, "A Battery with Ultra-capacitor Hybrid Energy Storage System in Electric Vehicles," *Proceedings of IEEE International Conference on Advances in Engineering, Science, and Management (ICAESM)*, pp. 731-735, Nagapattinam, India, 30-31 Mar. 2012.

[45] J. Cao and A. Emadi, "A new battery/ultra-capacitor hybrid energy storage system for electric, hybrid and plug-in hybrid electric vehicles," *Proceedings of IEEE Vehicle Power and Propulsion Conference*, pp.941-946, Dearborn, MI, USA, 7-10 Sept. 2009.

[46] X. Yan and D. Patterson, "Improvement of Drive Range, Acceleration and Deceleration Performance, in an Electric Vehicle Propulsion System," *Proceedings of 30th Annual IEEE Power Electronics Specialist Conference (PESC)*, pp. 638-643, Charleston, SC, USA, 27 June-1 July 1999.

[47] A. Xu, S. Xie, and X. Liu, "Dynamic voltage equalization for series connected ultra-capacitors in EV/HEV applications," *IEEE Transactions on Vehicular Technology*, Vol. 58, No. 8, pp. 3981-3987, Oct. 2009.

[48] Hong-S. Park, Chong-E. Kim, Chol-H. Kim, Gun-W. Moon, and Joong-H. Lee, "A modularized charge equalizer for an HEV Lithium-Ion battery string," *IEEE Transactions on Industrial Electronics*, Vol. 56, No. 5, pp. 1464-1476, May 2009.

[49] G. Guidi, T.M. Undeland, and Y. Hori, "Optimized Power Electronics Interface for Auxiliary Power Buffer Based on Supercapacitors," *Proceedings of IEEE Vehicle Power and Propulsion Conference (VPPC)*, pp. 1-6, Harbin, China, 3-5 Sept. 2008.

[50] G. Guidi, T.M. Undeland, and Y. Hori, *Effectiveness of Supercapacitors as Power-Assist in Pure EV Using a Sodium-Nickel Chloride Battery as Main Energy Storage*, Presnted at EVS24 International Battery, Hybrid and Fuel Cell Electric Vehicle Symposium, Stavanger, Norway, 13-16 May 2009.

[51] A.M. Rahimi and A. Emadi, "Active Damping in DC/DC Power Electronic Converters: A Novel Method to Overcome the Problems of Constant Power Loads," *IEEE Transactions on Industrial Electronics*, Vol. 56, No. 5, pp. 1428-1439, May 2009.

[52] C.N. Onwuchekwa and A. Kwasinski, "Analysis of Boundary Control for Buck Converters with Instantaneous Constant-Power Loads," *IEEE Transactions on Power Electronics*, Vol. 25, No. 8, pp. 2018-2032, Aug. 2010.

[53] F.S. Garcia, A.A. Ferriera, and J.A. Pomilio, "Control Strategy for Battery-Ultracapacitor Hybrid Energy Storage System," *Proceedins of 24th Annual IEEE Applied Power Electronics Conference and Exposition*, pp. 826-832, Washington, DC, USA, 15-19 Feb. 2009.

[54] S. Han and D. Divan, "Bidirectional DC-DC converters for plug-in hybrid electric vehicle (PHEV) applications," *Proceedings of 23rd Annual IEEE Applied Power Electronics Conference*, pp.784-789, Austin, TX, USA, 24-28 Feb. 2008.

[55] N.M.L. Tan, T. Abe, and H. Akagi, "Topology and Application of Bidirectional Isolated DC-DC Converters," *Proceedings of 8th International Conference on Power Electronics and ECCE (ICPE & ECCE)*, pp. 1039-1046, Jeju, South Korea, 30 May-3 June 2011.

[56] S. Rodriguez, N. Munichandraiah, and A.K. Shukla, "A review of state-of-charge indication of batteries by means of a.c. impedance measurements," *Journal of Power Source*, Vol. 87, Issue 1, pp. 12-20, Apr. 2000.

[57] D. Vinh Do, C. Forgez, K. El Kadri BenKara, and G. Friedrich, "Impedance observer for a Li-Ion battery using Kalman Filter," *IEEE Transactions on Vehicular Technology*, Vol. 58, No. 8, pp. 3930-3937, Oct. 2009.

[58] J.M. Miller (2004), *Propulsion Systems for Hybrid Vehicles*, London, United Kingdom: The Institute of Electrical Engineers.

[59] F. Huet, "A review of impedance measurements for determination of the state-of-charge or state-of-health of secondary batteries," *Journal of Power Source*, Vol. 70, Issue 1, pp. 59-69, Jan. 1998.

[60] L.P. Mandal and R.W. Cox, "A Transient-Based Approach to Estimation of the Electrical Parameters of a Lead-Acid Battery Model," *Proceedings of IEEE Energy Conversion Congress and Exposition (ECCE)*, pp. 4238-4242, Atlanta, GA, USA, 12-16 Sept. 2010.

[61] Shyh-j. Huang, Fu-S. Pai, and Bo-G. Huang, "A matching design for ultra-capacitor and Li-Ion battery cooperation in electric wheel motors," *Proceedings of SICE Annual Conference*, pp. 2646-2649, Taipei, Taiwan, 18-21 Aug. 2010.

[62] M. Chen and G.A. Rincon-Mora, "Accurate Electrical Battery Model Capable of Predicting Runtime and I-V Performance," *IEEE Transactions on Energy Conversion*, Vol. 21, No. 2, pp. 504-511, June 2006.

[63] L. Gao, S. Liu, and R.A. Dougal, "Dynamic Lithium-Ion Battery Model for System Simulation," *IEEE Transactions on Components and Packaging Technologies*, Vol. 25, No. 3, pp. 495-505, Sept. 2002.

[64] S. Piller, M. Perrin, and A. Jossen, "Methods for state-of-charge determination and their applications," *Journal of Power Sources*, Vol. 96, Issue 1, pp. 113-120, June 2001.

[65] M. Coleman, C.K. Lee, Z. Zhu, and W.G. Hurley, "State-of-Charge Determination from EMF Voltage Estimation: Using Impedance, Terminal Voltage and Current, for Lead-Acid and Lithium-Ion Batteries," *IEEE Transactions on Industrial Electronics*, Vol. 54, No. 5, pp. 2550-2557, Oct. 2007.

[66] J. Chiasson and B. Vairamohan, "Estimating the State of Charge of a Battery," *IEEE Transactions on Control Systems Technology*, Vol. 13, No. 3, pp. 465-470, May 2005.

[67] B.S. Bhangu, P. Bentley, D.A. Stone, and C.M. Bingham, "Nonlinear observers for predicting state-of-charge and state-of-health of lead-acid batteries for hybrid electric vehicles," *IEEE Transactions on Vehicular Technology*, Vol. 54, No. 3, pp. 783-794, May 2005.

[68] M. Zi-Lin, M. Xao-jian, W. Jun-xi, Q. Jia-xi, and Z. Bin, "Research on SOC Estimated Strategy of Ni-MH Battery Used for Hybrid Electric Vehicle," *Proceedings of IEEE*

Vehicle Power and Production Conference (VPPC), pp. 1-4, Harbin, China, 3-5 Sept. 2008.

[69] Il-Song Kim, "Nonlinear state of charge estimator for hybrid electric vehicle battery," *IEEE Transactions on Power Electronics*, Vol. 23, No. 4, pp. 2027-2034, July 2008.

[70] F. Zhang, G. Liu, L. Fang, and H. Wang, "Estimation of Battery State of Charge with H_∞ Observer: Applied to a Robot for Inspecting Power Transmission Lines," *IEEE Transactions on Industrial Electronics*, Vol. 59, No. 2, pp. 1086-1095, Feb. 2012.

[71] Sang H. Kim, W. Choi, Kyo B. Lee, and S. Choi, "Advanced dynamic simulation of super-capacitors considering parameter variation and self-discharge," *IEEE Transactions on Power Electronics*, Vol. 26, No. 11, pp. 3377-3385, Nov. 2011.

[72] O. Bohlen, J. Kowal, and D.U. Sauer, "Aging behaviour of electrochemical double layer capacitors Part II. Life time simulation model for dynamic applications," *Journal of Power Sources*, Vol. 173, Issue 1, pp. 626-632, Nov. 2007.

[73] S. Buller, M. Thele, R.W.A.A. DE Doncker, and E. Karden, "Impedance Based Simulation Models of Supercapacitors and Li-Ion Batteries for Power Electronic Applications," *IEEE Transactions on Industry Applications*, Vol. 41, No. 3, pp. 742-747, May/June 2005.

[74] L. Zubieta and R. Bonert, "Characterization of double layer capacitors for power electronic applications," *IEEE Transactions on Industry Applications*, Vol. 36, Issue 1, pp. 199-205, Jan./Feb. 2000.

[75] R. Faranda, M. Gallina, and D.T. Son, "A new simplified model of Double-Layer Capacitors," *Proceedings of International Conference on Clean Electrical Power (ICCEP)*, pp. 706-710, Capri, Italy, 21-23 May 2007.

[76] L. Shi and M.L. Crow, "Comparison of Ultra-capacitor Electric Circuit Models," *Proceedings of IEEE Power and Energy Society General Meeting*, pp. 1-6, Pittsburgh, PA, USA, 20-24 July 2008.

[77] R.W. Erickson and D. Maksimovic (2001), *Fundamentals of power electronics*, 2nd Ed., New York: Springer.

[78] IGBT Power Losses Calculation Using the Data-Sheet Parameters, *https://www.btipnow.com*

[79] IGBT/MOSFET Gate Drive Optocoupler, WISHAY Semiconductors, *https://www.btipnow.com*

[80] K. Koga, R. Ueda, and T. Sonoda, "Constitution of V/f Control for Reducing the Steady-State Speed Error to Zero in Induction Motor Drive System," *IEEE Transactions on Industry Applications*, Vol. 28, No. 2, pp. 463-471, Mar.-Apr. 1992.

[81] X. Nian, F. Peng, and H. Jang, "Regenerative Braking System of Electric Vehicle Driven by Brushless DC Motor," *IEEE Transactions on Industrial Electronics*, Vol. 56, No. 4, pp. 1561-1572, July 2007,.

[82] J. Nocedal and S.J. Wright (1999), *Numerical Optimization*, Second Edition, USA: Springer.

[83] X.S. Yang (2010), *Nature-Inspired Metaheuristic Algorithms*, 2nd Edition, University of Cambridge, United Kingdom: Luniver Press.

[84] E.G. Talbi (2009), *Metaheuristics: From Design to Implementation*, New Jersey, USA: Wiley.

[85] D. Bertsimas and J. Tsitsiklis, "Simulated Anealing," *Statistical Science*, Vol. 8, No. 1, pp. 10-15, Feb. 1993.

[86] R.V. Rao, V.J. Savsani, and D.P. Vakharia, "Teaching-learning-based optimization: A novel method for constrained mechanical design optimization problems," *Computer Aided Design*, Vol. 43, No. 3, pp. 303-315, Mar. 2011.

[87] T. Niknam, F. Golestaneh, and M. Sha Sadeghi, "θ-Multiobjective Teaching-Learning-Based Optimization for Dynamic Economic Emission Dispatch," *IEEE Systems Journal*, Vol. 6, No. 2, pp. 341-352, June 2012.

[88] H.T. Jadhav, D. Chawla, and R. Roy, "Modified Teaching Learning Based Algorithm for Economic Load Dispatch Incorporating Wind Power," *Proceedings of 11th International Conference on Environment and Electrical Engineering (EEEIC)*, pp. 397-402, Venice, Italy, 18-25 May 2012.

[89] K. Deb, "An Efficient Constraint Handling Method for Genetic Algorithm, *Computer Methods in Applied Mechanics and Engineering*, Vol. 186, No. 2-4, pp. 311-338, June 2000.

[90] Orbtronic, *http://www.orbtronic.com/*

[91] M. Chen and G.A. Rincon-Mora, "Acurate Electrical Battery Model Capable of Predicting Runtime and I-V Performance," *IEEE Transactions on Energy Conversion*, Vol. 21, No. 2, pp. 504-511, Apr. 2008.

[92] Tecate Group, *http://www.tecategroup.com/*

[93] R. Faranda, M. Gallina, and D.T. Son, "A new simplified model of Double-Layer Capacitors," *Proceedings of International Conference on Clean Electrical Power (ICCEP)*, pp. 706-710, Capri, Italy, 21-23 May 2007.

[94] Tesla Motors Company, *http://www.teslamotors.com*

[95] United States Environmental Protection Agency, *http://www.epa.gov/*

[96] T. Hofman and C.H. Dai, "Energy efficiency analysis and comparison of transmission technologies for an electric vehicle," *Proceedings of IEEE Vehicle Power and Propulsion Conference (VPPC)*, pp. 1-6, Lille, France, 1-3 Sept. 2010.

[97] Impact of Vehicle Air-Conditioning on Fuel Economy, Tailpipe Emissions, and Electric Vehicle Range, National Renewable Energy Laboratory, *http://www.nrel.gov*

[98] Young-J. Lee, A. Khaligh, A. Chakraborty, and A. Emadi, "Digital Combination of Buck and Boost Converters to Control a Positive BuckBoost Converter and Improve the Output Transients," *IEEE Transactions on Power Electronics*, Vol. 24, No. 5, pp. 1267-1279, May 2009.

[99] S. Dusmez, A. Cook, and A. Khalig, "Comprehensive analysis of high quality power converters for level 3 off-board chargers," *Proceedings of IEEE Vehicle Power and Propulsion Conference (VPPC)*, pp. 1-10, Chicago, IL, USA, 6-9 Sept. 2011.

[100] P. Sinhuber, W. Rohlfs, and D. Uwe Sauer, "Conceptional considerations for electrification of public city buses," *Proceedings of Emobility - Electrical Power Train*, pp. 1-5, Leipzig, Germany, 8-9 Nov. 2010.